Development of the AC² Program ATHLET for Evolutionary Reactors and Research Reactors (Phase B)

Weiterentwicklung des AC²-Programms ATHLET für evolutionäre Reaktoren und Forschungsreaktoren (Projektphase B)

GRS - 864

Gesellschaft für Anlagen- und Reaktorsicherheit (GRS) gGmbH

Development of the AC² Program ATHLET for Evolutionary Reactors and Research Reactors (Phase B)

Weiterentwicklung des AC²-Programms ATHLET für evolutionäre Reaktoren und Forschungsreaktoren (Projektphase B)

Final Report

Philipp Schöffel
Vincenzo Anthony Di Nora
Norman Dünne
Volker Jacht
Markus Junk
Matthias Küntzel
Daniel von der Cron
Fabian Weyermann
Andreas Wielenberg

June 2026

Remark:

This report refers to the in-house research project UMRS1615 which has been funded by Federal Ministry for the Environment, Climate Action, Nature Conservation and Nuclear Safety (BMUKN).

The work was conducted by Gesellschaft für Anlagen- und Reaktorsicherheit (GRS) gGmbH.

The authors are responsible for the content of the report.

GRS - 864
ISBN 978-3-911727-57-0

Keywords

AC^2, CI, flow regime map, FONESYS, RBHT, software development, spacer grid, Thermal-hydraulic system code ATHLET

Abstract

The BMUKN-funded project UMRS1615 on the *Further Development of the AC² code ATHLET for Evolutionary Reactors and Research Reactors (Phase B)* aimed to develop and upgrade models and methods for the thermal-hydraulic system code ATHLET to support the numerous national and international code users with a powerful and reliable tool for performing safety analyses according to the current state of science and technology for existing reactors, advanced future reactor designs, research reactors, and SMR.

The extension of the central flow regime map module, that has been introduced in Phase A of the project, represents an important step in the ATHLET development towards a more mechanistically based thermal-hydraulic modelling. It allows for the consistent use of flow pattern information and associated closure equations through various models of wall and interfacial transfers. The central module was expanded by a dedicated flow regime map for post-CHF conditions and validated against RBHT and COSMOS experiments. This development also comprised the introduction of new flow patterns and transition criteria typical for film boiling conditions, including inverted annular and inverted slug flow regimes. For these flow regimes, specific closure relations were implemented to precisely consider the wall and interfacial friction. In addition, the distribution of the wall heat transfer to the fluid phases was revisited considering flow patterns with separated phases such as the annular or the stratified flow regime, which are of particular significance for the simulation of passive system heat exchangers.

Concerning the thermo-hydraulic modelling of the reactor core, a new model for spacer grids was implemented in ATHLET that considers turbulence-induced heat transfer enhancement and droplet breakup. The droplet breakup effect causes an increase in the interfacial area, which promotes steam condensation and cladding pre-cooling under reflood conditions. A successful validation was performed against tests from the RBHT facility. In addition, the thermo-mechanical modelling could be extended by introducing a dedicated approach with specific models for the simulation of horizontally oriented components such as the core bottom plate or the tie plate. Further code improvements are related to the calculation of critical discharge rates using the ATHLET's CDR1D model, and the treatment of frictional losses for system parts with uncomplete information. To a more realistic consideration of pressure losses for both the laminar-turbulent transition region as well as the helically coiled heat exchangers, developments originally launched by national partners at KIT and RUB were adopted and integrated in ATHLET to ensure their availability to all code users.

By participating in the OECD/NEA project RBHT-II, GRS gained access to new and detailed experimental data on bundle reflooding for code validation. Evaluation of open and blind calculations performed in the frame of the benchmark focused on parameters relevant to quench front model validation, such as cladding temperatures at different elevations, pressure drop along the test section, and quench front progression. Overall, the simulation results could satisfactorily reproduce the experimental trends. The predicted peak cladding temperatures agreed very well, while the times to reach the peak temperatures and to quench the bundle tended to be underestimated with ATHLET.

The collaboration within the international network FONESYS aimed at the evaluation of different system codes, the assessment of the suitability of implemented models, and the derivation of suggestions for improving the codes' capabilities for reactor safety analyses. Several joint benchmarks were implemented, which investigated cross flows, phase drift and interfacial friction in bundle geometries as well as two-phase pressure losses in specific components like orifice or contraction. Significant differences between the codes involved could be found with regard to heat transfer in dispersed flow film boiling regime and phase relative velocities under low pressure conditions, revealing potential for future developments to reduce existing modelling uncertainties.

The methods for quality assurance in program development were strengthened and adapted in alignment with current international standards. By introducing new and extended input data options, input data error checks, and output data, the user friendliness of ATHLET was substantially improved. An extended and quality-assured new code version, ATHLET 3.5, was released as part of the program package AC² 2025 and distributed to numerous code users through the continuously maintained AC² user area.

Kurzfassung

Das Rechenprogramm ATHLET (**A**nalyse der **T**hermo**H**ydraulik von **LE**cks und **T**ransienten) ist ein wesentlicher Bestandteil des Programmpakets AC² (**A**THLET, ATHLET-**C**D, **C**OCOSYS). AC^2 dient vorrangig der Simulation thermohydraulischer Prozesse in kerntechnischen Anlagen und wird von zahlreichen Organisationen im In- und Ausland als deterministisches Analysewerkzeug für Forschungsaktivitäten sowie gutachterliche Tätigkeiten zur Behördenunterstützung in kerntechnischen Genehmigungs- und Aufsichtsverfahren genutzt. Das Anwendungsspektrum von ATHLET umfasst Zustände des Normalbetriebs und des anormalen Betriebs, Störfälle wie auch Unfälle. ATHLET wird hauptsächlich von der GRS entwickelt und validiert. Unterstützung erfährt die GRS vor allem von nationalen Partnerorganisationen wie bspw. HZDR, HSZG, KIT, IKE, RUB, TUD und TUM.

Übergeordnetes Ziel des vorliegenden Projekts UMRS1615 war, den GRS-internen und externen Anwendern von ATHLET ein erweitertes, leistungsstarkes, zuverlässiges und anwenderfreundliches Werkzeug zur Verfügung zu stellen, das die Durchführung von Sicherheitsanalysen nach aktuellem Stand von Wissenschaft und Technik für bestehende Kernkraftwerke, für zukünftige, fortschrittliche Reaktoren der Generationen III und III+, für Forschungsreaktoren, sowie für SMR (Small Modular Reactors) erlaubt. Dies unterstützt die GRS bei ihren Aufgaben, als wichtiger Ansprechpartner zu Fragen der nuklearen Sicherheit aufzutreten und die Bundesregierung zu diesen Fragen auch zukünftig kompetent zu beraten. Die in diesem Vorhaben durchgeführten Programmentwicklungen tragen insbesondere dazu bei, eine realistischere Beschreibung von transienten, thermohydraulischen Vorgängen bei Auslegungsstörfällen und Unfällen zu erzielen und somit die Vorhersagegenauigkeit von ATHLET für wassermoderierte Reaktoren und evolutionäre Reaktorkonzepte im (nahen) Ausland sowie für SMR zu verbessern.

Einzelzielsetzungen

Das oben formulierte, übergeordnete Gesamtziel wurde in die folgenden fünf Einzelzielsetzungen untergliedert, die von den fünf wissenschaftlich-technischen Arbeitspaketen des Projekts aufgegriffen wurden. Die Einzelziele umfassten

- den Ausbau und die Ertüchtigung der ATHLET-Modelle zur detaillierten Simulation zweiphasiger Strömungsvorgänge im Kühlsystem nukleartechnischer Anlagen.

Wesentliche Aspekte betrafen die Konsolidierung und Erweiterung der programminternen Strömungsbildkarten mit zugehörigen strömungsbildspezifischen Schließungsgleichungen.

- die Verbesserung der thermomechanischen und thermohydraulischen Modellierung in ATHLET. Neben der Implementierung eines neuen Geometrietyps zur genaueren Abbildung horizontaler Strukturen und Einbauten wurde die Modellierung der Abstandshalter und deren Einfluss auf thermohydraulische Phänomene im Reaktorkern erweitert.
- die Zusammenarbeit in internationalen Arbeitsgruppen und Projekten, die Unterstützung der Programmanwender und GRS-externen Programmentwickler (insbesondere auf nationaler Ebene), sowie die Verbesserung der Programmhandhabung.
- die Qualitätssicherung der ATHLET-Programmentwicklung sowie die Freigabe und Verteilung aktualisierter und erweiterter ATHLET Programmversionen.

Die zu diesen Einzelzielsetzungen durchgeführten Arbeiten und erzielten Ergebnisse werden nachfolgend knapp zusammengefasst.

Strömungsbildkarten und Korrelationen für neue Strömungsbilder

Bereits in der Projektphase A zum vorliegenden Eigenforschungsvorhaben UMRS1615 war ein zentrales Strömungsbildkartenmodul in ATHLET implementiert worden. Die Implementierung ermöglicht flexibel die Hinzunahme weiterer Strömungsbildkarten und den stetigen Übergang zwischen neuen und bereits implementierten Karten. Diese Funktionalität nutzend wurde eine neue Strömungsbildkarte für Post-CHF-Zustände (gekennzeichnet durch Wandtemperaturen oberhalb der minimalen Filmsiedetemperatur) implementiert. Die Karte basiert auf etablierten Ansätzen aus der Literatur und berücksichtigt neben der Tropfenströmung auch die in ATHLET neuen Strömungsbilder der invertierten Schwallströmung und der invertierten Ringströmung. Für beide Strömungsbilder wurden neuen Schließungsgleichungen implementiert, um Zwischenphasenreibung und Wandreibung unter diesen Strömungsbedingungen realistischer zu erfassen.

Erste Validierungsrechnungen anhand von CHF- und Reflooding-Versuchen zeigen vielversprechende Ergebnisse, gleichwohl nicht für alle Rechnungen Verbesserungen erzielt werden konnten. Eine weitere Konsolidierung der Implementierung ist zukünftig beabsichtigt und könnte im Rahmen eines geplanten Nachfolgevorhabens erfolgen, in dem

die Strömungsbildkarten und die strömungsbildspezifischen Schließungsgleichungen weiter verbessert werden sollen. Mit der neuen Implementierung geht die Möglichkeit einher, Post-CHF-Zustände nun auch in ATHLET mechanistisch zu modellieren, was nach geeigneter Feinabstimmung und Validierung der beteiligten Modelle genauere Ergebnisse erwarten lässt und dem internationalen Stand der Technik für Systemcodes entspricht. Damit können zukünftig Unsicherheiten z.B. bezüglich der Phasenverteilung im Kern oder bezüglich der Hüllrohrtemperaturen reduziert werden.

Darüber hinaus bietet das zentrale Strömungsbildkartenmodul mit speziellen Karten für sowohl Pre-CHF- als auch Post-CHF-Zustände erhebliches Potential für zukünftige Programmverbesserungen, da hiermit detaillierte Strömungsbildkarten für alle Programmteile und Modelle verfügbar sind. So könnte z.B. das Bulk-Verdampfungsmodell, das bisher mit einer sehr vereinfachten Strömungsbildkarte arbeitet, die umfassende Information aus dem neuen Modul nutzen. Auch der Wärmeübergang zwischen Wand und Fluid kann unter Kenntnis des Strömungsbildes realistischer simuliert werden, indem bspw. der Wärmestrom bei Strömungsbildern mit klarer Phasenseparation derjenigen Phase zugeordnet wird, die sich im Kontakt mit der Wand befindet. Für die Strömungsbilder der Ringströmung und der stratifizierten Strömung wurde hierzu ein Modellierungsansatz entwickelt, der die Verteilung der Wärmeströme mechanistisch betrachtet und damit geringere Unsicherheiten bei der Berechnung der Phasentemperaturen bietet.

Verbesserung der thermomechanischen und thermohydraulischen Modellierung

Basierend auf Beobachtungen, dass ATHLET während des Refloodings oberhalb des Gemischspiegels teilweise zu hohe Hüllrohrtemperaturen berechnet, wurde das Abstandshaltermodell in ATHLET erweitert. Abstandshalter haben einen erheblichen Einfluss auf die Thermohydraulik im Reaktorkern. Aufgrund ihrer turbulenzerzeugenden Wirkung wird der konvektive Wärmeübergang stromabwärts eines Abstandshalters zunächst deutlich erhöht, bevor er mit größer werdendem Abstand exponentiell auf das Ausgangsniveau abfällt. Zusätzlich werden für disperse Strömungen unter Filmsiedebedingungen die mitgerissenen Tropfen beim Aufprall auf die Abstandshalter in zahlreiche kleinere Tropfen aufgespalten. Dies hat eine deutlich vergrößerte Zwischenphasenfläche zufolge, was aufgrund höherer Tropfenverdampfung und einhergehender Dampfkühlung und -beschleunigung eine stärkere Hüllrohrkühlung bewirkt.

Die präzise Nachbildung all dieser thermohydraulischen Effekte ist von besonderem Interesse, da die maximale Hüllrohrtemperatur während des Refloodings bei

Filmsiedebedingungen im oberen Kernbereich zu erwarten ist. Daher wurden neue Modelle in ATHLET implementiert, die die genannten Effekte berücksichtigen. Anhand der RBHT-Versuche, die detaillierte Messungen der Zustände stromauf- und stromabwärts der Abstandshalter enthalten, wurde das neue Abstandshaltermodell validiert. Insbesondere hinsichtlich der Zustände unmittelbar stromabwärts der Abstandshalter konnten mit der neuen Modellierung deutlich verbesserte Ergebnisse erzielt werden. Einerseits folgen die berechneten Hüllrohrtemperaturen qualitativ wie auch quantitativ genauer den experimentellen Werten. Andererseits wird auch die Dampftemperatur realistischer simuliert, was hauptsächlich eine Folge der nachgebildeten Tropfenaufspaltung und deren Einfluss auf den Zwischenphasenübergang ist. Ein weiterer Ausbau des Abstandshaltermodells von ATHLET ist im Nachfolgevorhaben geplant, um auch hier z.B. den Einfluss des Strömungsbildes genauer zu berücksichtigen.

Zur Simulation spezieller, horizontaler Strukturgeometrien wie Einbauten in Behältern oder Boden-/Deckenplatten von Pools wurde das Wärmeleitmodul von ATHLET um den neuen Strukturtyp „Horizontale Platte“ ergänzt. Dies ermöglicht dem Anwender, entsprechende Geometrien in ATHLET realistischer abzubilden und den Wärmeübergang zum umgebenden Fluid genauer zu berechnen. Für letzteres wurden spezielle Wärmeübergangskorrelationen für kühlende oder heizende Bedingungen sowohl an der Unterseite wie auch an der Oberseite der horizontalen Struktur implementiert. Damit wird es bspw. möglich, den Wärmeübergang über die untere Kernplatte hinweg zwischen Kernbereich und unterem Plenum während eines schweren Störfalls nachzubilden.

Des Weiteren wurde die Berechnung der kritischen Ausströmung für Lecks verbessert und ein Modell zur Berücksichtigung des Phasenschlupfs verfügbar gemacht. Insbesondere für Bedingungen nahe der Sättigung, für die es im Ausströmgebiet zu erheblicher Verdampfung und zweiphasiger Strömung kommt, zeigt diese Programmerweiterung eine Ergebnisverbesserung. Das Modell ist einstweilen optional im Datensatz zuschaltbar, bis umfangreichere Validierungsergebnisse vorliegen und eine abschließende Bewertung ermöglichen.

Für die Simulation des Strömungsdruckverlusts bei querangeströmten Rohrbündeln wurde eine dedizierte Korrelation in ATHLET eingebaut. Die Korrelation findet auch Anwendung auf der Außenseite von helikalen Wärmetauschern. Ebenfalls mit Blick auf helikale Wärmeübertrager wurden die Routinen zur automatischen Nodalisierung von Strukturobjekten verbessert, die eine Neigung zum umgebenden Fluidobjekt aufweisen (wie bspw. geneigte Rohrbündel in einem vertikalen Kanal). Die Programmverbesserung

erleichtert dem Anwender die Abbildung derartiger Geometrien im Eingabedatensatz. Weitere, vor allem auch numerische Verbesserungen, die in UMRS1615 umgesetzt werden konnten, betreffen die Simulation von Einspeisesystemen mit unterkühltem Medium sowie die Simulation nicht-kondensierbarer Gase.

Anwenderunterstützung, nationale und internationale Zusammenarbeit

Ein weiteres Arbeitspaket beschäftigte sich mit der Unterstützung der Programmanwender sowie Aspekten der nationalen und internationalen Zusammenarbeit. Ein kontinuierlicher Erfahrungsrückfluss aus der Programmanwendung wurde durch regelmäßige bilaterale Kontakte sowie durch ein weiteres, internationales AC²-Anwendertreffen im Jahr 2025 in den Räumlichkeiten der GRS Köln sichergestellt. Im Rahmen des Austauschs wurden die Programmanwender und externen Entwickler beraten sowie durch Bereitstellung verbesserter Modelle und Ad-hoc-Entwicklungen unterstützt. Z. B. wurde ein neuer Ansatz zur automatischen, initialen Druckverlustanpassung durch ATHLET für Systembereiche mit unvollständigem Kenntnisstand bereitgestellt. Auch die Schnittstellen zur Kopplung eigener CHF- und Wärmeübergangskorrelationen wurden erweitert, um aktuelle Forschungsarbeiten der Programmanwender bspw. für neue Anwendungssituationen bei sehr hohem Druck oder für innovative Reaktorkonzepte zu unterstützen. Ein weiterer Arbeitspunkt betraf die kontinuierliche Verbesserung der Programmhandhabung, hier insbesondere mit Blick auf die Erstellung der Eingabedaten und die Anwenderinformation vor, während und nach einer Simulation. Umfangreiche Prüfungen des Eingabedatensatzes und zusätzliche Programmausgaben mit Korrekturhinweisen wurden ergänzt. Beides wirkt Fehlern bei der Datensatzerstellung entgegen und vereinfacht diesbezüglich notwendige Anpassungen. Zusätzliche Ausgabegrößen zu integralen Massen- und Energiebilanzen unterstützen den Anwender zukünftig bei der Auswertung seiner Analysen.

Darüber hinaus wurden auch außerhalb der GRS erfolgte Programmentwicklungen mit dem Ziel begleitet, diese nach erfolgreichem Abschluss in den Hauptentwicklungszweig von ATHLET zu integrieren und damit allen Programmnutzern zugänglich zu machen. Im Rahmen dieser Arbeiten konnte z. B. ein genaueres Wandreibungsmodell für den laminar-turbulenten Übergangsbereich, das vom IKE entwickelt wurde, übernommen und nach verschiedenen Modellanpassungen in die übrige ATHLET-Programmstruktur integriert werden. Außerdem wurden Modellierungsansätze von RUB-PSS zur Simulation der Reibungsdruckverluste in helikaler Wärmeübertragern angepasst, final implementiert und für alle Anwender freigegeben. Helikale Wärmetauscher sind z. B. in

einigen aktuellen SMR-Konzepten vorgesehen, so dass diese Entwicklung die Aussagesicherheit von ATHLET für derartige Anwendungen stärkt.

Die mit ATHLET verteilten Werkzeuge zum Pre- und Postprocessing wurden ebenfalls kontinuierlich weiterentwickelt. Das Plotprogramm Batchplot wurde z.B. mit unterschiedlichen, neuen Optionen zur Erzeugung von Zeitverlaufsdiagrammen oder von ortsabhängigen (axial und radial) Profilplots ergänzt. Da Batchplot die HDF5-Ausgabedatei von ATHLET nutzt, wurde auch diese mit zusätzlichen Daten zur Geometrie des simulierten Systems und Einheiten der ausgegebenen Größen vervollständigt. Auch die beiden Tools AIG und GIG wurden mit neuen Funktionalitäten ausgestattet. So ist AIG nun auch für Linux-Betriebssysteme verfügbar.

Ein weiterer Aspekt betraf die Zusammenarbeit in internationalen Arbeitsgruppen. Neben der Kooperation innerhalb des FONESYS-Netzwerks, das den Austausch mit den Entwicklern verschiedener Systemcodes wie CATHARE, SPACE, APROS oder LOCUST fördert, hat sich die GRS am OECD/NEA Rod-Bundle Heat-Transfer-Projekt (RBHT-II) beteiligt. Die durchgeführten, offenen und blinden Nachrechnungen zu Versuchen aus der RBHT-Anlage der Penn State University dienten der Validierung insbesondere derjenigen Modelle, die für die Simulation des Wiederauffüllvorgangs eines Reaktorkerns nach einem Kühlmittelverlust wesentlich sind. Im Vordergrund von Phase II des Projekts standen niedrige Flutraten, die in Phase I des RBHT-Projekts für die eingesetzten Simulationsprogramme die größte Herausforderung darstellten. Insgesamt konnte ATHLET die maximalen Hüllrohrtemperaturen sehr gut reproduzieren. Allerdings wurde der Zeitpunkt der Wiederbenetzung häufig zu früh berechnet. Ursächlich scheinen die Wärmeübergangsberechnung im Filmsiedegebiet oberhalb der Quenchfront sowie das berechnete Voranschreiten der Quenchfront selbst zu sein.

Qualitätssicherung und Freigabe erweiterter ATHLET-Programmversionen

In einem weiteren Arbeitspaket standen unterschiedliche Aspekte der Qualitätssicherung der ATHLET-Programmentwicklung im Vordergrund. Hierzu wurde u.a. die bestehende CI-Infrastruktur unter GitLab funktional erweitert und die Testmatrix um weitere ATHLET-Datensätze und zugehörige Plotskripte ergänzt. Weitere qualitätssichernde Maßnahmen betrafen das Refactoring des Quellcodes, in dessen Zuge einzelne Programmteile überarbeitet wurden. Die Arbeiten dienen der Erhöhung der numerischen Performanz sowie der besseren Les- und Wartbarkeit des Programms und machen die ATHLET-Entwicklung mit Blick auf neue Anwendungen und damit einhergehende Quellcodeerweiterungen zukunftssicherer. Darüber hinaus wurden die Programmausgaben

ergänzt. So erleichtern zusätzliche Informationen zu im Datensatz definierten, aber nicht genutzten Parametern und zur Verwendung von Nicht-Default-Werten für einzelne Parameter den Programmanwendern die Pflege und Qualitätssicherung insbesondere von umfangreichen und langfristig entwickelten Anlagendatensätzen.

Die ATHLET-Programmdokumentation, die aus User's Manual, Models and Methods Manual, Validation Manual, Programmer's Manual, und Program Updates Manual besteht, wurde entsprechend des Entwicklungsfortschritts kontinuierlich fortgeschrieben und gemeinsam mit den neuen Programmversionen an die Nutzer verteilt. Teile der Dokumentation, die bisher unter der Software Microsoft® Word fortgeschrieben wurden, wurden nach Latex migriert, um Pflege und Versionierung langfristig zu erleichtern.

Innerhalb des Projektzeitraums wurde die aktuelle ATHLET-Programmversion, ATHLET 3.5.0, sowie ein Patch zur Vorgängerversion, ATHLET 3.4.3, fertiggestellt und freigegeben. Der Freigabe gingen jeweils umfangreiche qualitätssichernde Maßnahmen und Validierungsarbeiten voraus, um die Programmzuverlässigkeit und -leistungsfähigkeit sicherzustellen. Mit der neuen Codeversion wurden zahlreiche neue und verbesserte Modelle allen Anwendern zugänglich gemacht (für eine vollständige Übersicht siehe Kapitel 8.5.1). Als umfangreiche Weiterentwicklungen hervorzuheben sind

- das optional auswählbare Modul mit zentralisierten Strömungsbildkarten,
- das umfangreich erweiterte Modell für Abstandshalter mit Berücksichtigung ihres Einflusses auf den Wandwärmeübergang und die Tropfenaufspaltung,
- das erweiterte Heat-Pipe-Modell zur Simulation von horizontalen oder vertikalen Wärmerohren,
- ein neues Modell zur Simulation horizontaler Einbauten und Platten in Behältern wie dem RDB,
- die Simulation der 3D-Wärmeleitung in Strukturen unter Nutzung effizienter Lösungsverfahren, die über das Numerical Toolkit (NuT) verfügbar sind,
- die optionale Eingabe von 3D-Geometriedaten zur 3D-Visulaisuerung mittels ParaView, sowie
- die Integration von ursprünglich ATHLET-CD-eigenen Modellen zur Inventarberechnung, zum Spaltprodukttransport und zum thermomechanischen Brennstabverhalten in ATHLET.

Zur Verteilung von ATHLET und seinen Softwarewerkzeugen als Bestandteil von AC² wurde die User Area, die als Kommunikationsplattform mit den zahlreichen nationalen und internationalen Programmanwendern dient, kontinuierlich gepflegt und ergänzt.

Fazit und Ausblick

Die im Projekt UMRS1615 zur *Weiterentwicklung des AC²-Programms ATHLET für evolutionäre Reaktoren und Forschungsreaktoren – Phase B* vorgesehenen Themen und Arbeitsschwerpunkte konnten innerhalb der Projektlaufzeit von ca. drei Jahren erfolgreich bearbeitet werden. Gleichwohl sind nicht alle Entwicklungen abgeschlossen, so dass einige Arbeiten im Rahmen eines geplanten Nachfolgevorhabens bzw. innerhalb der kontinuierlich weitergeführten internationalen Zusammenarbeit fortgeführt werden sollen.

Im Rahmen des vorliegenden Projekts wurden mehrere thermohydraulische Neuentwicklungen abgeschlossen und Modellverbesserungen umgesetzt, die die Leistungsfähigkeit und die Zuverlässigkeit von ATHLET mit Blick auf ein ständig wachsendes Anwendungsspektrum gewährleisten. Die vorgesehenen Entwicklungen zur Simulation invertierter Strömungsbilder auf Basis dedizierter Strömungsbildkarten für Post-CHF-Zustände und Filmsiedebedingungen konnten erfolgreich durchgeführt werden. Die Arbeiten zur Nutzung spezifischer Schließungsgleichungen für diese Strömungsbilder konnte ebenfalls realisiert werden. Weitere umfangreiche Neuentwicklungen, die in UMRS1615 durchgeführt werden konnten, betrafen das Abstandshaltermodell und das Modell für horizontale Geometrien. Diese Programmerweiterungen zielen insbesondere auf eine präzisere Simulation des Reaktorkerns unter Störfallbedingungen und ermöglichen bspw. eine präzisere Vorhersage von Hüllrohrtemperaturen. Das GRS-Engagement im Rahmen der zweiten Phase des OECD/NEA RBHT-Projekts wurde weitergeführt und neue Versuche durch offene wie auch blinde Simulationen begleitet. Neben der erweiterten Validierung der Reflooding-Modelle von ATHLET ermöglichen die neuen Versuchsdaten zukünftige, auf diesen aufbauende Weiterentwicklungen, insbesondere hinsichtlich der Modellierung des Wärmeübergangs und der Quenchfrontdynamik, für die Verbesserungsbedarf identifiziert werden konnte.

Die intensive Zusammenarbeit und Unterstützung der Programmanwender wie auch die Kooperation in internationalen Arbeitsgruppen hat wichtige Impulse für die Weiterentwicklung von ATHLET gegeben, die im Projektverlauf aufgegriffen werden konnten und sich in zahlreichen Programmverbesserungen widerspiegeln, die mit der Freigabe der aktuellen Programmversion ATHLET 3.5 an die Nutzer verteilt wurden. Die Maßnahmen

zur Qualitätssicherung der Programmentwicklung wurden fortgeführt und ausgebaut. Die Nutzung von Issue Trackern, Merge-Requests, und der integrierten GitLab Continuous Integration mit erweiterter Testmatrix ermöglichen effiziente Arbeitsabläufe und fördern durch Vieraugenprinzip und automatisierte Programmverifikation die Qualität der Programmentwicklung.

Insgesamt tragen die im Rahmen des Projekts erzielten Programmverbesserungen wesentlich dazu bei, den zahlreichen im Umgang mit ATHLET geschulten Anwendern auch zukünftig ein leistungsstarkes, zuverlässiges und anwenderfreundliches Werkzeug zur Verfügung zu stellen, das die Durchführung von Sicherheitsanalysen nach dem neuesten Stand von Wissenschaft und Technik erlaubt. Sowohl mit Blick auf den verfügbaren Modellumfang als auch bezüglich der Programmimplementierung und Dokumentation hat ATHLET einen fortgeschrittenen, qualitätsgesicherten Entwicklungsstand erreicht, wodurch das Rechenprogramm für zukünftige Anwendungen und Weiterentwicklungen auf dem Gebiet der Reaktorsicherheitsforschung sehr gut aufgestellt ist.

Contents

1 Introduction 1

1.1 Objective 2

1.2 Particular Objectives 2

1.2.1 Detailed Simulation of Flow Regimes 2

1.2.2 Improved Modelling of Complex Two-Phase Phenomena 3

1.2.3 Improved Heat Transfer and Thermo-Mechanical Modelling 3

1.2.4 User Support and Co-Operation 4

1.2.5 Quality Assurance, Documentation and Release Management 4

2 Flow Regime Maps and Closure Laws for Post-CHF Conditions 5

2.1 Post-CHF Flow Regime Map 5

2.1.1 Transition between Pre- and Post-CHF Conditions 9

2.1.2 Closure Laws for Inverted Flow Regimes 11

2.1.3 Verification 13

2.2 Two-Phase Heat Transfer and Distribution of Heat Flow 26

2.2.1 Distribution of Heat Flows to Phases 26

2.2.2 Harmonization of Wall and Bulk Condensation Modelling 28

2.2.3 Verification against COSMEA 30

2.2.4 Conclusions 34

3 Improved Thermal-hydraulic Modelling 35

3.1 Cladding Pre-cooling and Droplet Breakup by Spacer Grids during Reflooding 35

3.1.1 Spacer Grid Droplet Breakup Modelling 36

3.1.2 Validation against RBHT 38

3.1.3 Summary 41

3.2 Simulation of Non-condensable Gases 42

3.3 Extended Critical Discharge Model 43

3.4 Thermal-hydraulic Simulation of ECC Injection Systems 44

4 Modelling of Structures and Internals 47

4.1 Horizontal Plate Model 47
4.2 Convective Heat Transfer Enhancement by Spacer Grids 49

5 Improved Program Handling and User Friendliness 53
5.1 New Options for Friction Loss Adaptation 53
5.2 Input Data Analysis and Extended Input Data Checks 53
5.3 New Input and Output Options 54
5.3.1 Input Data Extensions 54
5.3.2 HDF-5 Output Data Format 57
5.3.3 Output of GCSM signals units 58
5.4 Software Utilities 59
5.4.1 Batchplot Plotting Tool 59
5.4.2 3D Visualization with ParaView 65
5.4.3 AC²-GUI 66
5.4.4 ATHLET Input Graphics 66
5.4.5 GCSM Input Graphics 67
5.4.6 ATHLET Developer Tools 67

6 Program Improvements after User Feedback 69
6.1 Pressure Loss in Pipe Bundle Cross Flow 69
6.2 Automatic Nodalization of HCO 71
6.3 Laminar-turbulent Transition Friction Factor Calculation 73
6.4 Improved Condensation Model 74
6.5 Corrected Pressure Iteration 75
6.6 Extended Plugin Interfaces 76
6.7 Friction Loss Calculation for Helical Coil Heat Exchanger 76
6.8 Simulation of Reynolds Number-Dependent Form Losses 77
6.9 Solved Code Errors 78

7 International Cooperation 81
7.1 OECD/NEA RBHT-II Project 81
7.1.1 Test Parameters 81

7.1.2 Simulation Results 82
7.1.3 Summary 87
7.2 International AC² User Meeting 2025 88
7.3 Co-operation within the FONESYS Network 88
7.3.1 Core-3D Crossflow Benchmark 89
7.3.2 Bundle Interfacial Friction 98
7.3.3 Singular Pressure Loss Calculation 111

8 Quality assurance 117
8.1 Refactoring 117
8.2 Documentation 121
8.3 Continuous Integration 122
8.4 Quality Assurance and Build Tools 124
8.5 ATHLET Release Management 125
8.5.1 Code Version ATHLET 3.5.0 125
8.5.2 User Area and Code Transfer 131

9 Conclusion and Outlook 133

1 Introduction

For the safety analysis of transients, incidents and severe accidents in nuclear facilities, simulation codes are applied that provide realistic, so-called best-estimate, results in accordance with the current state of science and technology. The *Federal Ministry for the Environment, Climate Action, Nature Conservation and Nuclear Safety* (BMUKN) promotes the development and validation of such programs within the framework of reactor safety research. On this basis, GRS is developing the AC² program package, which includes the three system codes ATHLET, ATHLET-CD and COCOSYS, the 3D neutron kinetics code FENNECS, the interactive analysis simulator ATLAS and further tools /WEY 26/. The main purpose of the system code ATHLET (**A**nalysis of **TH**ermohydraulics of **LE**aks and **T**ransients) is the thermal-hydraulic simulation of the phenomena and processes in the coolant systems as well as heat removal systems of nuclear facilities. The ATHLET-CD (**C**ore **D**egradation) module provides models for fission product release and for damage and displacement of the reactor core. COCOSYS (**CO**ntainment **CO**de **SYS**tem) is used to analyse the thermal-hydraulics and the fission product behaviour in the containment.

AC² or individual programs of AC² are used as a deterministic analysis tool both in Germany and abroad by around 70 organizations for research activities and to support the regulatory authorities in nuclear licensing and supervisory procedures. The main objective of this project was the further development and improvement of the ATHLET thermal-hydraulic system code to keep pace with the evolving state of science and technology in nuclear safety. This allows to provide the numerous national and international code users with a powerful and reliable tool for carrying out safety analyses for a wide range of postulated incidents and types of nuclear facilities, including current and future (advanced) reactor designs, SMRs, and research reactors. In addition, the robustness of safety assessments made on the basis of simulation results achieved with ATHLET is reinforced.

The project *Further Development of the AC² code ATHLET for Evolutionary Reactors and Research Reactors* has been split into two project phases, where phase A was dealt with in RS1600 /SCH 24a/ and phase B in UMRS1615. The report at hand summarizes the results and findings achieved in project phase B.

1.1 Objective

ATHLET focuses on the thermal-hydraulic modelling of the cooling systems and heat removal systems of nuclear power plants and research reactors and additionally includes methods for the simulation of neutron kinetic power generation and reactor control systems. It is developed, validated, and applied for the analysis of conditions of normal operation, operational occurrences, design basis accidents and severe accidents in diverse nuclear facility designs. As component of the program package AC², ATHLET is distributed to and used by many organizations, TSOs, research centers and universities in Germany and abroad. As a deterministic analysis tool, the code is employed for research activities as well as for supporting nuclear licensing and supervisory procedures.

The overarching goal of this project was to provide the GRS and its national and international partner organizations a powerful, reliable, and user-friendly simulation tool that permits safety analyses according to the current state of science and technology for existing reactors and nuclear facilities, for advanced Gen III+ generation reactors, for SMR (Small Modular Reactors), and for research reactors. Associated with this, the further development of ATHLET enables the assessment and extension of international safety standards and contributes to the maintenance of competence in the field of nuclear safety in Germany.

1.2 Particular Objectives

The project's overarching goal was subdivided into five particular objectives, which were assigned to five scientific working packages. In the following, these particular objectives and the related subjects investigated in project phase B are briefly summarized.

1.2.1 Detailed Simulation of Flow Regimes

For the simulation of two-phase flow conditions in the reactor cooling circuit, it is of particular importance to determine the flow pattern for the flow channel correctly and to consistently apply appropriate constitutive equations for wall and interphase transfer. Therefore, the previously implemented model-specific flow regime maps of ATHLET and related closure laws should be centralized and expanded with regard to number of flow regimes distinguished. Furthermore, the heat transfer regime should also be considered when determining the flow regime and the according fluid dynamic closure laws. For heating surfaces and film boiling conditions, a dedicated flow map was to be

implemented in ATHLET, considering characteristics of inverted flow regimes that may significantly differ when compared to flows at adiabatic walls or pre-CHF conditions. The detailed determination of flow patterns and their transition criteria for film boiling conditions is of particular interest for the analysis of reactor core thermal-hydraulics and increases the predictive capability of ATHLET for the safety assessment of advanced light water-cooled reactors and SMRs.

Progress made towards this objective is outlined in chap. 2.

1.2.2 Improved Modelling of Complex Two-Phase Phenomena

The simulation of various complex two-phase phenomena in the cooling system of nuclear facilities required the elaboration of the code's modelling basis. Simulations of reflooding tests in bundle geometries had shown that ATHLET did not accurately describe the pre-cooling of the fuel rods in the region above the swell level, a finding that could be attributed to the lack of a suitable spacer grid model. The code's model basis should be extended accordingly. Additionally, in order to comply with existent user requirements, the modelling of injection systems as well as non-condensable gases should be revisited, mainly to improve the overall numerical performance of the code.

Progress made towards this objective is outlined in chap. 3.

1.2.3 Improved Heat Transfer and Thermo-Mechanical Modelling

Main aim is the more realistic simulation of structures connected to the core of a nuclear reactor to better predict their thermal-hydraulic impact on the course of an accident. On the one hand, the modelling of spacer grids should be extended so that their impact on the HTC downstream the spacer grid is captured. On the other hand, an approach should be developed to represent the lower and upper core support plates as horizontal structures, considering heat transfer processes between regions located below and above the plates, which is of particular interest for long-term severe accident applications.

Progress made towards this objective is outlined in chap. 4.

1.2.4 User Support and Co-Operation

In order to ensure the successful application of ATHLET, both ATHLET users as well as GRS-external code developers should be supported. This work comprises ad hoc developments, mainly to enable code application in new areas of interest or to fix program weaknesses, recommendations for input data preparation, and integration of external developments into the main ATHLET development line to provide them to all code users. A further aim of the code development is the continuous increase of the program's user-friendliness to prevent potential error sources and to simplify the preparation of valid input data sets. Share of experiences should be ensured by regular bilateral contacts and biennial international user meetings held in the premises of GRS. Finally, to further contribute to the international state of science and technology in the field of nuclear safety, GRS continued the cooperation within OECD/NEA benchmarks and international working groups like the FONESYS network.

Progress made towards this objective is outlined in chap. 5, 6 and 7.

1.2.5 Quality Assurance, Documentation and Release Management

The intended work aimed at the introduction of state-of-the-art methods and tools for the continuous quality assurance of the ATHLET code development, e.g., by implementing CMake for compilation, and employing code reviews through merge requests and issue trackers. The existing CI framework on GitLab should be further streamlined, extended by new functionalities and additional tests to ensure broader model coverage.

In accordance with the progress of development, the program documentation had to be continuously updated. New ATHLET (and AC²) program versions should be periodically released and distributed as installation files (for Windows and Linux OS) to all program users, so that their investigations take benefit from the latest developments and code improvements. Finally, the user area, mainly used for communication with the code users and for program distribution, should be maintained and continuously updated.

Progress made towards this objective is outlined in chap. 8.

2 Flow Regime Maps and Closure Laws for Post-CHF Conditions

2.1 Post-CHF Flow Regime Map

Literature research was carried out to find a map that is suitable to be adopted in ATHLET. Since post-CHF flow regime maps are typically utilized in thermal-hydraulic system codes, the research focused on model descriptions of the codes MARS, RELAP5-3D, RELAP7, SPACE, and TRACE. It was found that TRACE and RELAP7 make use of the same flow regime map (the one shown in Fig. 2.1), so do RELAP5-3D and MARS (the map is shown in Fig. 2.2). The map shown in Fig. 2.3 is implemented in TRACE and is qualitatively very similar to the RELAP5-3D and MARS map.

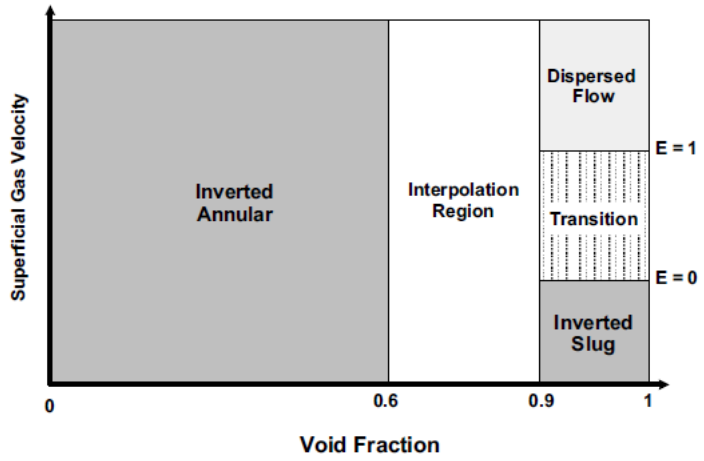

Fig. 2.1 Flow regime map for post-CHF conditions in vertical flow paths of TRACE /NRC 12/. $\mathbf{E}$ stands for the entrained droplet fraction.

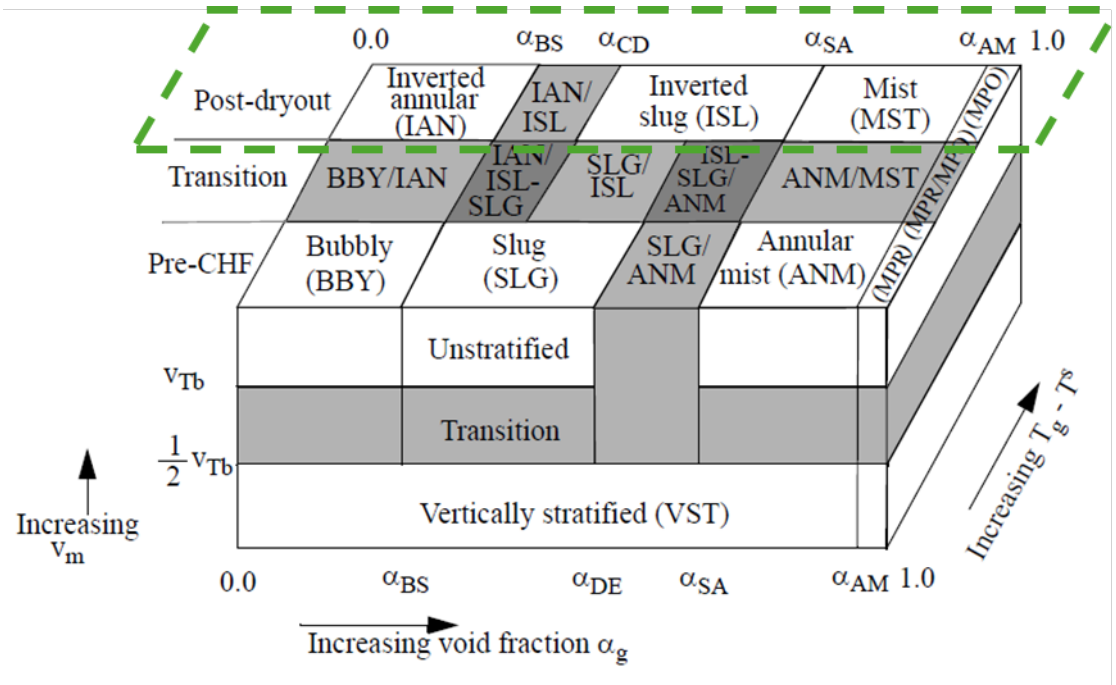

Fig. 2.2 Flow regime map for vertical flow paths of RELAP5-3D /INL 12/. The post-CHF flow regimes are within the area framed by the green dashed line.

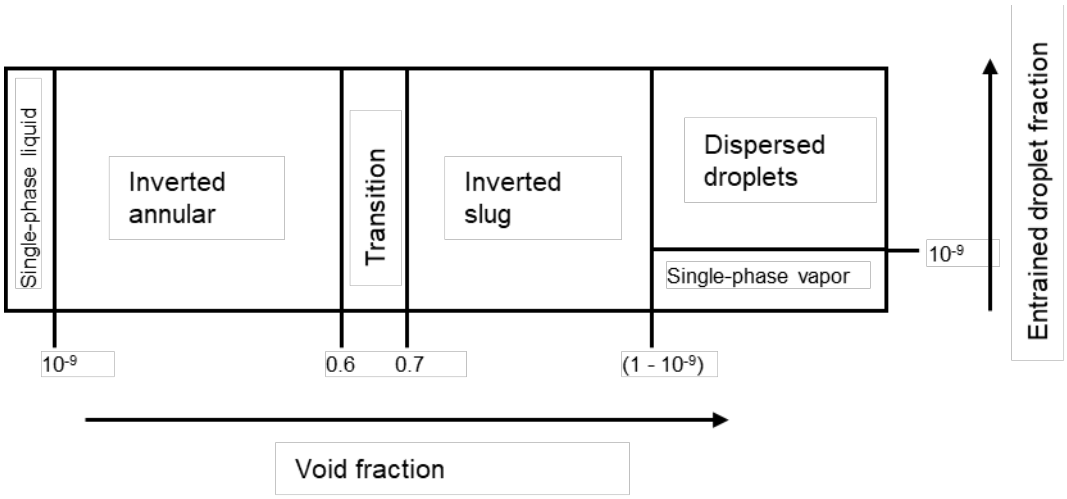

Fig. 2.3 Flow regime map for post-CHF conditions in vertical flow paths of SPACE (own work, based on /KIM 14/)

All these maps share some common features:

- Three flow regimes in the post-CHF region:
  - inverted slug flow
  - inverted annular flow

    - dispersed droplet flow (called “mist” in the RELAP5-3D and MARS maps)

- The interpolation bounds and transition criteria between the flow regimes depend on both the void fraction and the entrained liquid fraction. While the dependency on the entrained liquid fraction is obvious in Fig. 2.1 and Fig. 2.3, it is “hidden” in Fig. 2.2 within the criterion α_{SA}, which is – among other things – dependent on the critical velocity for the onset of entrainment.[1]

The only significant differences seem to lie in the actual numerical values of the transition boundaries and the question whether inverted annular flow and dispersed droplet flow are neighboring regimes or separated by inverse slug flow (compare Fig. 2.1 and Fig. 2.3). For the first implementation in ATHLET, it was decided to adopt the post-CHF flow regime map of TRACE and RELAP7 in ATHLET – mainly for two reasons:

- The map relies on fixed void fraction transition criteria which makes it easier to detect errors and track the effects of the flow regime prediction compared to “dynamic” transition criteria (as used in the RELAP5-3D and MARS map).

- The possibility of a direct transition from inverted annular flow to dispersed droplet flow looks reasonable and seems to be backed-up by experimental observations: “*Experimental data indicate that the inverted annular regime persists up to void fractions of 60-70% and that a smooth transition, in so far as the wall heat transfer is concerned, is made to the dispersed flow regime.*” /NRC 12/

Future ATHLET versions may be extended by further post-CHF flow regime maps, including the ones implemented in RELAP5-3D/MARS and SPACE.

In /SCH 24a/, the decision trees for creating the pre-CHF flow regime maps are shown. Analogously, the decision tree for the post-CHF map is shown in Fig. 2.4. Just as in the pre-CHF maps, the droplet flow regime precedes the others in importance: First, the entrained liquid rate is checked to decide whether the flow regime in a CV or junction can be (partially) characterized as droplet flow. The corresponding ratio is saved in $\mathrm{w}_{\mathrm{droplets}}$ which equals p_{droplets}. Then, the void fraction is checked to decide whether the remaining flow can be (partially) characterized as inverse annular and/or inverse slug

[1] Note in this context that the entrained liquid fraction is usually dependent the superficial vapor velocity and thus on the void fraction. This means that void fraction and entrained liquid fraction are no “orthogonal” concepts – though the flow regime maps in Fig. 2.1 and Fig. 2.2 might create this impression.

flow, with $p_{\text{inverse_annular}} = \left(1 - \text{w}_{\text{droplets}}\right) \cdot \text{w}_{\text{inverse_annular}}$ and $p_{\text{inverse_slug}} = \left(1 - \text{w}_{\text{droplets}}\right) \cdot \left(1 - \text{w}_{\text{inverse_annular}}\right)$.[2] For void fractions below $\alpha = 0.6$, entrainment is prohibited under CHF conditions. For void fractions between 0.6 and 0.9, an interpolation region is introduced. This finally results in the map shown in Fig. 2.5, which is similar to the TRACE map given in Fig. 2.1 (see also footnote 1 on the dependency of the entrained liquid fraction on the void fraction).

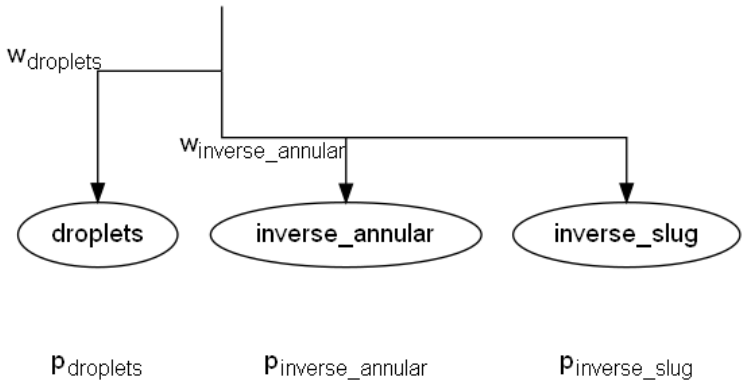

Fig. 2.4 Decision tree for the implemented post-CHF flow regime map for vertical channels

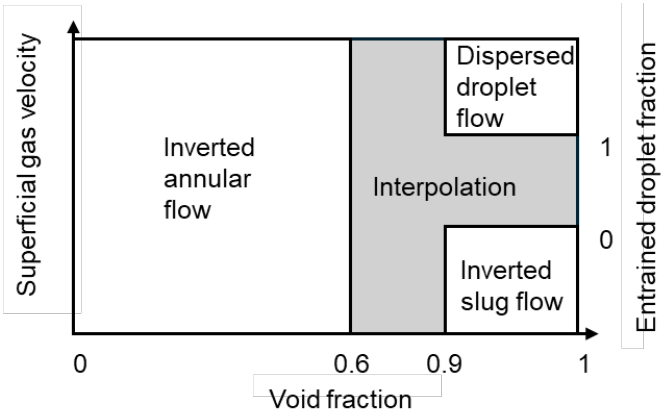

Fig. 2.5 Graphical representation of the post-CHF flow regime map for vertical channels as implemented in ATHLET

[2] More information on how the decision tree is walked through can be found in /SCH 24a/.

2.1.1 Transition between Pre- and Post-CHF Conditions

For the transition between pre- and post-CHF conditions, the general blending approach mentioned in /SCH 24a/, section "*Blending algorithm*", and described in detail in /CRO 23/, is applied. This means that a transition region between pre- and post-CHF conditions is defined by certain conditions. If the conditions in an ATHLET control volume (CV) are clearly pre-CHF conditions, a suitable pre-CHF flow regime map is applied. Conversely, if the conditions are clearly post-CHF conditions, the post-CHF flow regime map described above is applied. If the conditions in the CV are within the transition region, both the pre- and the post-CHF map are evaluated and their predicted flow regimes are blended.

To define the transition region between pre- and post-CHF conditions, a weighting factor $w_{CV} \in [0,1]$ has been introduced. $w_{CV} = 0$ means pre-CHF conditions, $w_{CV} = 1$ means post-CHF conditions, and $0 < w_{CV} < 1$ is the transition region where the predicted flow regimes of both maps are blended. The weighting factor is determined for a fluiddynamic CV. If a CV is in contact with more than one HCO – for example in a configuration as shown in Fig. 2.6, w_{CV} is the surface area-average of all w_H values with w_H being the weighting factor of a single HCO surface.

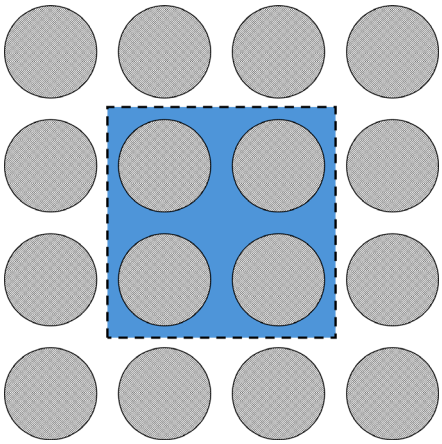

Fig. 2.6 A fluiddynamic CV (blue) which is in contact with four different HCOs

The weighting factor w_H of a surface is calculated by an evaluation of the heat transfer coefficients from the surface to the fluid:

$$w_H = \frac{htc_{NB} - htc_{tot}}{htc_{NB} - htc_{FB}} \tag{3.1}$$

with $\mathrm{htc}_{\mathrm{NB}}$ being the heat transfer coefficient for nucleate boiling, $\mathrm{htc}_{\mathrm{FB}}$ the heat transfer coefficient for film boiling, and $\mathrm{htc}_{\mathrm{tot}}$ an interpolated value between $\mathrm{htc}_{\mathrm{NB}}$ and $\mathrm{htc}_{\mathrm{FB}}$. Typically[3], $\mathrm{htc}_{\mathrm{NB}} > \mathrm{htc}_{\mathrm{tot}} > \mathrm{htc}_{\mathrm{FB}}$, which means:

- $w_{\mathrm{H}} = 0$ for pure nucleate boiling
- $w_{\mathrm{H}} = 1$ for pure film boiling
- $0 < w_{\mathrm{H}} < 1$ for transition boiling

The information about whether nucleate, film, or transition boiling is present as well as the various heat transfer coefficients are provided by the HECU module of ATHLET.

Note:
The procedure of averaging all w_{H} for determining whether pre- or post-CHF conditions are prevailing in a flow path follows a general approach pursued in ATHLET – for example, in order to decide whether a flow regime map for evaporation or for condensation /SCH 24a/ has to be applied, the surface temperatures of all HCOs adjacent to the considered flow path are averaged in a similar manner. This approach is in accordance with the lumped-parameter nature of the system code. Moreover, the flow regime maps found in literature are typically derived from experiments with pipes that have more or less uniform boundary conditions. However, one should be aware that situations in actual facilities could be more complex. For example, looking again at Fig. 2.6 – what would happen if the upper left HCO was a “hot rod”, i.e. the only one with post-CHF conditions while the other HCOs had pre-CHF conditions at their surfaces? ATHLET would at least recognize that it has to apply maps for both pre- and post-CHF conditions, and would predict flow regimes according to these maps, e.g. inverted annular flow for the post-CHF map and bubbly flow for the pre-CHF map. However, ATHLET would not assign the inverted annular flow regime specifically to the part of the flow channel which is in contact with the hot rod (and the bubbly flow to the rest). Instead, the predicted flow regimes – and thus all affected model predictions, such as the wall friction – would be “smeared” across the flow path. As said before, this is not a drawback specific to the CHF flow regime map, but generally rooted in the lumped-parameter approach of ATHLET. If the user wished to isolate the hot rod, he would have to refine the thermo-fluiddynamic grid.

[3] For explanatory purposes, only the typical case is described here. In the actual implementation, various cases are covered to ensure that w_{H} attains valid and reasonable numerical values.

2.1.2 Closure Laws for Inverted Flow Regimes

2.1.2.1 Interfacial Shear

The interfacial shear stress can be calculated from an interfacial friction factor f_i as:

$$\tau_i = \frac{\rho_g}{2} f_i {w_r}^2 \tag{3.2}$$

The ATHLET momentum equation considers the interfacial shear per unit volume, which is given by

$$\tau = \tau_i \frac{p_i}{A} = \frac{\rho_g}{2} \frac{p_i}{A} \cdot f_i \cdot {w_r}^2 = C_i \cdot {w_r}^2 \tag{3.3}$$

with $C_i = \frac{\rho_g}{2} \frac{p_i}{A} \cdot f_i$ the interfacial shear coefficient. In the inverted annular flow regime, smooth and wavy inverted annular films can be distinguished. The interfacial shear coefficient for the wavy film regime is calculated as follows /MOE 70/:

$$C_{i,\text{wavy}} = \frac{\rho_g}{2} \frac{p_i}{A} \cdot f_{i,\text{wavy}} = \frac{\rho_g}{2} \frac{p_i}{A} \cdot 0.05 \left(1 + 545 \left(\frac{\delta}{d_h}\right)^{1.42}\right) \tag{3.4}$$

with the relative vapor film thickness

$$\frac{\delta}{d_h} = \frac{1}{2}\left(1 - \sqrt{(1-\alpha)(1-e_d)}\right) \tag{3.5}$$

and e_d the entrainment fraction. For the inverted annular flow regime, it can be derived:

$$\frac{p_i}{A} = \frac{4}{d_h}\sqrt{(1-\alpha)(1-e_d)} \tag{3.6}$$

Alternatively to (3.4), the interfacial friction factor in wavy inverted annular flow can be calculated according to Wallis /WAL 70/:

$$f_{i,\text{wavy}} = 0.05\left(1 + 300\left(\frac{\delta}{d_h}\right)\right) \tag{3.7}$$

For a smooth inverted annular film flow, correlations for the interfacial friction factor are proposed on the basis of laminar vapor flow wall friction factor according to Hagen-Poiseuille. E.g., Cachard derived following expression /CAC 96/:

$$f_{i,\text{smooth}} = \lambda_{fv}\frac{24}{\text{Re}_v} \tag{3.8}$$

where λ_{fv} denotes an enhancement factor related to the momentum transfer from the vapor to the interface accounting for interfacial disturbances. However, since laminar vapor flow at low velocity can only be expected in a narrow region immediately downstream the quench front, and since the criterion for the transition from a smooth to a wavy inverted film flow is difficult to define /LIU 21/, only the interfacial friction for the wavy annular flow regime is considered in ATHLET. For the inverted slug flow regime, the same interfacial shear coefficient is used as for the wavy inverted annular flow regime.

2.1.2.2 Wall Friction

Wall friction in inverted annular flow is treated so that the friction assigned to the vapor phase is a function of the share of the inverted annular flow regime in the total flow. In case of a pure inverted annular flow, the wall friction is completely assigned to the vapor phase. To pursue a mechanistic approach, the wall friction pressure loss assigned to the vapor phase in inverted annular flow is calculated from the single-phase wall friction factor without enhancement by e.g. a two-phase multiplier. Additional friction losses due to the two-phase character of the flow are captured by the dedicated interfacial shear coefficient calculation described above. Using the Darcy-Weisbach friction factor for the vapor phase λ_v, the wall friction loss can be calculated as:

$$\zeta_{\text{wall}} = \lambda_v \frac{l}{d_h A^2}\frac{\rho_v}{2} \tag{3.9}$$

Details on how the Darcy-Weisbach friction factor is calculated in ATHLET can be found in chap. 6.3.

2.1.3 Verification

The extended FLRM module considering inverted flow regimes under post-CHF conditions has been verified against experiments from the COSMOS, RBHT and FLECHT facilities. In the following sections results for COSMOS (CHF tests) and RBHT (reflooding tests) are presented.

2.1.3.1 COSMOS

The test facility COSMOS (Critical-heat-flux On Smooth and MOdified Surfaces) was assembled at the Institute of Nuclear and Energy Technologies (IKET) of the Karlsruhe Institute of Technology (KIT). COSMOS is a water loop for thermo-hydraulic experiments of two-phase heat transfer and critical heat flux at low pressure. A detailed description of the facility and the conducted tests can be found in /HAA 12/. Already within research project RS1565, GRS performed ATHLET calculations of several COSMOS experiments; a description of these and of the used ATHLET data set can be found in the final project report /SCH 21/. For the simulations performed within UMRS1615 (the project described in the report at hand), the ATHLET data set created in RS1565 was taken as a basis. A subset of the experiments listed in /SCH 21/ was used for the test calculations. The simulations were performed both with activated and deactivated flow regime map module in order to investigate the effects of the new implementations. The following paragraphs summarize the major outcomes of the verification against COSMOS. Fig. 2.7 to Fig. 2.10 exemplarily show selected simulation results for COSMOS test LA-120-80-0250 (large annulus, 120 kPa outlet pressure, 80 °C inlet temperature, 250 kg/(m² s) mass flux).

To evaluate numerical stability and performance, the integration time step size, the CPU time, as well as the number of time steps and Jacobian matrix updates were compared. For the evaluated COSMOS experiments, both the simulations with activated and deactivated flow regime map module ran stably. However, the results comparison showed a clear tendency for a larger number of integration time steps and Jacobian matrix updates, both resulting in longer CPU times, when the flow regime map module was activated, see Fig. 2.7 and Fig. 2.8.

The residual mass error, too, showed a tendency for deterioration (i.e. its absolute value becoming larger) when the flow regime map module was activated. Fig. 2.9 shows the residual water mass in the simulated system (for comparison: the time-integrated mass flow rate through the system is at 69.5 kg at the end of the simulation at 1490 s, which means that the *relative* residual error is still quite small).

Regarding physical consistency, all simulations showed a generally reasonable behavior of the investigated physical parameters. An exception to this is the liquid inventory in the heated channel – in many simulations, a sudden increase in the liquid mass was observed, independently of the (de-)activation of the flow regime map module. An example of this behavior is given in Fig. 2.10 at time = 600 s. A first investigation found that at least one reason for this jump lies in a seeming contradiction between the fluiddynamic module (TFD) and the heat transfer module (HECU) of ATHLET: When the hot structure surface is rewetted, the heat transfer level does not drop back from post-CHF to pre-CHF conditions and ATHLET thus continues calculating very low film boiling heat transfer coefficients, even though the local void fraction in the TFD module is already calculated to be zero (meaning that there is no vapor film on the structure and therefore film boiling could not occur). Another possible cause for the liquid mass increase is suspected to be due to the bulk condensation model. Since the research objective of the COSMOS experiments was critical heat flux and the transition from nucleate boiling to film boiling, the focus of the ATHLET analyses was on these very processes and the rewetting phenomenon has not been further investigated. Nevertheless, the described issue needs to be addressed in a follow-up project.

Concerning the prediction of critical heat flux, the activation of the flow regime map module neither leads to a clear improvement nor to a clear degradation of the simulation results when compared to the simulations without flow regime map module. For one test case, the simulation result comes closer to the experimentally determined heat flux. On the other hand, for two test cases, the deviation from the measured values increases significantly. For the other cases, the calculated critical heat flux stays almost unchanged when the flow regime maps module is (de-)activated. Overall, ATHLET tends to underestimate the critical heat flux, i.e. film boiling is reached (too) early in the simulations. This means that the deviations from the experimental values are rather conservative (this holds true for simulations both with and without flow regime maps module). The calculated critical heat fluxes of the investigated test cases as well as their experimental counterparts are given in the table Tab. 2.1.

Tab. 2.1 Comparison of measured and calculated critical heat fluxes

Annulus size	Design exit pressure (kPa)	Design inlet temperature (°C)	Design mass flux (kg/m²/s)	Experi-ment	Simulation w/o FLRM		Simulation w/ FLRM	
				$\dot{q}_{CHF}$ (kW/m²)	$\dot{q}_{CHF}$ (kW/m²)	rel. error	$\dot{q}_{CHF}$ (kW/m²)	rel. error
small	115	45	250	660	569	-14%	529	-20%
small	115	65	250	840	559	-33%	558	-34%
small	115	80	250	670	563	-16%	563	-16%
large	120	45	250	1130	260	-77%	260	-77%
large	120	65	250	970	998	3%	801	-17%
large	120	80	250	820	556	-32%	583	-29%
large	120	80	400	1020	1022	0%	847	-17%
large	200	80	400	1190	1329	12%	1173	-1%

The data sets of the various COSMOS tests were added to the GRS GitLab server so that they can easily be included in regression testing pipelines in the future.

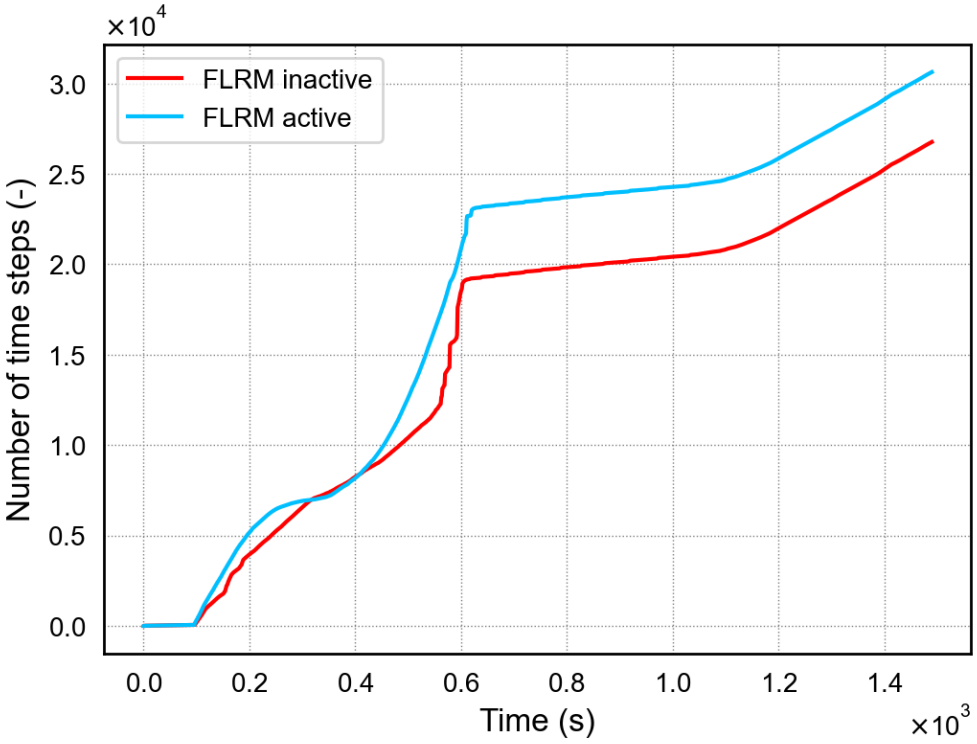

Fig. 2.7 COSMOS test LA-120-80-0250: Number of time steps needed with active and inactive flow regime map module

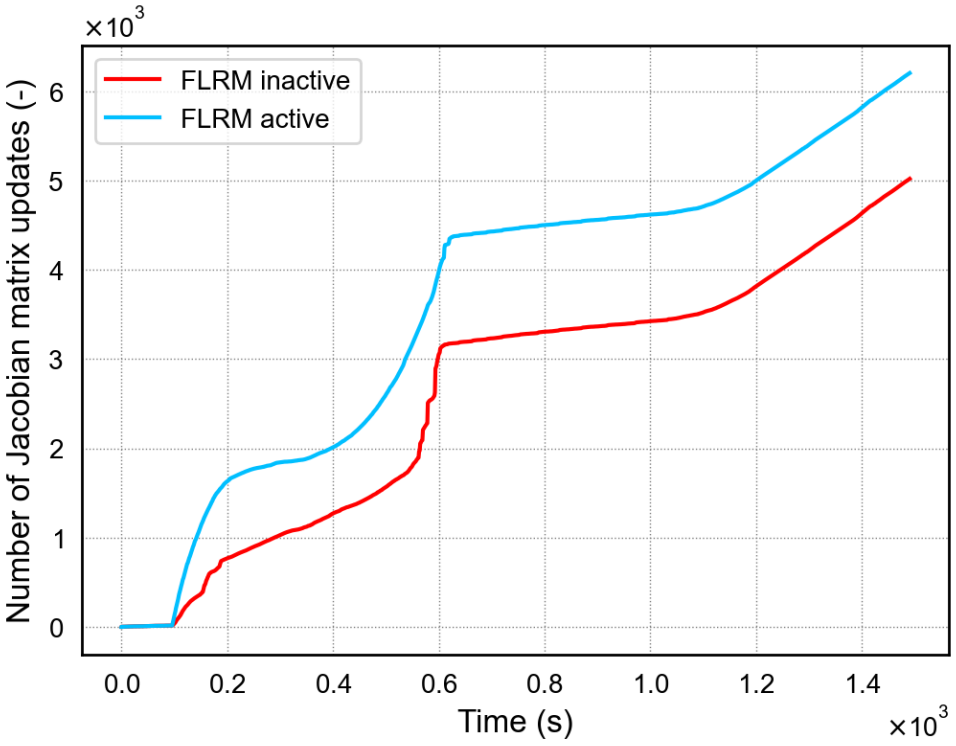

Fig. 2.8 COSMOS test LA-120-80-0250: Number of Jacobian matrix updates needed with active and inactive flow regime map module

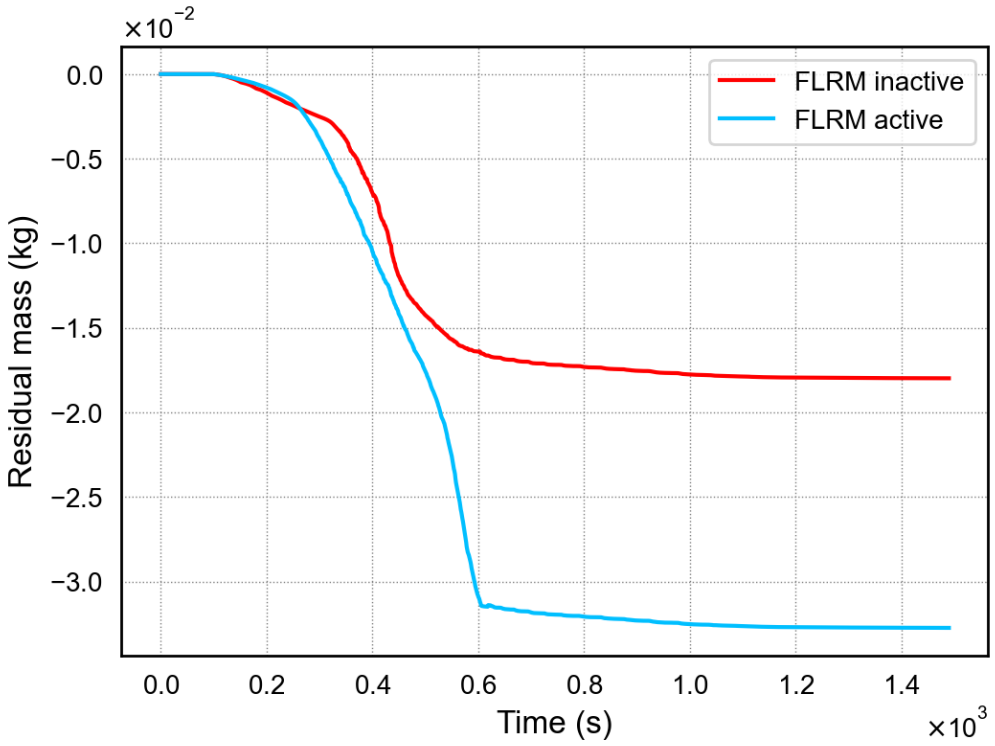

Fig. 2.9 COSMOS test LA-120-80-0250: Residual mass with active and inactive flow regime map module

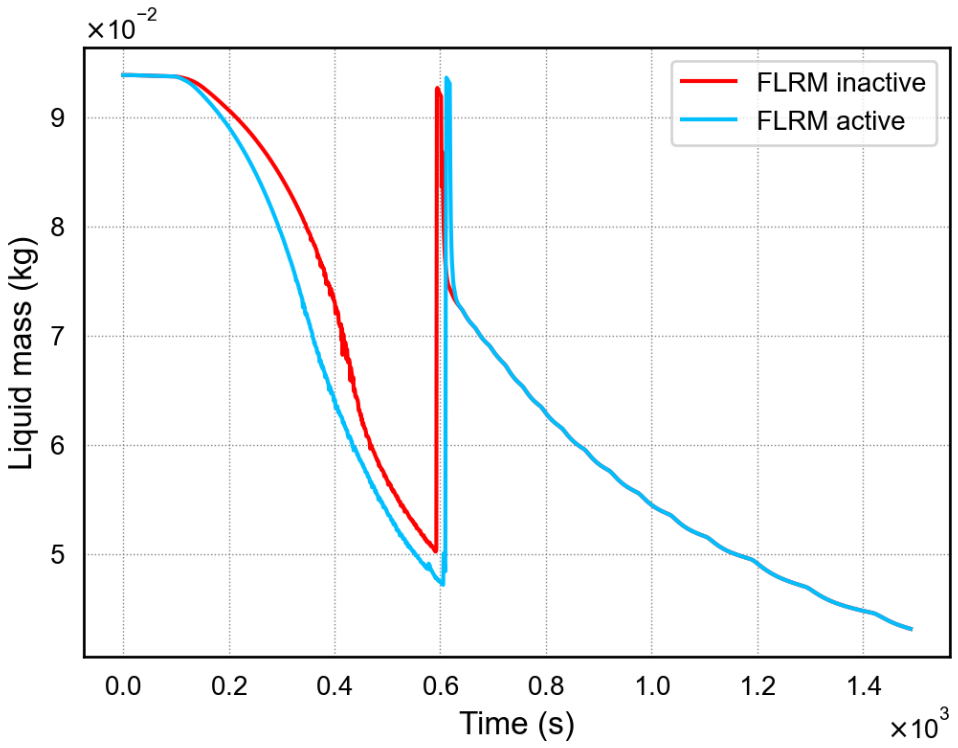

Fig. 2.10 COSMOS test LA-120-80-0250: Liquid mass inventory calculated with active and inactive flow regime map module

2.1.3.2 RBHT

The complete flow regime map module with extensions for post-CHF conditions and consideration of inverted flow regimes has been verified against RBHT project phase I open tests. Overall, eleven tests were performed in the frame of phase I /OEC 25/. The results obtained with the FLRM module are presented below, together with experimental values and code predictions achieved with the latest ATHLET release version 3.5 as reference.

Overall, eleven reflooding tests (O-1 to O-11) have been recalculated. The tests differed in inlet water subcooling (2.8 to 80 K), bundle power (35 to 252 kW) and reflood rate (0.5 to 15 cm/s). Generally, tests with high, medium or low reflood rate can be distinguished. Pressure was fixed at 2.8 bar. Details are presented in Tab. 2.2.

Tab. 2.2 Initial and boundary conditions of RBHT phase I open tests

Test #	Pressure [kPa]	Coolant Velocity [cm/s]	Bundle Power [kW]	Inlet Sub-cooling [K]	Init. Bundle Tempera-ture [K]
O-1	265	2.5	144	10	1000
O-2	266	2.5	144	78.9	1000
O-3	273	15	253	11.7	1144
O-4	276	15	253	80	1144
O-5	265	5	144	13.9	1000
O-6	268	2.5	144	31.7	1000
O-7	267	2.5, +3, -2, oscillating T=4s	144	9	1000
O-8	272	7.2 until 15s 5.1 until 30s 3.1 until 40s 1.4 until 1500s 1.1 from then on	144	26.1	1000
O-9	270	0.5	35	2.8	922
O-10	265	2.5	222, decay-ing	47.8	1000
O-11	273	5	144	11.1	1000

The used input data set is based on the work presented in /DÜN 22a/, /DÜN 22b/. Input data changes related to the simulation of spacer grids were introduced (for details see sections 3.1.1 and 4.2). Fig. 2.11 depicts the two-channel nodalization used to represent the RBHT facility.

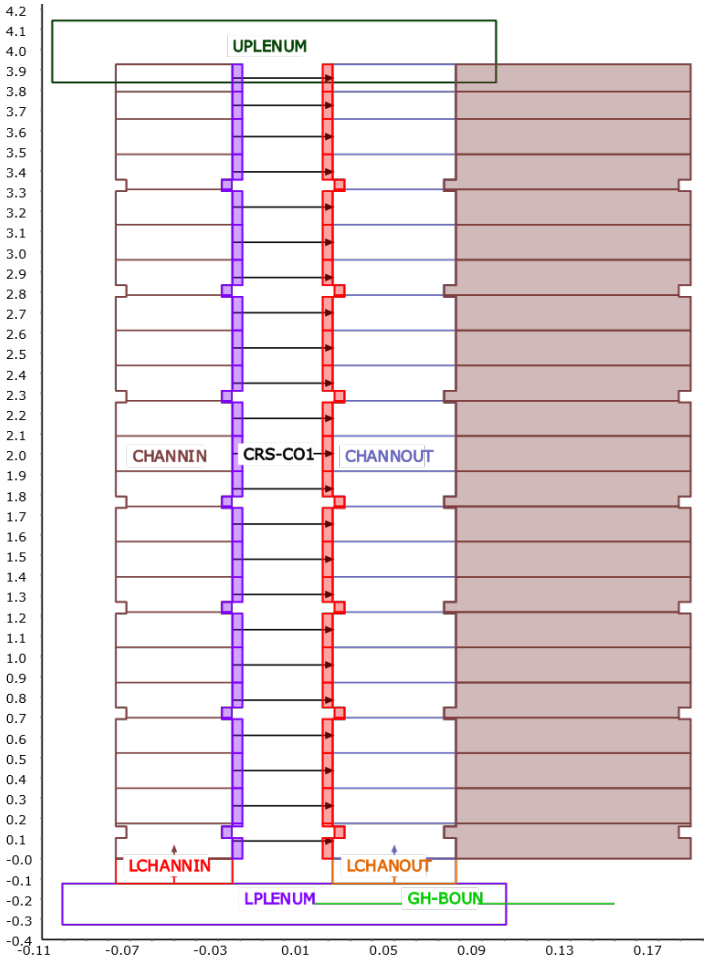

Fig. 2.11 RBHT facility nodalization

Considering the test cases with high flooding rates, a slightly increased quench front velocity was found leading to earlier rewetting and a better agreement between simulation and experiment. This can be seen from Fig. 2.12 to Fig. 2.15 for the tests O3 and O4.

For the medium and low flooding rate tests, an increased carryover mass flow was predicted by activating the extended FLRM models. This generally caused a slightly delayed quench front propagation, as can be seen from Fig. 2.16 to Fig. 2.18 for the medium mass flow rate tests O6 and O7. Similarly, for the tests with very low reflood mass flow rate, an increased carryover fraction accompanied by a later quench and increased cladding temperature was simulated, which generally improves the code predictions (Fig. 2.19 to Fig. 2.21).

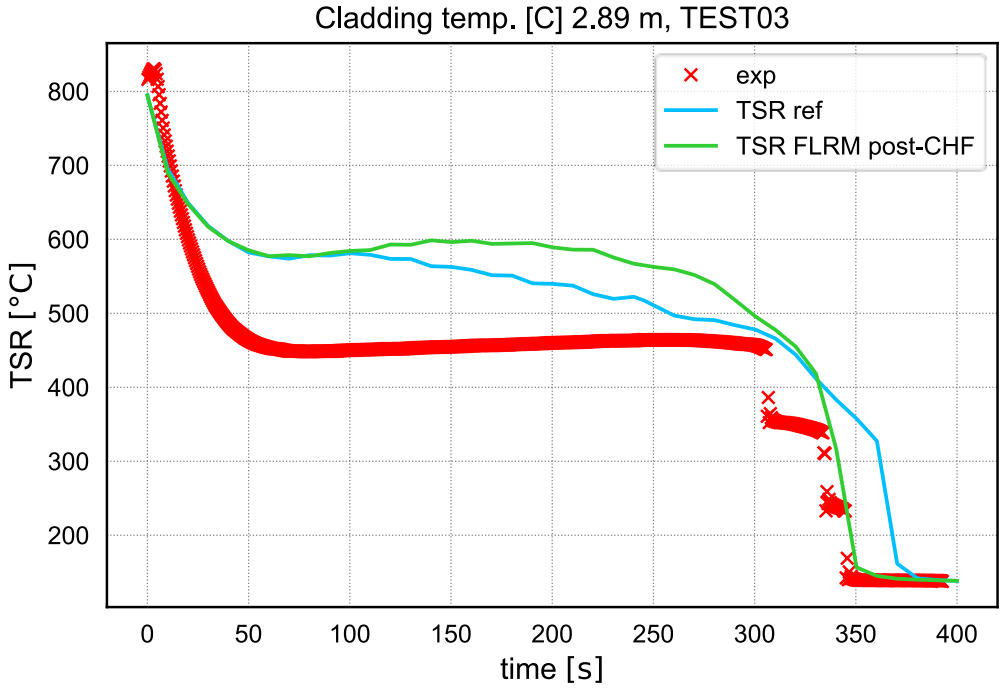

Fig. 2.12 Measured and simulated cladding temperature for test O3

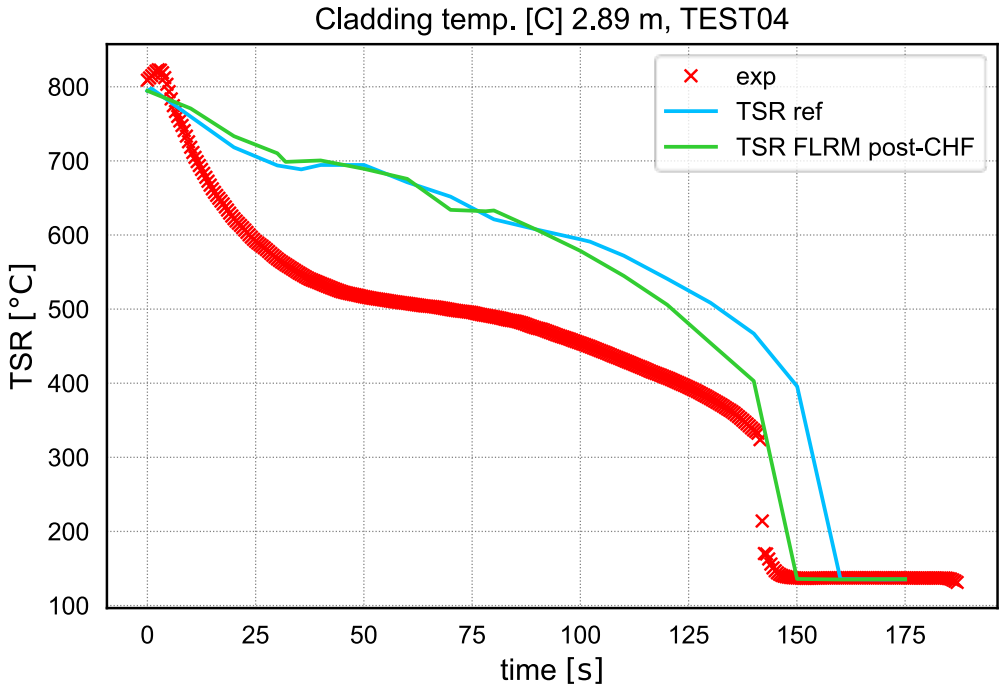

Fig. 2.13 Measured and simulated cladding temperature for test O4

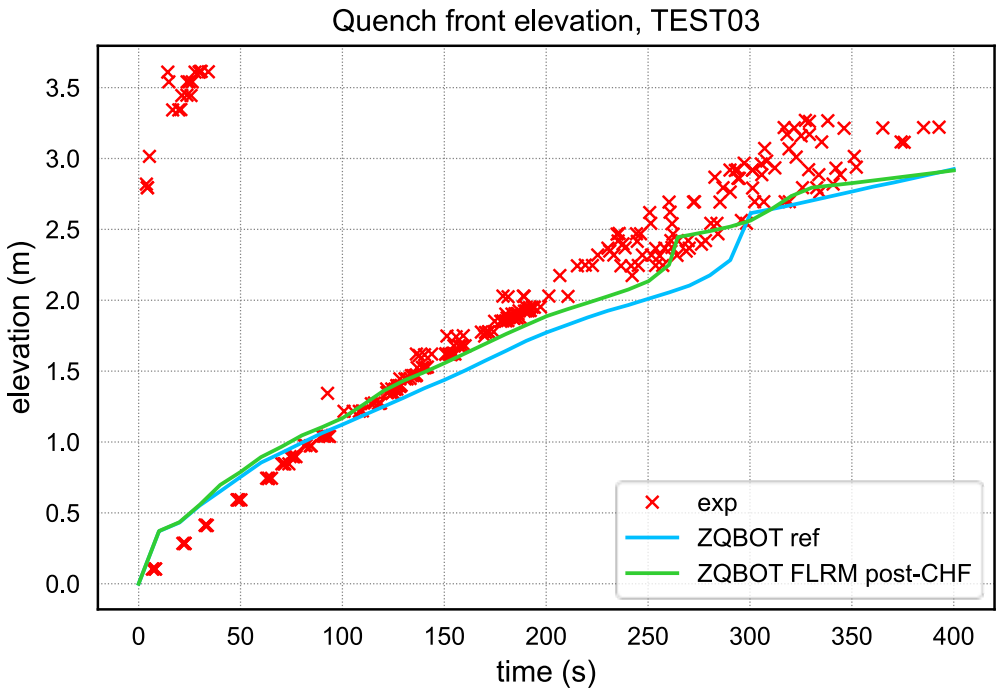

Fig. 2.14 Measured and simulated quench front progression for test O3

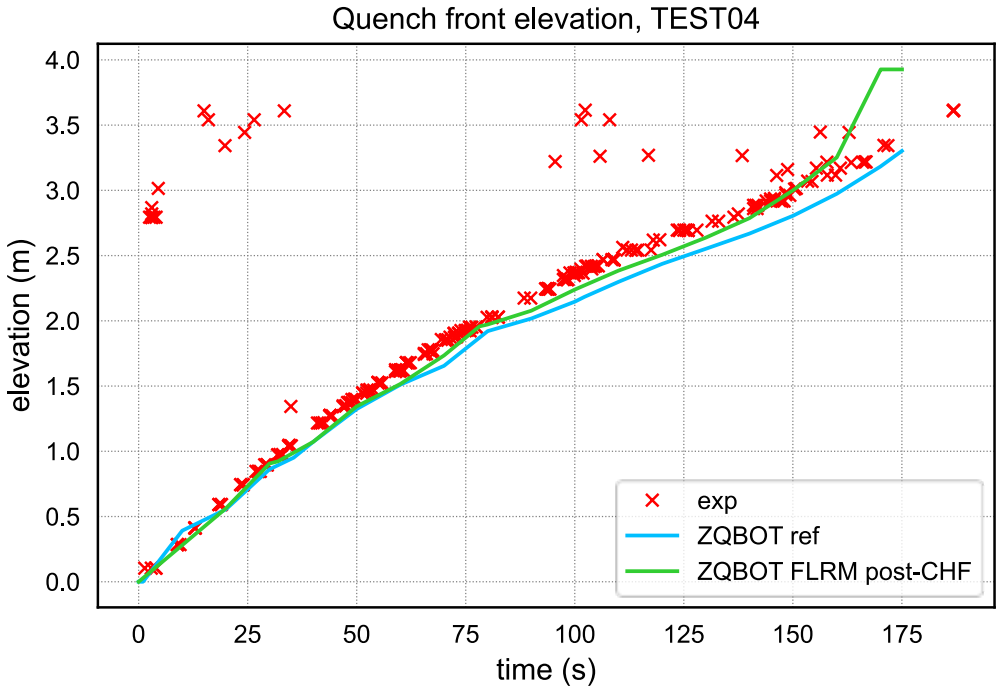

Fig. 2.15 Measured and simulated quench front progression for test O4

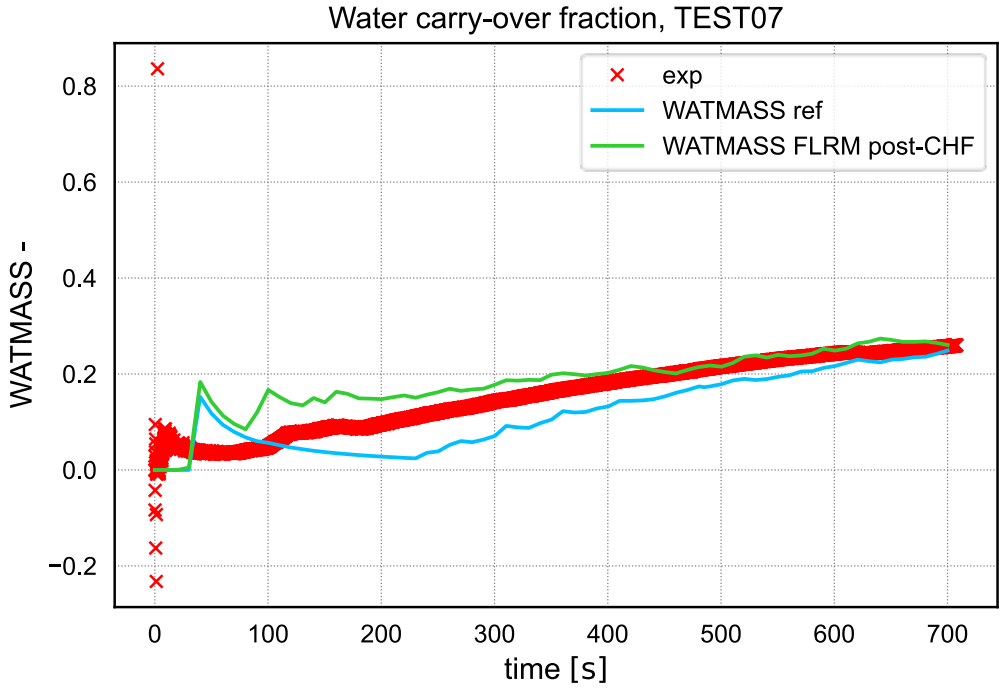

Fig. 2.16 Measured and simulated carry over fraction for test O7

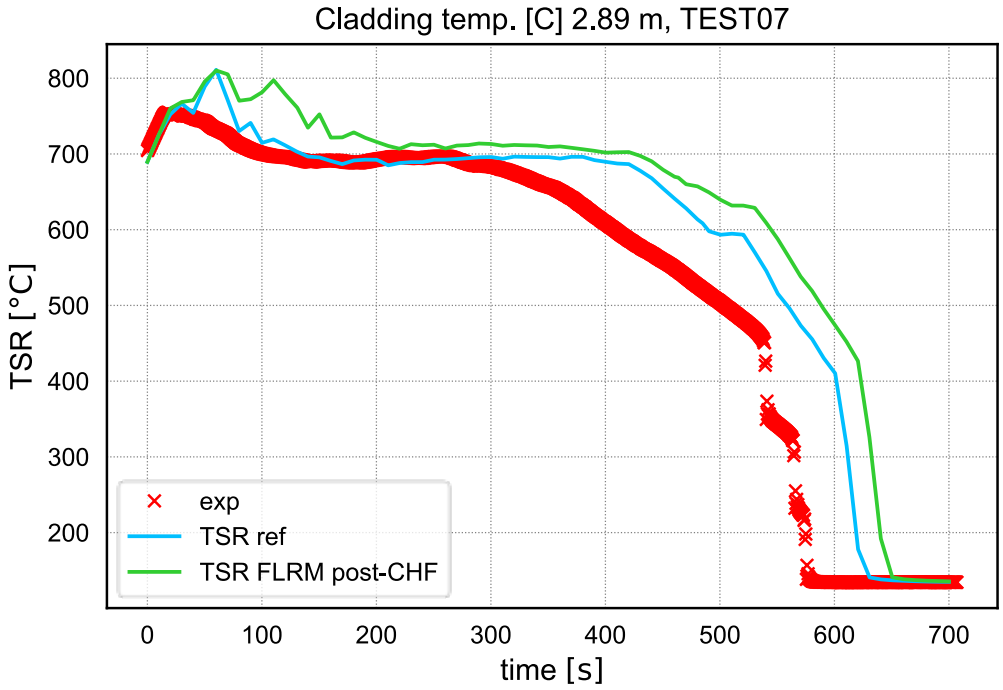

Fig. 2.17 Measured and simulated cladding temperature for test O7

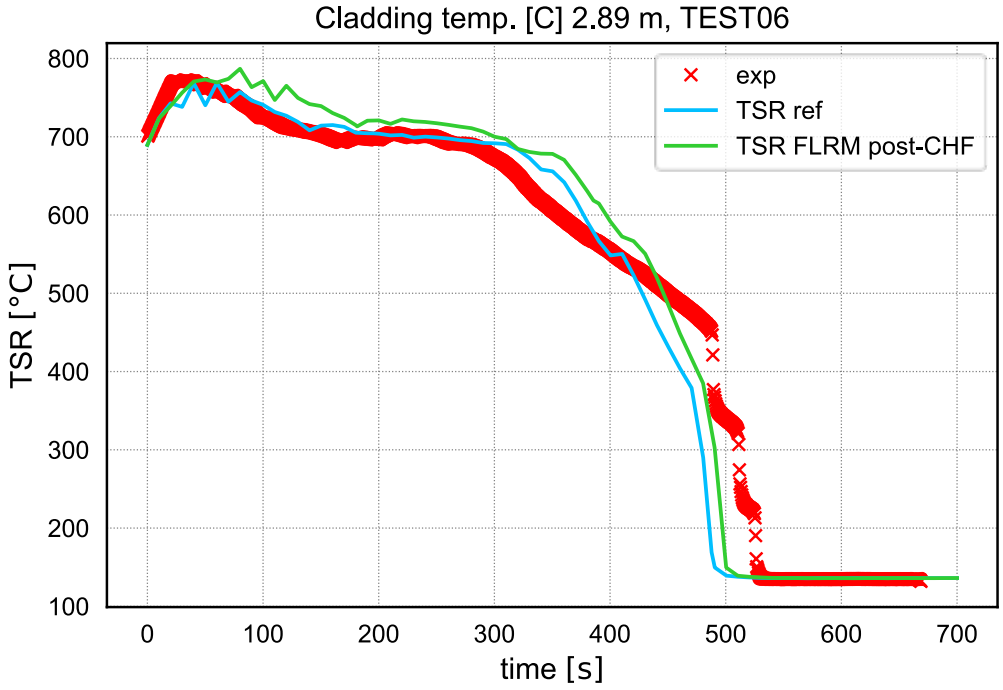

Fig. 2.18 Measured and simulated cladding temperature for test O6

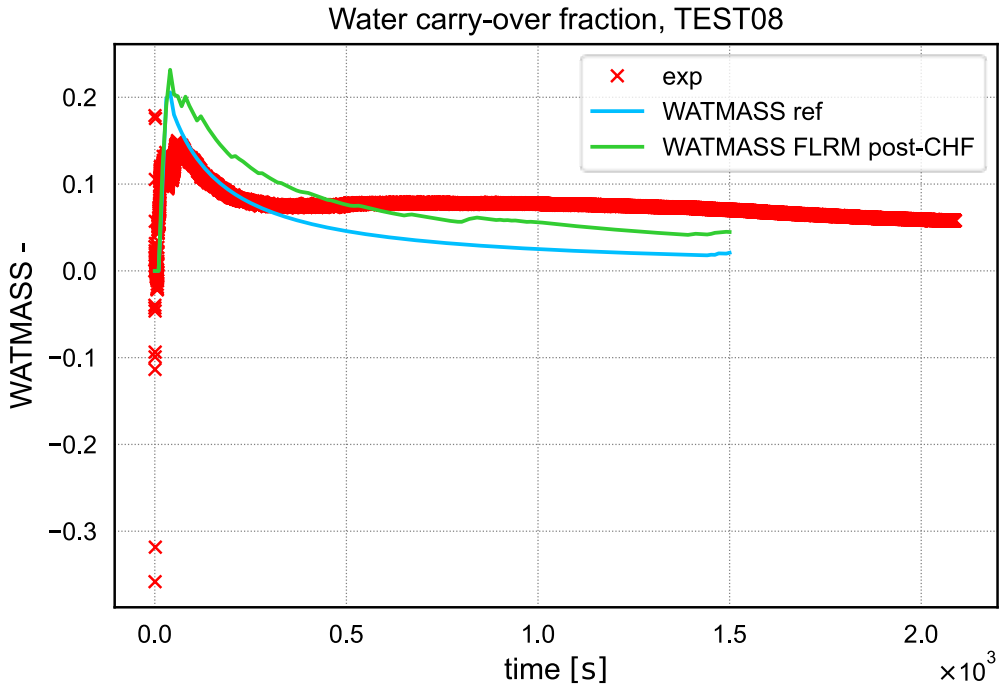

Fig. 2.19 Measured and simulated carry over fraction for test O8

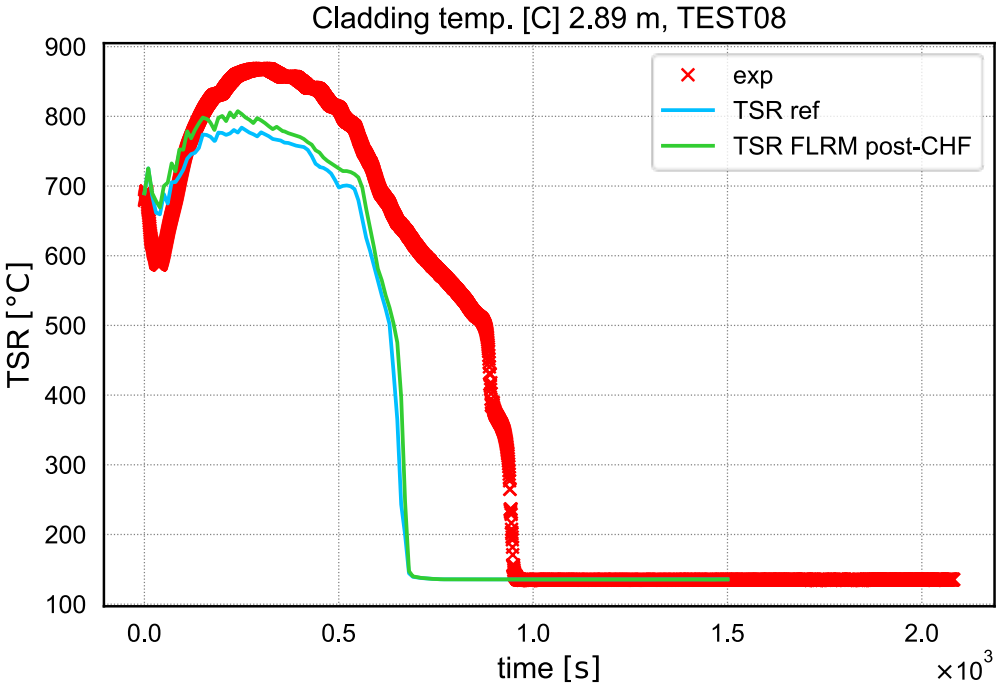

Fig. 2.20 Measured and simulated cladding temperature for test O8

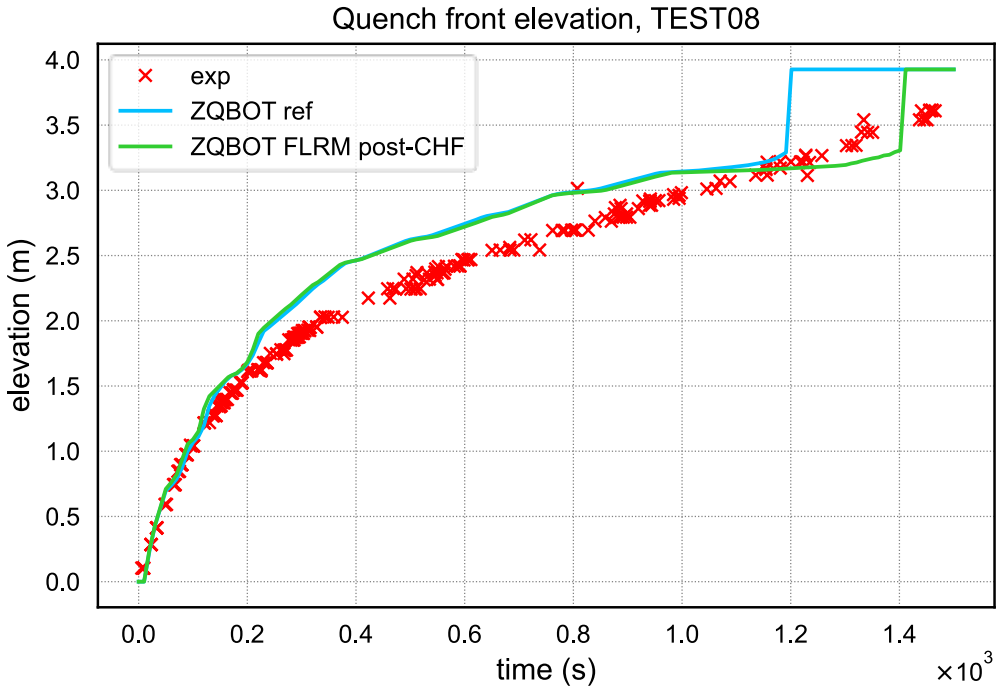

Fig. 2.21 Measured and simulated quench front elevation for test O8

2.1.3.3 Conclusions

While the extended FLRM modelling approach comprising post-CHF conditions yielded slightly improved simulation results for the RBHT simulations, its application impaired the numerical performance of the COSMOS calculations, without having a significant effect on the simulated physical behaviour. Therefore, further consolidation of the model is necessary. Model improvements that could be considered in the future include:

- Provide a more accurate and numerically stable simulation of interfacial friction in connection with the drift-flux model.
- Allow for a more detailed consideration of the derived flow pattern for HTC calculation in the post-CHF region.
- Perform a review of the quench front and the interfacial friction models, particularly with regard to experiments involving very low reflooding rates, for which ATHLET generally predicts quenching significantly too early.
- Provide additional post-CHF flow regime maps: So far, one post-CHF flow regime map, applicable for vertical flow paths, has been implemented. Additional post-CHF flow regime maps for vertical flow may be incorporated in ATHLET and tested for their suitability under various boundary conditions. Furthermore, post-CHF flow regime maps for horizontal flow paths may be implemented if needed.
- Enable the combined application of the FLRM and the mixture level model: So far, both models cannot work in combination. This limitation should be overcome in a future code version.
- Improve the numerical efficiency of the FLRM. For several test cases, ATHLET is slower and sometimes needs more time steps if the FLRM is active. This has already been an outcome of RS1600 and does not (only) depend on the FLRM implementation for post-CHF conditions. The weaker numerical performance needs to be addressed by further consolidating the existing implementation, better aligning the current modeling with regard to interfacial and wall transfers, improving numerics settings and identifying root causes for numerical problems.

Apart from the flow regime map module, the following general needs for further development of ATHLET have been identified within the frame of the verification calculations:

- Regarding the movement of the quench front, it can be observed that the calculated velocity of the quench front is too low when the position of maximum power (at about 2.5 m for RBHT tests) is passed. A thorough analysis of the quench model should be performed to investigate this behavior.
- The simulation of the COSMOS experiments revealed a seeming contradiction between the fluiddynamic module (TFD) and the heat transfer module (HECU) of ATHLET: When a hot surface is re-wetted, the heat transfer level does not drop back from post-CHF to pre-CHF conditions and ATHLET thus continues calculating very low film boiling heat transfer coefficients, even though the local void fraction in the TFD module is already calculated to be zero (meaning that there is no vapor film on the structure and therefore film boiling could not occur). This behavior seems unphysical and needs to be improved.

2.2 Two-Phase Heat Transfer and Distribution of Heat Flow

For the calculation of the heat flow between wall and fluid, ATHLET provides a comprehensive heat transfer package with numerous HTC correlations for single-phase and two-phase conditions. Three cases are distinguished for the HTC calculation: cooling walls, adiabatic/heating walls, and film-boiling conditions. By default, the total heat flow is distributed to the phases depending mainly on their phase fraction. This approach has been proven to be successful for well-mixed flow regimes like bubbly or annular flow. However, for flow regimes with clearly separated phases, a more mechanistic approach seems to be beneficial. Relevant flow regimes are the annular flow regime (vertical and horizontal) as well as the stratified/stratified-wavy flow regime (horizontal only). For these flow regimes, the wetted fraction of the wall can be determined (for stratified flow based on the void fraction) and an according approach for the calculation of the phase heat flows has been derived now.

2.2.1 Distribution of Heat Flows to Phases

In general, a total HTC and a HTC for the gas phase are calculated by the heat transfer package. From the total HTC, a total heat flow is derived:

$$Q_{\mathrm{tot}} = A_{\mathrm{HCV}} \cdot \mathrm{htc}_{tot} \cdot (T_w - T_v) \tag{2.10}$$

From the HTC for the gas phase, a fictitious heat flow to the vapor phase can be calculated:

$$Q_v = A_{\mathrm{HCV}} \cdot \alpha_v \cdot \mathrm{htc}_v \cdot (T_w - T_v) \tag{2.11}$$

Finally, Q_v is used to calculate the fraction of the total heat flow Q_{tot} that has to be provided to the vapor phase.

In general, htc_v is the convection to vapor HTC, e.g. calculated by Dittus-Boelter or Mc Eligot correlations. For cooling wall condition, condensation may also occur at the wall surface. In that case, htc_v is calculated from

$$\mathrm{htc}_v = \max(\mathrm{htc}_{\mathrm{convection}}, \mathrm{htc}_{\mathrm{cond}}) \tag{2.12}$$

where $\mathrm{htc}_{\mathrm{cond}}$ is the condensation HTC derived from specific correlations. Additionally, a condensation heat flow to be provided to the vapor phase can be derived:

$$Q_{\mathrm{cond}} = A_{\mathrm{film}} \cdot \alpha_v \cdot \mathrm{htc}_{\mathrm{cond}} \cdot \left(T_w - T_{v,\mathrm{sat}}\right) \tag{2.13}$$

It should be noted, that Q_{cond} for condensation differs from Q_v regarding the temperature difference to be used. The temperature difference applied for the condensation heat flow has been modified in the code. Now, $\left(T_w - T_{v,\mathrm{sat}}\right)$ is consistently used instead of $\left(T_w - \min\left(T_{\mathrm{fluid}}, T_{v,\mathrm{sat}}\right)\right)$. Considering the heat-of-evaporation at the prevailing conditions, a condensation mass transfer rate can be easily determined from Q_{cond}.

For annular flow, the water film is assumed to be at the wall surface, so that the heat transfer between wall and fluid should be completely directed towards the liquid phase. For stratified flow, the heat flow should be distributed in accordance with the wetted and try perimeter fractions. Adopting this approach under consideration of the shares the relevant flow regimes have in the overall flow field, finally yields the heat flow directed to the vapor phase as follows:

$$Q_v = A_{\mathrm{HCV}} \cdot \alpha_v \cdot \mathrm{htc}_v \cdot (T_w - T_v) \cdot \left(1 - \varepsilon_{\mathrm{ann}} - \varepsilon_{\mathrm{strat}} \frac{p_l}{\pi\, d_h}\right) \tag{2.14}$$

$$Q_{\mathrm{cond}} = A_{\mathrm{film}} \cdot \alpha_v \cdot \mathrm{htc}_{\mathrm{cond}} \cdot \left(T_w - T_{v,\mathrm{sat}}\right) \cdot \left(1 - \varepsilon_{\mathrm{ann}} - \varepsilon_{\mathrm{strat}} \frac{p_l}{\pi\, d_h}\right) \tag{2.15}$$

2.2.2 Harmonization of Wall and Bulk Condensation Modelling

In the case of heat transfer involving wall condensation – that is, when the wall temperature is below the saturation temperature of the vapor – a wall condensation rate G_{cond} is calculated. The wall condensation rate is derived from the condensation heat flow:

$$G_{\mathrm{cond}} = \frac{Q_{\mathrm{cond}}}{\Delta H_{\mathrm{evap}}} \tag{2.16}$$

Strictly speaking, G_{cond} is considered as condensation potential first. This condensation potential is subsequently taken into account when calculating the total condensation rate in a CV, which is determined by the bulk heat and mass transfer model, which G_{cond} contributes to.

The bulk heat and mass transfer model calculates the (final) evaporation or condensation rate in the fluid to determine the phase transition within the CV. This is derived from the sum of two components, which the liquid phase (subcooled or superheated) on the one hand, and the vapor phase (also subcooled or superheated) on the other contributes to. In addition, the wall condensation rate (or wall evaporation rate for nucleate boiling) is added. This approach is appropriate if the wall model and bulk model describe different phase transition phenomena (example: subcooled nucleate boiling at the wall and simultaneous condensation of the bubbles in the subcooled bulk liquid).

In the case of wall condensation, heat transfer correlations such as the Dobson-Chato correlation are used, which take into account the condensation of vapor at the saturated film surface of an annular flow or stratified flow. This therefore refers to a contribution to condensation not directly at the wall, but within the flow at the liquid surface. However, this condensation is also taken into account by the bulk model. In this case, simply adding the two is therefore incorrect and leads to overestimated condensation rates. The bulk model and the wall model had therefore to be better harmonized with each other. Basically, this could be achieved by using the higher of the two condensation rates.

In ATHLET, condensation rates have a negative sign and evaporation rates a positive. If G_{cond} is not zero, it is treated as a minimum condensation rate, which may be further increased by the bulk condensation model:

$$G_{\mathrm{cond,tot}} = \min(G_{\mathrm{bulk}}, G_{\mathrm{cond}}) \tag{2.17}$$

Taking the flow pattern into account, bulk condensation can be described in detail as the sum of condensation related to the phase-separated flow regimes (i.e. annular and stratified flow) and condensation related to other flow regimes:

$$G_{\mathrm{bulk}} = G_{\mathrm{bulk,sep}} + G_{\mathrm{bulk,rest}} \tag{2.18}$$

The contributions from the separated flow regimes describe the phenomenon of condensation at a liquid surface also captured by the wall condensation. Therefore, the minimum of both (i.e. the larger condensation rate since negative) is identified as common condensation mass flow rate:

$$G_{\mathrm{cond,tot}} = \min\left(G_{\mathrm{bulk,sep}}, G_{\mathrm{cond}}\right) + G_{\mathrm{bulk,rest}} \tag{2.19}$$

If follows as total condensation rate:

$$\begin{aligned} G_{\mathrm{cond,tot}} &= \min\left(G_{\mathrm{bulk,sep}}, G_{\mathrm{cond}}\right) + G_{\mathrm{bulk,rest}} \\ &= G_{\mathrm{bulk}} + \min(0\,, G_{\mathrm{cond}} - G_{\mathrm{bulk,sep}}) \end{aligned} \tag{2.20}$$

In accordance with the mass transfer rate between the phases, the energy transfer rate must be adjusted. Previously, the energy transfer was calculated as follows:

$$Q_{\mathrm{cond,tot}} = Q_{\mathrm{bulk}} + Q_{\mathrm{cond}} \tag{2.21}$$

Using the new approach, the fraction of bulk condensation that can be attributed to the separated flow regimes is reduced by the contribution from wall condensation:

$$Q_{\mathrm{cond,tot}} = Q_{\mathrm{bulk}} + Q_{\mathrm{cond}} - \max\left(G_{\mathrm{cond}}, G_{\mathrm{bulk,sep}}\right) \cdot \left(\max(\mathrm{HV},\mathrm{HL}) + \frac{1}{2}\rho {w_v}^2\right) \tag{2.22}$$

2.2.3 Verification against COSMEA

COSMEA is a test facility with a coaxial double pipe to investigate flow characteristics and heat transfer during the condensation of steam in a slightly inclined horizontal tube. It is a sub-section of the thermal-hydraulic test facility TOPFLOW (Transient two-phase flow test facility), at the Helmholtz-Zentrum Dresden-Rossendorf (HZDR). The inner pipe (tube or primary side) is a condensation pipe where hot saturated steam and water flow under high pressure, while the outer pipe (shell or secondary side) is a cooling pipe where cold water passes. The experiment was initially set up and performed in 2012. Further information can be found in /BIE 20/.

There were a few modifications to the test facility in 2020. The inclination was slightly changed from 0.75° to 0.87°. The diabatic and adiabatic lengths between the condensation pipe and cooling pipe were adjusted (Fig. 2.22). The active length for the heat transfer between the condensation pipe and cooling pipe was 2.823 m. The diameters of pipes remained unchanged from the previous facility design – the outer diameter of the condensation pipe is $D_{\mathrm{out,cond}} = 48.3\ \mathrm{mm}$ and the inner diameter of the cooling pipe $D_{\mathrm{in,cool}} = 116\ \mathrm{mm}$. The details of the dimensions of the test section are shown in Fig. 2.22.

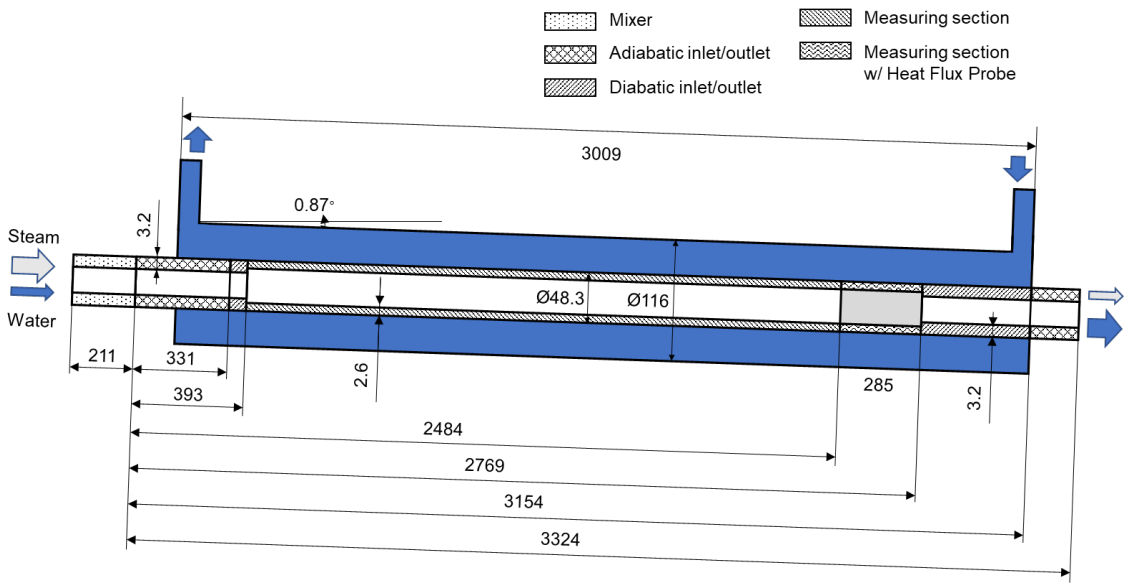

Fig. 2.22 Schematic drawing of COSMEA test facility (2020) (not proportional to real scale)

In the experiment performed in 2020, 26 tests were carried out with changes in pressure from 5 to 65 bar, steam inlet mass flow rate from 0.02 to 1.0 kg/s, water inlet mass flow rate from 0.0 to 0.7 kg/s for the condensation pipe, and water mass flow rate from 13 to 36 kg/s for the cooling pipe. The temperatures and the pressures in the cooling pipe were almost constant values at 43 °C and 3.5 bar, respectively /BOD 24/. Initial and boundary conditions are given in Tab. 3.1. In the experiment, the condensation rate in the cooling pipe, the heat flux between the condensation and cooling pipe and the temperature rise along the cooling pipe were measured when the system had reached a steady state.

Tab. 2.3 Initial and boundary conditions of COSMEA 2020 experiment

	Condensation pipe					Cooling pipe		
Exp. ID	P_{out} (bar)	$T_{L,in}$ (°C)	$\dot{m}_{L,in}$ (kg/s)	$\dot{m}_{V,in}$ (kg/s)		P_{in} (bar)	$\dot{m}_{L,in}$ (kg/s)	T_{in} (°C)
s51r	5.0	0.0	0.00	0.16		3.6	13.5	43.3
s53	5.0	153.6	0.37	0.02		3.5	13.1	43.5
s54	5.0	152.3	0.10	0.02		3.5	13.0	44.7
s121r	12.0	0.00	0.00	0.28		3.6	17.9	43.1
s124	12.0	188.4	0.48	0.04		3.5	13.3	43.7
s125	12.0	188.0	0.48	0.02		3.6	13.3	43.2
s126	12.0	187.8	0.10	0.04		3.5	13.1	43.8
s126r	12.0	187.7	0.10	0.02		3.5	13.0	43.8
s251r	25.0	0.0	0.00	0.55		3.7	25.0	42.9
s254	25.0	224.6	0.70	0.08		3.6	19.0	43.1
s255	25.0	224.7	0.70	0.04		3.6	19.0	43.7
s256	25.0	224.6	0.70	0.02		3.6	15.4	42.9
s257	25.0	219.4	0.10	0.02		3.5	13.7	44.0
s451r	45.0	0.0	0.00	1.00		3.7	33.0	43.0
s454	45.0	257.9	0.70	0.15		3.6	24.0	43.7
s455	45.0	257.9	0.71	0.08		3.6	19.9	42.9
s456	45.0	257.8	0.71	0.04		3.6	18.5	43.2
s457	45.0	257.8	0.70	0.02		3.7	17.5	43.0
s458	45.0	252.8	0.10	0.02		3.6	13.1	43.8
s651r	65.0	0.0	0.00	1.00		3.6	36.3	43.0
s654	65.0	281.1	0.70	0.20		3.7	27.7	43.0
s655	65.0	281.2	0.70	0.15		3.6	26.2	43.0
s656	65.0	281.2	0.70	0.10		3.5	22.5	43.4
s657	65.0	281.2	0.70	0.05		3.6	22.2	42.9
s658	65.0	281.2	0.70	0.02		3.6	18.4	43.1
s659	65.0	274.4	0.10	0.02		3.5	13.1	41.9

The nodalization of the test facility for the simulation is shown in Fig. 2.23. The TFO CONDPIPE is the condensation pipe (primary side), which is fed with water by LIQINLET and steam by the junction in VERBINJT. CONDPIPE is 3.3 m long and discretized into 34 nodes, which yields approximately 0.1 m per node (L/D = 2.4). The mixture of steam and water flows out to the time-dependent volume (TDV) CONDOUT, where the outlet pressure and enthalpy are assigned. The object COOLPIPE is the cooling pipe (outer surrounding pipe). The heat conduction objects (HCOs) shaded in red, purple, grey, and dark green connect CONDPIPE and COOLPIPE to enable the heat transfer between the two pipes. For the heat transfer calculation between inner condensation pipe and outer cooling pipe, the single-phase heat transfer coefficient on the outer side was calculated according to the Dittus-Boelter correlation /DIT 30/. As earlier investigations have shown, the single-phase heat transfer coefficient is significantly underestimated on the shell side /JOB 24/, which might be the result of turbulence introduced by the experimental setup or by wall roughness. To compensate for this effect in the calculations presented below, the HTC on the shell side was increased by a factor of 2.5, which is in line with the measurements and the referenced publication.

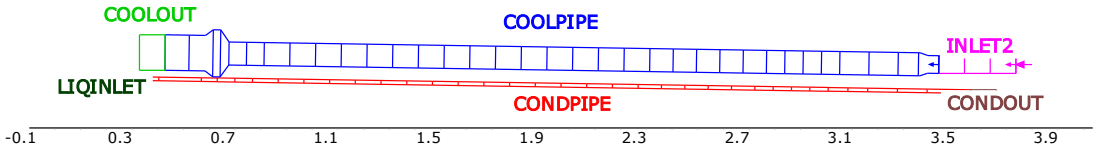

Fig. 2.23 Nodalization of COSMEA facility

The extended implementation yielded slightly improved results for the condensation rate and the condensate temperature at the pipe outlet, as can be seen from Fig. 2.24 and Fig. 2.25. But overall, the condensation rate is still underestimated, while the condensate temperature is overestimated. The only small effect of the new implementation on the void fraction distribution is depicted in Fig. 2.26 for the tests at 45 bar.

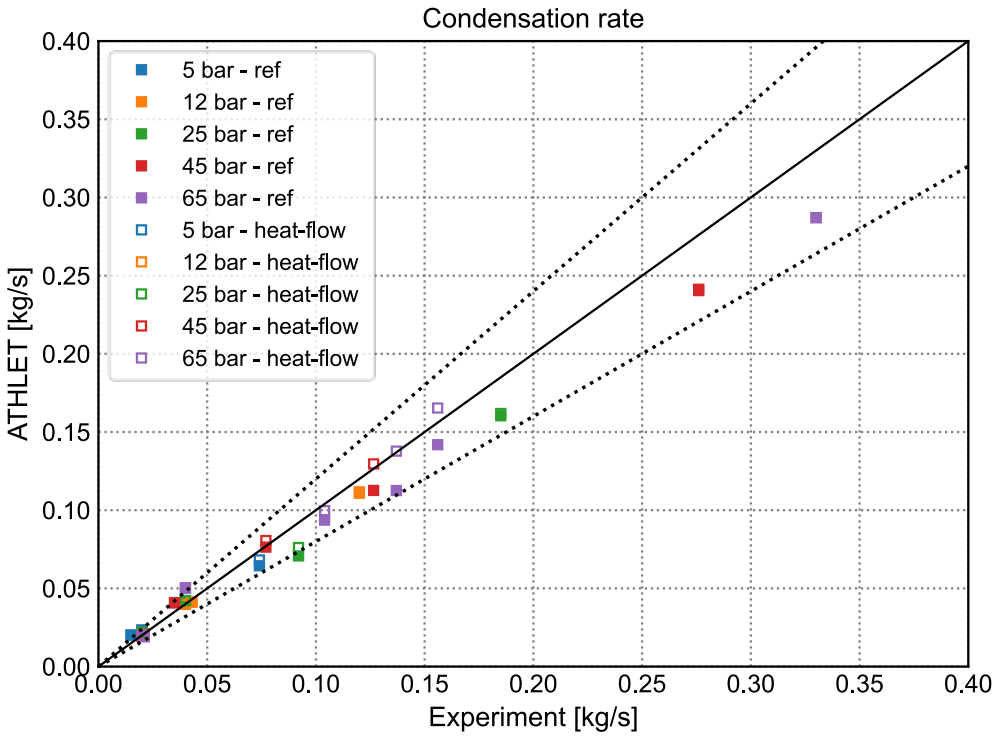

Fig. 2.24 Measured and calculated condensation rate for COSMEA experiment

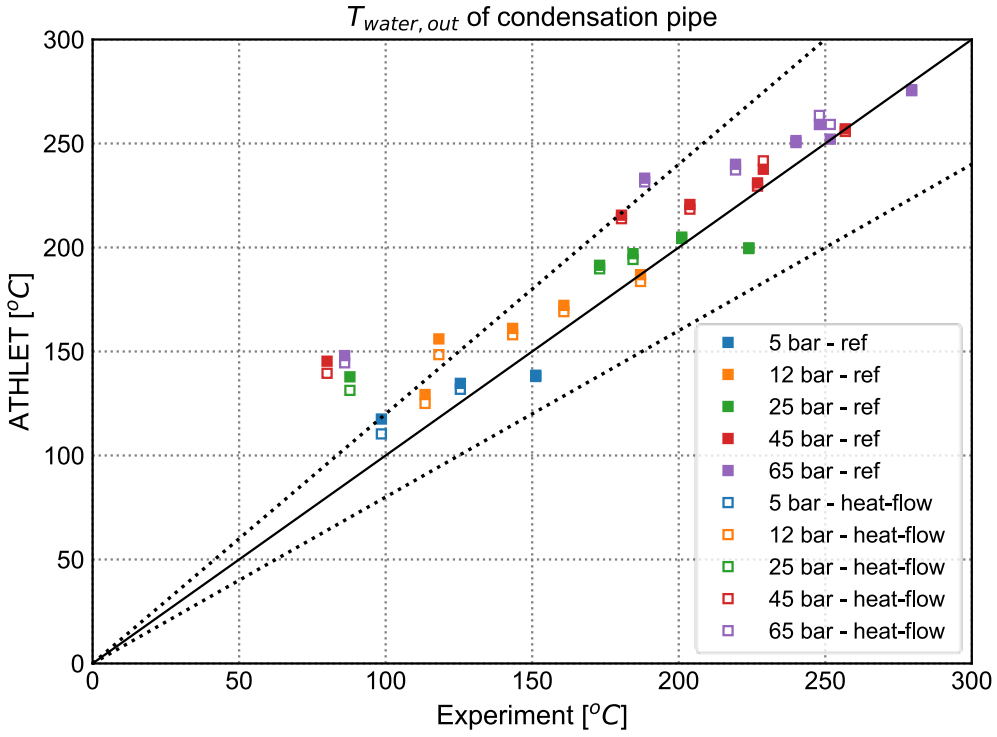

Fig. 2.25 Measured and calculated condensate outlet temperature for COSMEA experiment

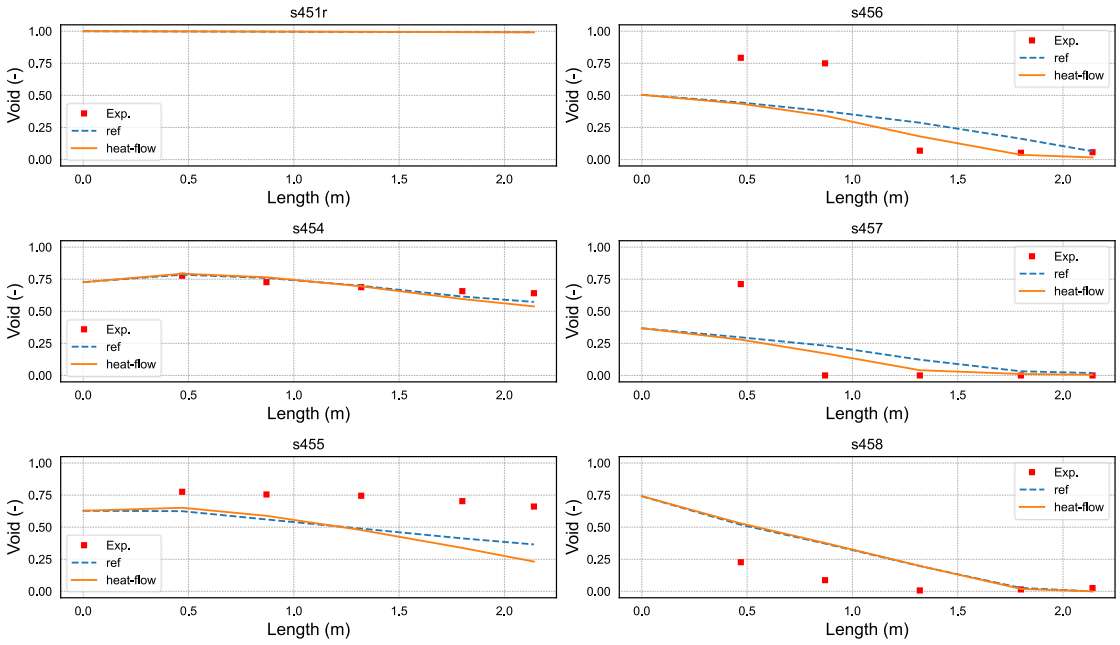

Fig. 2.26 Void fraction along COSMEA condensation pipe

2.2.4 Conclusions

Following conclusions can be drawn from the application of the above-described phase heat flow distribution modelling to the COSMEA experiment:

- Using the FLRM together with the adjusted phase heat flow distribution provided improved simulation results for the COSMEA experiment. Condensation rate and temperature better agreed with the experimental data.
- To further increase the still underestimated condensate subcooling, it seems to be necessary to adjust the bulk condensation model. It was found for COSMEA that a subcooling of only several degrees caused relatively strong condensation of saturated steam, preventing a further subcooling of the liquid phase.
- The impact of the new model on the calculated void profile was rather small. The observed deviations could be rather caused by the interfacial and wall friction modelling for horizontal pipe than by the heat transfer.
- Further validation, also against experiments with vertical pipe orientation, is required, before the extended model for the phase heat flow distribution can be integrated in the main ATHLET development branch.

3 Improved Thermal-hydraulic Modelling

3.1 Cladding Pre-cooling and Droplet Breakup by Spacer Grids during Reflooding

Fuel rod bundles of nuclear reactors such as PWRs are equipped with spacer grids to maintain the fixed distance between the rods. The presence of these spacer grids along the entire rod bundle has significant effects on the reactor core thermal-hydraulic behavior. Due to the induced turbulent mixing, convective heat transfer rate increases significantly downstream of a spacer grid, and such enhancement decreases exponentially away from the spacer grid location (see chap. 4.2). In addition, the droplets entrained in the vapor phase in the DFFB regime do breakup into much smaller ones at the spacer grid locations when spacer grids are dry, leading to significantly increased interfacial heat transfer area and, as a result, further enhancement of the cooling capability can be achieved due to vapor flow accelerating and de-superheating through phase change by droplet evaporation. On the other hand, wet spacer grids serve as potential source for liquid droplet deposition and re-entrainment.

The peak cladding temperature (PCT) usually occurs in the dispersed flow boiling region, where the dispersed liquid droplets exist within the continuous vapor phase. These dispersed droplets have a large surface area-to-volume ratio, providing a significant interfacial area for heat and mass transfer, which results in the cooling of the superheated steam. The steam cooling rate is strongly proportional to the droplet size and number of droplets that determines the interfacial heat transfer area between the dispersed droplets and the continuous vapor phase. An increased cooling of the steam, e.g. induced by droplet breakup at spacer grids, results in an increased wall-to-fluid heat transfer and a reduction of the PCT. Thus, to quantify the amount of cooling enhancement it is necessary to determine the Sauter mean diameter ratio of the droplets downstream and upstream of the spacer grid.

Sugimoto and Murao investigated grid spacer effects on reflood heat transfer in a 6x6 bundle under dispersed and slug flow conditions /SUG 84/. They found that the reduction of droplet diameter downstream the spacer grid can be correlated with the blockage ratio of the spacer and depends on the droplet Weber number. Droplet Weber number represents the ratio of the incoming droplet inertia to its surface tension:

$$\mathrm{We}_0 = \frac{\rho_d \cdot w_0^2 \cdot d_0}{\sigma} \tag{3.1}$$

Yao et al. investigated droplet behavior impacting on hot strips beyond Leidenfrost temperature and derived limiting conditions for the shattering and cutting phenomena /YAO 88/. They could correlate the average size of the generated droplets to the incoming Weber number. Generally, incoming droplets split into two groups of ejected droplet diameters: a group of large droplets (few samples only) with a diameter similar to the incoming droplets, and a group of significantly smaller diameter droplets (large number of samples). The authors estimated the Sauter mean diameter d_{32} of the new droplets as:

$$\frac{d_{32}}{d_0} = A \cdot \mathrm{We}_d^{-B} \tag{3.2}$$

/YAO 88/ give the parameters A and B as functions of the incoming droplet diameter and the width of the strip of the spacer grid. Other authors define constant values /SAL 20/:

$$\frac{d_{s,32}}{d_0} = 6.167 \cdot \mathrm{We}_d^{-0.53} \tag{3.3}$$

3.1.1 Spacer Grid Droplet Breakup Modelling

The droplet number and droplet size distribution mainly impacts the evaporation rate at the droplets' surface. The droplet evaporation rate is calculated according to the Sideman and Plesset-Zwick models as

$$\Psi_{\mathrm{Vol}}^{U_D \neq 0} = \frac{2\ C0}{r} \cdot \Delta T_{\frac{\mathrm{Liq}}{Vap}} \cdot V \cdot (1-\gamma)^{-1} \cdot \left\{6\ \rho_V \cdot c_{p,V} \cdot \lambda_V \cdot U_D \cdot n_D \cdot \alpha \cdot \mu\right\}^{\frac{1}{2}} \tag{3.4}$$

with $U_D = U_{D0} + C1 \cdot \left(\frac{\rho_L}{\rho_V}\right)^{C2} \cdot w_i^{C3}$

with $U_{D0} = 0.15\ \mathrm{m/s}$, $C0 = 1.0$, $C1 = 0.1$, $C2 = 0.0$ and $C3 = 1.0$. V is the volume of the CV and n_D the so-called number of droplets per unit volume.

The correlations for spacer grid induced droplet breakup provide an expression for the ratio of Sauter diameters of incoming droplets d_0 and ejected droplets d_{32}.The Sauter diameter is defined as

$$d_{32} = \frac{6\, V_{\mathrm{tot}}}{A_{\mathrm{tot}}} \tag{3.5}$$

where A_{tot} is the total surface of the droplets and $V_{\mathrm{tot}} = (1-\alpha)\cdot V_{\mathrm{CV}}$ their volume.

The total droplet volume $V_{\mathrm{tot}} = (1-\alpha)\cdot V_{\mathrm{CV}}$ is independent of the droplet size distribution and assumed to be the same downstream and immediately upstream the spacer grid. From the ratio of the Sauter diameters, the number of ejected droplets can be determined:

$$\frac{d_{32}}{d_0} = \frac{A_{0,\mathrm{tot}}}{A_{e,\mathrm{tot}}} = \frac{\sum N_{0,i}\cdot A_i}{\sum N_{e,i}\cdot A_i} = \frac{4\pi\, n_0 \cdot \mathrm{d}_0^2}{4\pi\, n_e \cdot d_{32}^2} \tag{3.6}$$

Here, N_0 and N_e are the number of droplets in the CV upstream the spacer grid and, respectively, downstream the spacer grid. n_0 and n_e are the droplet numbers in terms of droplets per unit volume. Now, following expression can be derived:

$$n_e = n_0 \left(\frac{d_0}{d_{32}}\right)^3 \tag{3.7}$$

Thus, the droplet evaporation rate downstream a spacer grid can be determined using eqs. (3.4) and (3.7) as

$$\Psi_{\mathrm{Vol}}^{U_D\neq 0} = \frac{2\,C0}{r}\cdot \Delta T_{\frac{\mathrm{Liq}}{\mathrm{Vap}}}\cdot V\cdot(1-\gamma)^{-1}\cdot\left\{6\,\rho_V\cdot c_{p,V}\cdot\lambda_V\cdot U_D\cdot n_0\cdot\alpha\cdot\mu\right\}^{\frac{1}{2}}\cdot\left(\frac{d_0}{d_{32}}\right)^{3/2} \tag{3.8}$$

where n_0 is the number of droplets in the CV upstream the spacer grid.

For the droplet size ratio downstream and upstream the grid, the following correlation proposed in /SAL 20/ is employed in ATHLET:

$$f_{32} = \frac{d_{32}}{d_0} = 6.167 \cdot \mathrm{We}^{-0.53} \tag{3.9}$$

The droplet size ratio and its impact on the evaporation rate is considered not only in the CV immediately downstream a spacer grid, but it is transported with the liquid velocity through the CVs of the core channel(s).

3.1.2 Validation against RBHT

The extended spacer grid model has been validated against open tests from phase I of the OECD RBHT (Rod Bundle Heat Transfer) project. In the frame of previous TH analyses during the RBHT project, ATHLET (as well as several other thermal-hydraulic codes) over-predicted the temperature of the rod surface for several test conditions, and the prediction of the quench front progression of the rod bundle diverged from experimental results /OEC 25/.

The investigated experiment was conducted at the RBHT test facility at the Pennsylvania State University. The test section features a 7 x 7 rod bundle with a pitch of 12.6 mm and a heated length of 3.657 m and four unheated support rods in the corners. The 45 electrical heater rods have a diameter of 9.5 mm and feature a skewed axial power profile, where the point of maximum power, located at 2.74 m, constitutes 1.5 times the average heating power, while the end points of the rods equal 0.5 times the average power. The bundle is contained in square housing which measures 91.3 mm x 91.3 mm.

The used input data set is based on the work presented in /DÜN 22a/, /DÜN 22b/. Fig. 2.11 depicts the two-channel nodalization of the RBHT facility. Overall, eleven reflooding tests (O1 to O11) have been recalculated. The tests differed in inlet water subcooling (2.8 to 80 K), bundle power (35 to 252 kW) and reflood rate (0.5 to 15 cm/s). Pressure was fixed at 2.8 bar. Details are presented in Tab. 2.2.

Tests with high, medium and low reflood rates can be distinguished. Exemplary for a high reflood rate is test O3 (15 cm/s). Results are presented in the following figures. Applying the new spacer grid model, improvements could be achieved for the cladding temperature downstream the spacer grid No. 6 location at 2.89 m elevation (Fig. 3.1). The new model is capable to simulate the early precooling of the cladding. This is caused by a reduced vapor temperature due to an increased droplet evaporation as can be seen

in Fig. 3.2. The progression of the quench front (Fig. 3.3) is improved but still slightly underpredicts the experimentally observed quench front velocity.

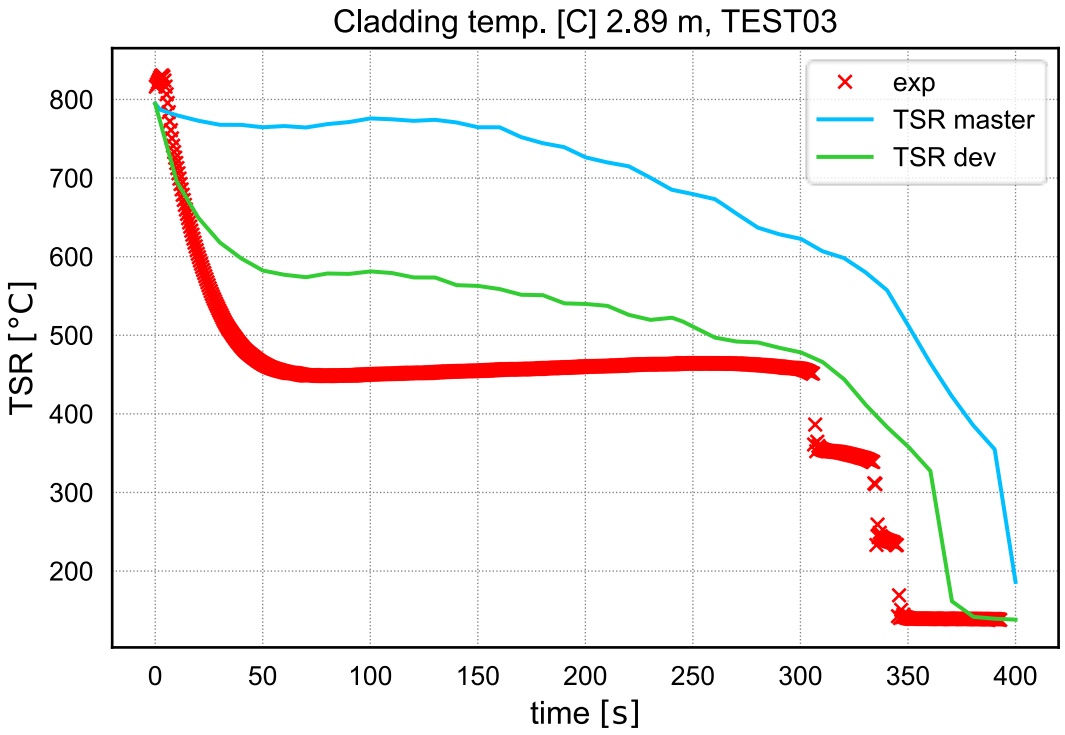

Fig. 3.1 Cladding temperature downstream spacer grid No. 6 for RBHT test O-3

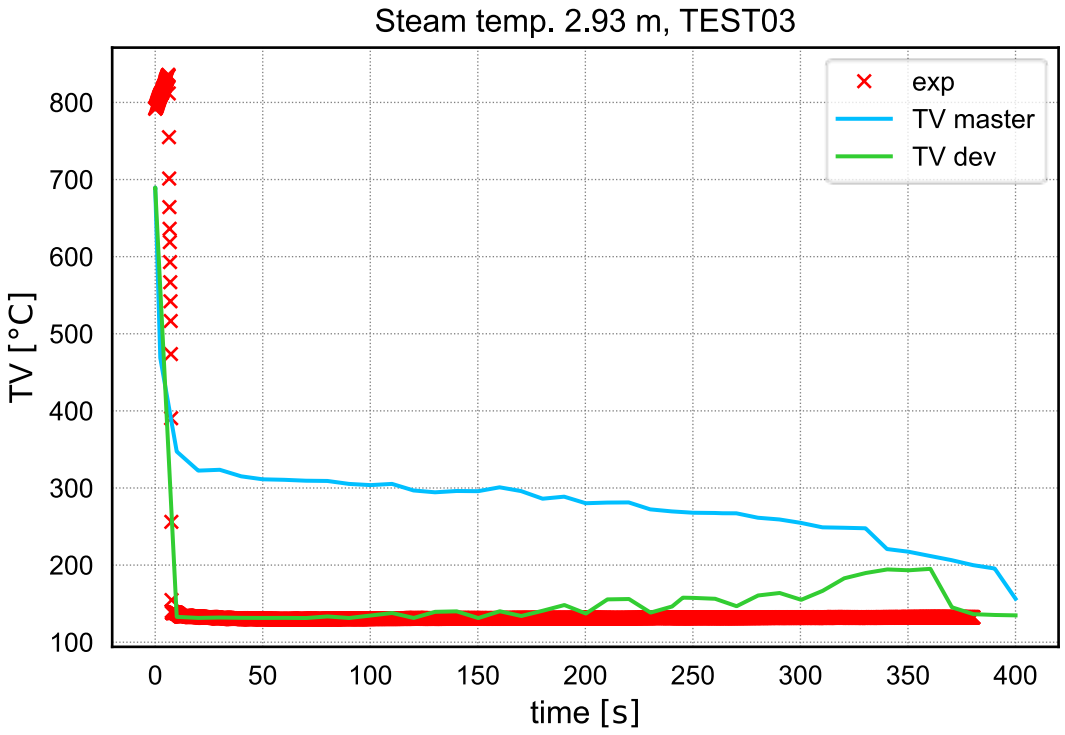

Fig. 3.2 Steam temperature downstream spacer grid No. 6 for RBHT test O-3

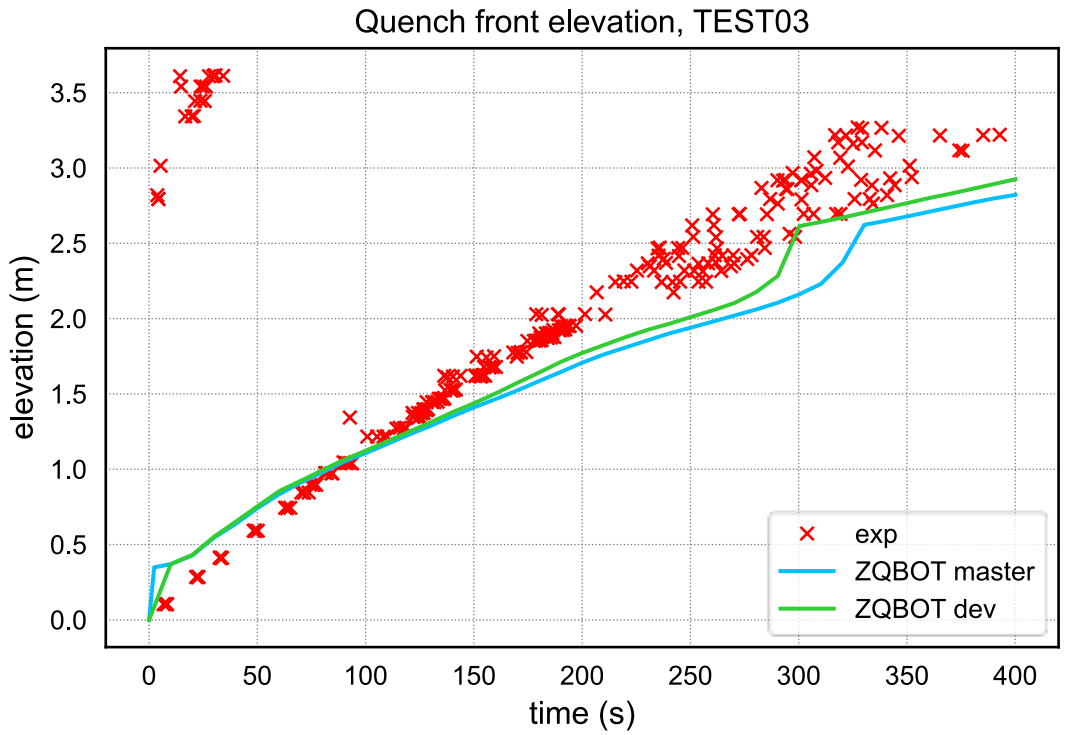

Fig. 3.3 Quench front position for No. 6 for RBHT test O-3

A good example for medium reflood rate (2.5 cm/s) is test O6. Again, the prediction of the surface temperature downstream the spacer grid No. 6 position is improved by the application of the new spacer grid model (Fig. 3.4). For tests with low reflood velocity, the impact of the new spacer grid model with consideration of droplet breakup is small due to the very low entrainment fraction.

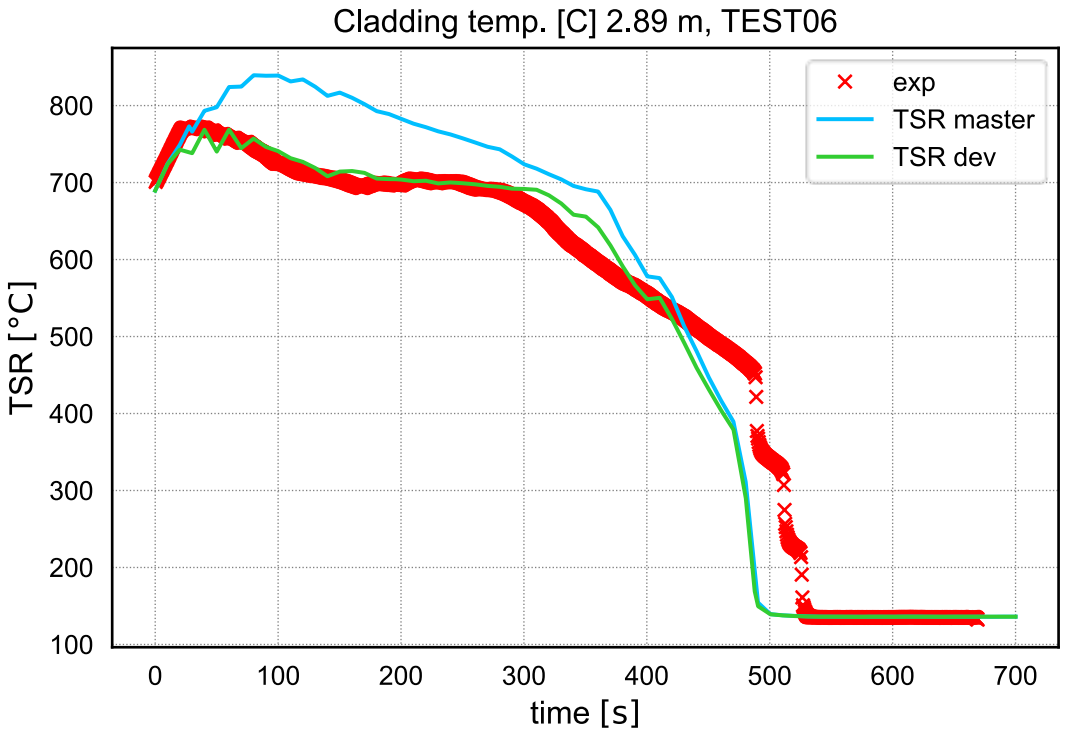

Fig. 3.4 Cladding temperature downstream spacer grid No. 6 for RBHT test O-6

3.1.3 Summary

Recalculations of RBHT experiments on core reflooding were analysed in detail to determine the causes of observed deviations with regard to the pre-cooling of the rods' surface before quenching. Pre-cooling is achieved by convective heat transfer to a vapour-droplet flow under DFFB conditions during reflooding of the core. The vapour is cooled by evaporation of the entrained droplets, which eventually increases the wall heat transfer. In ATHLET, the evaporation rate of the entrained droplets has been underestimated in the past. Main reason was that the spacer grids in the core, which cause the splitting of droplets and an increase in the interfacial area, were not taken into account. Now, the implementation of the 2-fluid model of ATHLET has been supplemented so that the influence of the spacer grids on the number and size of the droplets can be taken

into account. The extended model basis has been validated against RBHT tests and provided improved numerical predictions when compared to experimental data, particularly for medium to high reflood rate conditions. A more detailed simulation of the influence of the spacer grids could be achieved in future by modelling a dedicated droplet field, as could be done, for example, within the framework of a 3-field model.

3.2 Simulation of Non-condensable Gases

In several production calculations as well as test examples, small amounts of one or more non-condensable gases transported in the ATHLET domain (e.g. in areas with subcooled water under a mixture level) have led to time step limitations. For this reason, it was investigated if removing such residual amounts of non-condensables, including the overall gas phase, would stabilize calculations. To that end, cut-offs for non-condensables and overall CV quality were implemented in the code. In the default setting, ATHLET employs a vapour phase cut-off quality value of 10^{-30} in `dxmlim`. Based on tests, the following insights have been gained.

- Removing non-condensable gas quantities during FEBE time step integration is impossible as this leads to inconsistencies in the integration flow. This particularly forecloses attempts to prevent the transport of small quantities of non-condensables by destroying these during integration.
- Going to higher cut-off-values has no positive impact on numerical performance, and cut-off values higher than about 10^{-20} are often detrimental.
- Small amounts of non-condensables and inconsistencies in non-condensable gas concentration in a noticeable fraction of cases are artefacts of FEBE integration at approximation order 3. This happens if NC gas qualities do not change for the second sub-step, but only for the third and final sub-step. In this case, the extrapolation can be very volatile; addressing that would require to (re-)activate higher approximation orders or similar interventions in the integration flow. This is deemed impractical.

For FEBE integration, ATHLET integrated the non-condensable gas qualities for all gases activated in a CV irrespective of the value of their qualities, if non-condensables were present and integrated in the CV. That has the potential of limiting the ATHLET time step if small gas qualities are changing in the time step (see also the remark on extrapolation issues above). For this reason, the control of FEBE integration was improved by defining the NC-gas specific variable `TOPNCICV` that allows to switch off the

integration for individual non-condensables beyond the first gas. For quality values below 10^{-20}, FEBE integration of the solution variable will be switched off. For the overall gas quality of non-condensables, the threshold is 10^{-28}. Suitable set-points for reactivating equations have been defined. This change has demonstrated small benefits in terms of time step behaviour and has the additional advantage that it reduces the numerical effort by a small amount. Relevant data are stored in the restart file to ensure restart capability.

3.3 Extended Critical Discharge Model

The critical discharge model of ATHLET, CDR1D, had been extended by a new option to consider the drift between the phases in the past /SCH 18/. The underlying 4-equation system uses the following correlation for the phase slip:

$$S = 1 + \frac{3}{2}\sqrt{3\alpha}\,(1-\alpha)\left(\left(\frac{\rho_l}{\rho_v}\right)^{1/3} - 1\right) \tag{3.10}$$

Relative velocity is also considered for the calculation of the evaporation rate, for which the standard bulk heat and mass transfer model of ATHLET is used.

Now, the extended model has been numerically improved and transferred into the main ATHLET code version, so that it becomes available to all code users. The extended model can be activated via user input under the control word `DISCHARGE` (input parameter `IAUR`=5). Preliminary validation has been performed against Super Moby Dick experiment, where two nozzle geometries were investigated, sudden expansion and diffusor. Particularly for saturation conditions at the inlet, the new model predicts discharge rates that are in better agreement with the experimental data than the old model (Fig. 3.5 and Fig. 3.6).

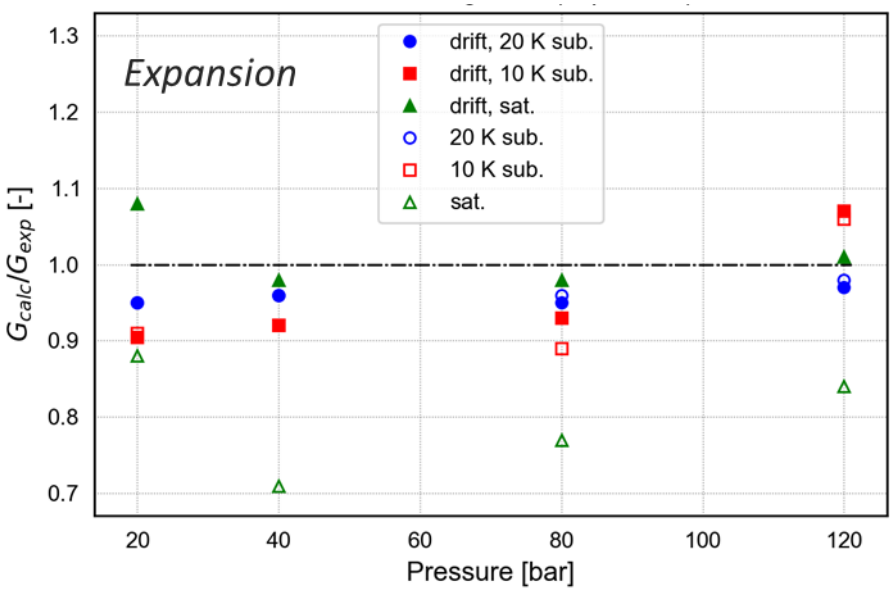

Fig. 3.5 Discharge rates for Super Moby Dick experiment with sudden expansion

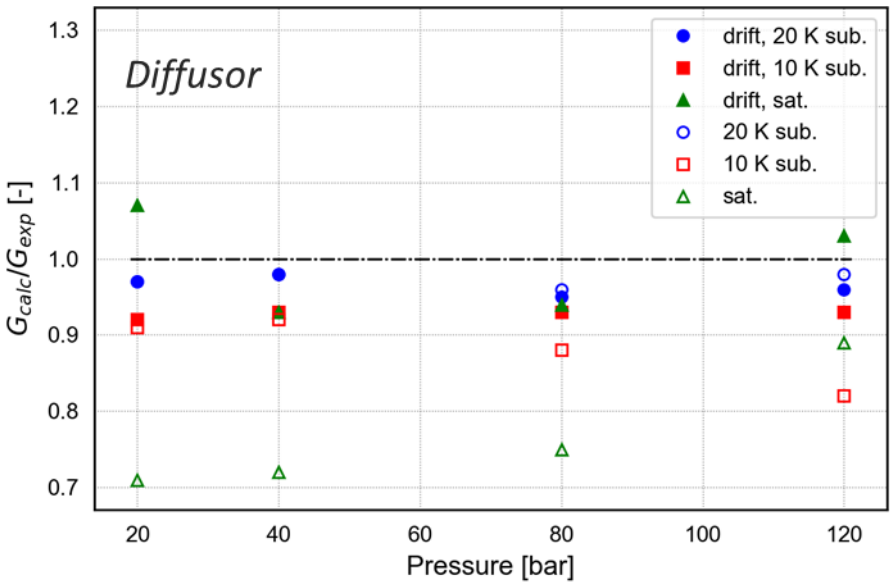

Fig. 3.6 Discharge rates for Super Moby Dick experiment with diffusor

3.4 Thermal-hydraulic Simulation of ECC Injection Systems

In the past occasional program aborts could be observed which had their origin in system domains with sub-cooled water, e.g. the ECC injection system. The work carried out was aimed at analyzing the underlying errors in detail and, where necessary, improving the implementation in order to achieve a more robust simulation of such systems.

One investigated error observed with a user input deck was caused by a combination of the ATHLET 5-equation model with a cyclically opening and closing check valve. For an abruptly opening/closing valve, the time step size controlled by the ATHLET internal ODE solver FEBE should actually be limited in order to avoid numerical problems. But this was not effectively implemented for the 5-equation model. The implementation could be successfully adapted so that fast acting valve behavior can be robustly simulated.

Furthermore, the error notifications of several previous simulations were analyzed, which had led to program stops in the ECC injection system. Many of these simulations showed a uniform error pattern, pointing at an issue with evaporation/condensation at very low pressure and very low vapor content, which could e.g. be induced by pressure waves passing through system domains with subcooled water. Fig. 3.7 illustrates the condition, which are determined by cold water (TL=30 °C), low vapor quality (XQM=1.D-10) and reduced pressure (PRESS=3600 Pa) where mass transfer processes at the phase interface finally resulted in vapor temperature below the allowed range (TV=-460 °C).

```
DPRPLV: VAPOUR TEMPERATURE OUT OF RANGE! CV=  3270 IFLUID= 1 TIME= 2.90582D+01
TL(I)= 2.99999D+01 TV(I)=-4.65612D+02 PRESS(I)= 3.65098D+03 XQM(I)= 2.47579139D-10 NFKEY =   4
HXX IN DPRPLV: RANGE OF PROPERTY APPROXIMATION EXCEEDED. NFKEY =   4
HXX IN FIMP, NFKEY =  4 T = 2.90582D+01 DELTA = 6.85291D-07
FECK: HXX -> CHANGE OF TYPE OF DISCRETIZATION.   OLD DT = 6.85291D-07  NEW DT = 2.28430D-07   AJ = T
FEBE: SUGGESTED STEP SIZE DELTA=  8.44220D-09 IS SMALLER THAN MIN(GRESCH,GRE), WHICH IS  1.00000E-08
```

Fig. 3.7 ATHLET Error Message

Another potential improvement to the program, which could be implemented in the future concerns the ATHLET-specific handling of evaporation processes at low pressures below approximately 10 bar. At such low-pressure conditions, the evaporation rate is artificially reduced aiming at avoiding pressure oscillations caused by volume expansion. However, if this is done under conditions with a negative pressure gradient, the reduction of the evaporation rate could intensify pressure oscillations instead of dampening them, as the pressure decrease in the CV can hardly be supported by evaporation. If necessary, in the future, the implementation of the bulk evaporation mode could be analyzed in more detail and adjusted.

4 Modelling of Structures and Internals

4.1 Horizontal Plate Model

In ATHLET, a HCO is always coupled along the axial direction of the corresponding TFO. Typically, HCOs represent walls of pipes, or rods inside a core channel, thus this is the natural orientation. However, for several applications, including modelling a vessel lid or bottom, a pool bottom, or a tie plate, this rule turned out to be too restrictive and could lead to limited accuracy of the model. Fig. 4.1 exemplary depicts the situation for the core support plate. In a multichannel RPV model, the bottom core plate should be represented by several horizontally oriented HCOs, which are connected at their top to the vertical core channels and at their bottom to the vertical lower plenum channels.

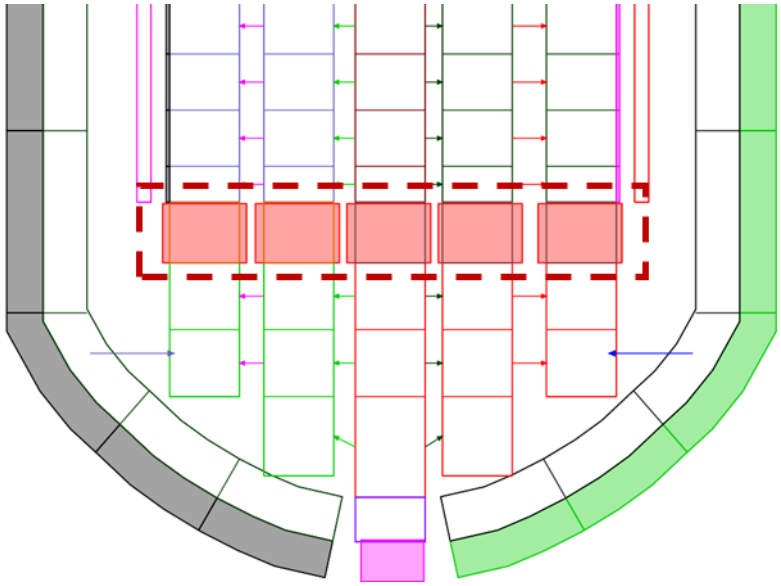

Fig. 4.1 Horizontal HCOs representing the core bottom plate (shaded red) with adjacent vertical TFOs for the core and lower plenum region

Therefore, the implementation of HCOs in ATHLET was extended to allow orthogonal coupling of a strictly horizontal plate-type HCO to a strictly vertical section of a TFO. Such plate-type HCOs always consist of a single HCV. For cylindrical- and spherical-type HCOs, this option is not available.

General orthogonal coupling to inclined or horizontal TFOs is not possible so far. Furthermore, a HCO with orthogonal coupling on one side cannot be coupled in the standard way (along the TFO axis) on the other side, while orthogonal coupling on both sides is

possible. The supported coupling scenarios are illustrated in Fig. 4.2. The red dashed line inside the single HCV (orange) indicates a layer boundary. Like any HCO the horizontal plate HCO may consist of an (almost) arbitrary number of material zones and layers.

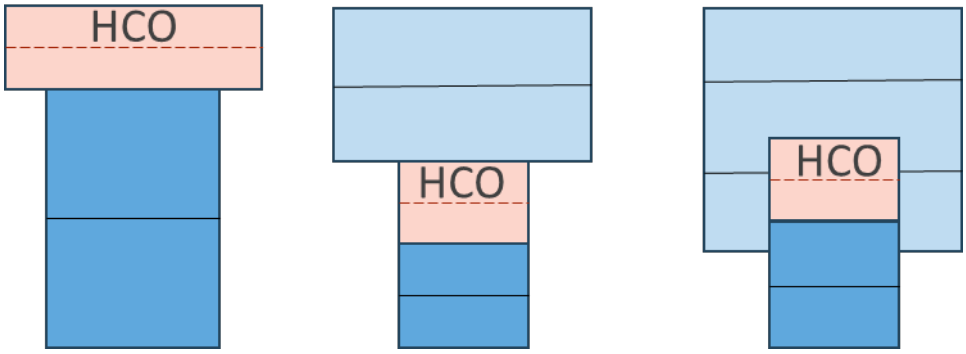

Fig. 4.2 Supported options for the coupling of horizontal plates:
Left: one-sided horizontal coupling. Center: two-sided horizontal coupling.
Right: two-sided horizontal coupling, at one side inside a TFO CV.

Only a limited number of HTC correlations specifically for horizontal plates can be found in literature. For natural convection of liquid or vapor at the upper or lower side of a horizontal plate, the Churchill correlation /VDI 13/ has been implemented, while in other heat transfer regimes the standard HTC correlation package of ATHLET is applied.

For coolant heating at the upper surface (cooling at the lower surface), the heat transfer coefficient for laminar flow is calculated by:

$$\mathrm{htc}_{\mathrm{lam}} = 0.766\,\frac{\lambda}{L}\,[\mathrm{Ra}\cdot f_2(\mathrm{Pr})]^{\frac{1}{5}} \tag{4.1}$$

For turbulent flow, the equation

$$\mathrm{htc}_{\mathrm{tur}} = 0.15\,\frac{\lambda}{L}\,[\mathrm{Ra}\cdot f_2(\mathrm{Pr})]^{\frac{1}{3}} \tag{4.2}$$

is used, with the Rayleigh number Ra, the Prandtl number Pr, the heat conductivity λ, the characteristic length L (plate area divided by breadth), and

$$f_2(\mathrm{Pr}) = \left[1 + \left(\frac{0.322}{\mathrm{Pr}}\right)^{\frac{11}{20}}\right]^{-\frac{20}{11}} \tag{4.3}$$

The boundary between the laminar and turbulent regime is set (though differently given in the literature) at $\mathrm{Ra} \cdot f_2(\mathrm{Pr}) = 204659$ which results in a steady transition.

For coolant heating at the lower surface (cooling at the upper surface), only a correlation for laminar flow (validity range) is available:

$$\mathrm{htc}_{\mathrm{lam}} = 0.6\,\frac{\lambda}{L}[\mathrm{Ra} \cdot f_1(\mathrm{Pr})]^{\frac{1}{5}} \tag{4.4}$$

with

$$f_1(\mathrm{Pr}) = \left[1 + \left(\frac{0.492}{\mathrm{Pr}}\right)^{\frac{9}{16}}\right]^{-\frac{16}{9}} \tag{4.5}$$

As no other correlation is known in the literature, this correlation is also applied in the turbulent regime.

4.2 Convective Heat Transfer Enhancement by Spacer Grids

The heat transfer in the reactor core is significantly improved by spacer grids. So far, the positions of the spacer grids could be specified in the ATHLET input data set, but their influence has only been taken into account (optionally) in the calculation of the critical heat flux if the Groeneveld look-up table were used. But for the calculation of the wall-to-fluid heat transfer, the detailed impact of a spacer grid on single-phase convective heat transfer was not considered.

Due to the induced turbulent mixing, the heat transfer rate increases significantly down-stream of a spacer grid, and such enhancement decreases exponentially away from the spacer grid location. Yao et al. /YAO 82/ performed single-phase flow and dispersed flow experiments to analyze the characteristics of heat transfer for simple egg-crate type

spacer grids in a fuel bundle. They recommended a correlation for heat transfer evaluation downstream to the spacer grid, which considers the axial distance behind the spacer (z) in dimensionless form and the blockage ratio (ε). The Nu number for a rod bundle with spacer grid $\mathrm{Nu}_{\mathrm{spacer}}$ is expressed in terms of the Nu number of the same rod bundle without grid Nu_0:

$$\mathrm{Nu}_{\mathrm{spacer}} = \left(1 + 5.55\ \varepsilon^2 e^{-0.13(z/d_h)}\right) \cdot \mathrm{Nu}_0 \tag{4.6}$$

Several authors reported that the single-phase pressure loss coefficient could be a more meaningful parameter than the blockage ratio to correlate the heat transfer enhancement. Since different types of support grids (even at comparable blockage ratios) produce different heat transfer enhancement, Holloway et al. /HOL 08/ proposed a correlation that considers the pressure loss coefficient instead of the blockage ratio. This correlation is claimed to capture all types of spacer grids with reasonable accuracy:

$$\mathrm{Nu}_{\mathrm{spacer}} = \left[1 + \left(0.8\ K_g - 0.4\right) e^{-0.25(z/d_h)}\right] \cdot \mathrm{Nu}_0 \tag{4.7}$$

In order to enable the consideration of different spacer grid types, both correlations have been implemented in ATHLET. To use Yao's correlation, the input data format has been extended so that the user can provide the required blockage ratio of the spacer grid. The pressure loss coefficient K_g, which is necessary to adopt Holloway's approach, is calculated from the zeta value for the respective spacer grid, which has to be provided by the user in the input deck.

$$K_g = \xi \cdot \mathtt{AMIJ}^2 \tag{4.8}$$

Fig. 4.3 depicts a comparison between Yao's and Holloway's correlations in terms of the heat transfer enhancement factor that can be defined as $f_e = \frac{\mathrm{Nu}_{\mathrm{spacer}}}{\mathrm{Nu}_0}$. Holloway allows to distinguish between different grid types by specific pressure loss coefficients. Exemplary values for pressure loss coefficients K_g for egg-crate, disc, and vane spacer grids were taken from /HOL 08/:

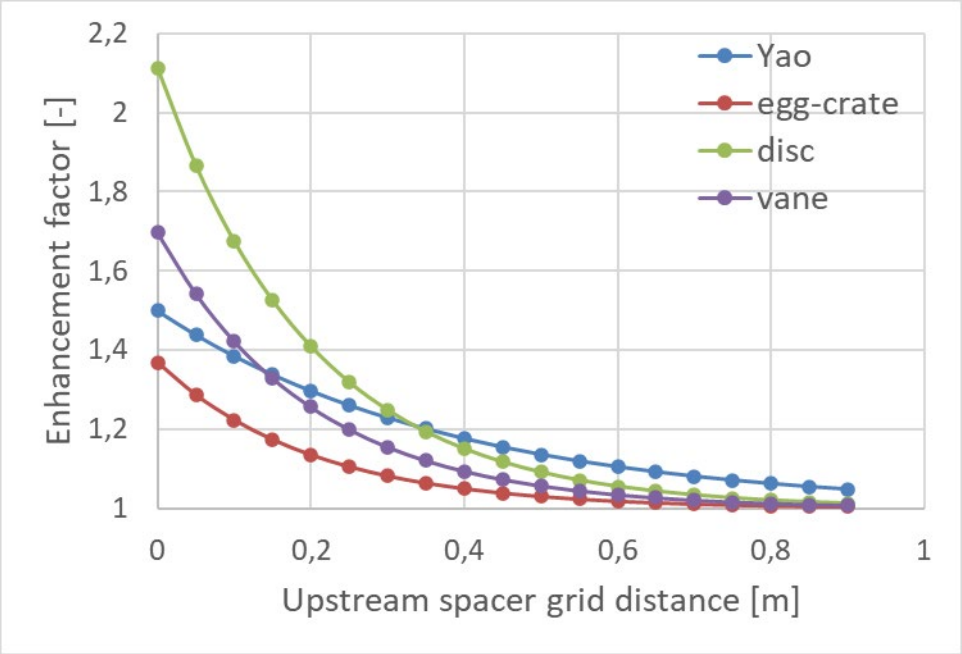

Fig. 4.3 Comparison of convective heat transfer enhancement factors for different spacer grid types

From Fig. 4.3 it can be seen that the Yao model (originally developed for egg-crate type spacers) and the Holloway model with egg-crate typical pressure loss coefficient provide qualitatively similar results. Considering higher pressure losses induced by e.g. mixing vanes using Holloway's correlation enables the calculation of significantly higher heat transfer enhancement factors, which are typical for vane and disc type spacer grids.

5 Improved Program Handling and User Friendliness

5.1 New Options for Friction Loss Adaptation

During the steady-state calculation, all friction and form loss values are adapted if necessary (within certain limits). The adjustment is applied uniformly within a given priority chain (PC) by multiplying the friction and form loss values of all junctions in that PC by a constant factor. A new mechanism has been introduced at the request of internal users to give finer control over how pressure loss adjustments are handled during the SSC. In large systems, global pressure loss values are often uncertain, while high-quality measurements may exist for specific components. Previously, users had only two choices: either enable pressure loss adaptation for the entire priority chain, thereby modifying even the well-characterized components, or disable adaptation entirely, which forced the user to manually provide sufficiently accurate friction loss values for every junction in the PC. This made system initialization significantly more difficult and partly inaccurate. Thus, the aim of the development undertaken was to introduce a possibility to restrict friction loss adaptation to areas where information on pressure loss is incomplete or unreliable.

The new code extension optionally allows the user to specify in the input data set, either for a complete TFO or for selected junctions within a TFO, a weighting factor for the adjustment of the friction losses. This factor can range from 0.0 to 1.0. The default values are 0.0, i.e. adaptation is disabled for the priority chain by global input settings, or 1.0, i.e. adaptation is generally permitted for the PC. These global settings are overwritten by the optional TFO- or junction-specific user input under the newly introduced pseudo keyword `SSCFRIC`. The effective degree of friction and form loss adjustment at a given junction is determined by the ratio between its local weighting factor and the maximum weighting factor assigned to any junction within the same PC.

5.2 Input Data Analysis and Extended Input Data Checks

During input processing, user input for options and model parameters under several CWs are checked against recommended values or default settings in the ATHLET Input Data Description. This includes options such as `ICPUTM` for time measurement under CW `CONTROL`, the inertia term `A1V` for valves under CW `VALVE` or the interfacial heat and mass transfer model selection `IGKV` under CW `EVAPORATE`. If differences to the

recommended values are found an information is written to the log file that refers to the respective input data set line (s. Fig. 5.1).

This new feature facilitates detecting (potentially unintended) deviations between input deck and recommended or default settings of ATHLET and thus assists the users in maintaining and quality assuring the input data.

```
FINPUT: Recommended value for ECKSCH is >= 100 * GRESCH, here:   1.00000000E-06 but GRESCH = 1.00000000E-07
        in input line 757

FINPUT: Recommended value for ITYPTS is 1 but ITYPTS = 0
        in input line 757

DIMISC: Recommended value for AA is   0.00000000E+00 but AA =   4.00000000E+00
        in input line 790
```

Fig. 5.1 Excerpt from the log file containing information for the user on non-default input parameter settings

Additional input data checks and related print messages were added to the ATHLET code, e.g. for following models:

- Input for rod model and TRISO particles
- Input for vessel module
- More detailed input checks for `FUNGEN` controller type under GCSM:
  - If the parameter `EPSCON`, which is used for a time step control at signal discontinuities of logical controllers, is given, the specification of this controller (e.g. a switch) under `X2NAME` is mandatory. If `X2NAME` was not provided, the previous implementation resulted in an array bound violation.
  - If `X2NAME` is not given, the input parameter `IOPT` must be -2 or 0.

5.3 New Input and Output Options

5.3.1 Input Data Extensions

- A new optional input data check for (possibly unintentionally) unused parameters has been implemented. The check can be activated under CW `SERVICES`, PW `IDLE_PARAM` and contributes to the quality assurance of the input deck.

- As additional process signal, the minimum DNB ratio `DNBRMIN` has been made available, so that it can be used as input to the control system defined in the input data set.

- The new possibility to group priority chains under the CW `TOPOLOGY` by means of optional sub-keywords (SW) has been introduced. This feature can be used for an extended configuration control by easily switching on/off whole sets of PCs defined in the input deck.

- Up to now, the output values of GCSM signals were not accompanied by units. For both process signals (derived e.g. from physical quantities in the simulated system) as well as several GCSM controllers, e.g. the `PROP` controller providing material properties, default units have been added to the output data (key file or hdf5 output). Furthermore, for any user-defined GCSM controller, an output unit (e.g. kg/s) can be specified as an optional input string `AGUNIT` in the third, optional input card of the signal. The unit information is automatically used by post-processing tools like ATLAS in the generated diagrams.

- Mass integration control with input `QQ` under CW `MISCELLAN` has been changed. `QQ` is interpreted as a time step value above which implicit integration values for masses will be used instead of the explicit values. For the default setting of `QQ` = 0.0, explicit integration mass values are used throughout. Tests have found that integration efficiency is improved for larger time steps with `QQ` $\gtrsim$ 10 ms. As expected, large time steps profit from using implicit integration, whereas small time steps are stabilized using explicit values.

- The processing of parameters has been made more flexible. When a string-valued parameter is used to represent an active SW or PW string (e.g. `-----`) or an inactive PW string (`-*---`), the latter is not detected during preprocessing of the input deck (before parameter values are replaced). Thus, inactive PW (and SW) represented by parameters and their input blocks are not removed from the effective input deck. And consequently, parameters standing for active keywords do not end inactive code blocks during input preprocessing. Generally, ATHLET input processing is not reliably detecting deactivated SW and PW not removed from the effective input deck. Under CW `TOPOLOGY` and `HEATCOND`, both active and inactive SW can be used via string-valued parameters since ATHLET version 3.5. And under CW `GCSM` both PW (GCSM blocks) and SW (signals) can be controlled via such parameters. Finally,

PWs under CW OBJECT, HEATCOND and ROD can also be controlled via string-valued parameters.

- The input processing for KW under CW OBJECT, CW HEATCOND and CW ROD was refactored to harmonize the effect of COPY directives for the next release version. Consequently, a COPY directive consistently will copy all data from the master object (TFO, HCO; ROD) that are not overwritten by PW input for the specific object. This extends the behavior for default TFO types also to HCO and ROD objects.
  This also allows to mix PWs from a master TFO with PWs for the current TFO for CCO objects. However, for the special component models PRIZER and SECONDARY, no copy is allowed.
  For ROD objects, the COPY directive per default copies not only the PW from the master ROD but also its power profile. Previously, only the copy of power profiles was possible.
  For more flexibility, the additional directive COPY_ONLY can be specified, allowing to select PROFILE for the previous behavior, and PW for skipping the master object power profile and copying only the PW. In the latter case, the current rod must provide its own power profile.
  Additionally, also power profiles for rods can be copied that consist of multiple HCO – provided the rod objects are congruent. Via the additional directive COPY_HCO, the list of HCO in the power profile of the master rod can be replaced by the provided HCO names in their order of input.
  Finally, it is also checked if every HCO assigned to a ROD object is present in its power profile, which protects against input errors where the same ROD object is assigned to multiple HCO inadvertently.

- If liquid water comes into contact with HCOs with surface temperatures (far) exceeding the spinodal values imposed by ATHLET (saturation temperature + 100 K) or the critical temperature, the water property package would not be able to provide a valid value for the (superheated) liquid water phase, leading to simulation stops. The procedure dprplv was refactored so that it now provides more or less arbitrary but numerically (and physically) reasonable values to continue the calculations as long as the amount of liquid water in the CV is sufficiently small. This is particularly important for severe accident calculations.

- For simulations of reactors system in space applications, the new KW `GRAVITY` was added under CW `MISCELLAN`. Here, a fixed value for the local gravity and also a GCSM signal controlling local gravity over time can be provided.
- The parameter `FQDCH` under CW `ROD` describes the fraction of the core neutron power deposited directly in the coolant. This fraction is applied to all rods in the model, irrespective of type, and it applies to the full rod power and not only to its fission power. The actual physical effect of direct coolant heating, however, does depend on the (average) density of the coolant in the core. And it does depend on whether there is neutron power or if there is only decay power (long) after reactor shutdown. For this reason, an additional optional input `AFQDCH` was added to specify a GCSM signal, which provides the value for `FQDCH` throughout the transient calculation. This allows to simulate a more realistic time evolution for the direct coolant heating fraction.

5.3.2 HDF-5 Output Data Format

In phase A of the project, some basic geometry data were added to the HDF5 file to support advanced plotting, like distribution plots along objects, e.g. using the Batchplot extension ac2.athlet. Furthermore, the information about the physical unit of the variables, which was available so far only in the key file, was written directly into the HDF5 file. Technically, the HDF5 feature to store attributes next to the tables with the actual values of the variables was used. The units in the HDF5 file are automatically displayed in ATLASneo, and they are also read by ac2.athlet. In phase B of the project, a few more geometry data were added.

During calculations with large facility datasets with extensive GCSM modelling, a dramatic increase in runtime was reported by users inside GRS when using the HDF5 output format in version 3.4 of ATHLET, both in comparison with earlier versions and with runs using the same version 3.4 without HDF5 output. By tracking the version history, it was determined that this performance loss can be observed since the addition of geometry data and unit information to the HDF5 output. However, the effect is minor in calculations with typical test data sets, so it went unnoticed at that time. Further testing specifically identified the presence of the HDF5 attributes with the unit information as the root cause for the performance loss. However, no obvious errors or deviations from the recommendations by the HDF5 developers could be identified in this type of unit storage. The problem was resolved by disabling support for earlier versions of the HDF5 library in ATHLET

when writing the HDF5 file. The reason for the performance loss may thus be an inadequacy of earlier versions of the HDF5 library. Since all GRS internal tools (Batchplot, ATLASneo) and the most used external tools (HDFView and the Python packages pytables and h5py) also support the current version of the HDF5 library, no restrictions are expected in practical applications.

Some changes in the internal structure of the HDF5 file were applied to make the data access more systematic, for the user and for tools like ac2.athlet. In particular, the output tables of library signals, like those of type `POSTPRO`, `LEVEL`, and others, are not stored anymore like standard GCSM signals below the group `/plotdata/GCSM`, but because of their different nature and output under the new group `/plotdata/GCSMLIB`.

The sorting of the output data in the HDF5 file into groups like `/plotdata/TFO`, `/plotdata/HCO` and others is based on the scope mechanism in ATHLET which is provided by the *libfde*. Data that do not fall under any of the supported scopes are automatically stored under `/plotdata/other`. With the SAFT model being now an integral component of ATHLET, a new `SAFT_scope` has been introduced, and the data of this model are now consequently stored under `/plotdata/SAFT`. Some names of the SAFT output variables were adjusted to be in better alignment with ATHLET naming schemes. In addition, fission product data are written to `/plotdata/FPSUM`.

The Batchplot extension ac2.athlet was extended and allows now convenient access to GCSM library quantities and also supports e.g. distribution plots along SAFT objects (see the detailed description in 5.4.1).

5.3.3 Output of GCSM signals units

For all GCSM signals, the unit has not been written into the key file so far. While this is justified for many signals with unknown units, the units of process signals are well defined and now stored correctly. In addition, units of GSCM signals specified by the user via the new input option are now recorded as well. The same applies for the HDF5 output, and both output files have been updated accordingly.

Furthermore, for several GCSM library models like `LEVEL` (collapsed level calculation) or `POSTPRO` (post-processing options), the units are now written to both the key file and HDF5 file as well.

Furthermore, the print and plot data have been extended by:

- Additional quantities under keyword `MONITOR`: `IJLIM` and `IJRED` denote the indexes of the time step size limiting junction/CV and the time step size reducing junction/CV, respectively.
- ATHLET enables the consideration of reactivity feedbacks by thermal expansion of structures (represented by HCOs) or fluidic domains (TFOs). The average temperature of CVs or HCVs taken into account for the calculation of thermal expansion feedback reactivities has been added to the print and plot quantities.
- Print and plot output of the prevailing flow regime in both junction and CV.

5.4 Software Utilities

ATHLET comes with various software utilities to support both the program users as well as the program developers. The tools have been extended to meet current user needs.

5.4.1 Batchplot Plotting Tool

The AC^2 tool "Batchplot" for the script-based generation of graphical representations of simulation results was previously restricted to the processing of HDF5 files. Moreover, the user had to be aware of the internal data structure of ATHLET's HDF5 output. Therefore, changes to this structure could not be made without breaking user code. There was also no easy solution for combining simulation data from restart files.

In order to address these issues, the sub-package "ac2.athlet" was developed for Batchplot. It contains the class "AthletOutput" which is designed to serve as a unified interface for accessing all ATHLET output data. Data access is based on the names of objects and variables and thus is independent of the data storage model. In this way it is possible to also access files in the plotdata (pd) format by simply changing the variable name. On the implementation side AthletOutput communicates with dynamically generated instances of the specialised backend classes PdFile and H5File, which encapsulate the data retrieval details of their respective storage formats and present the same API to the user-facing class. This approach simplifies the application and adds to the maintainability of the code. PdFile internally extracts geometrical information from the gr-file whereas these data are directly available in the HDF5 output. Another new Batchplot class called "Restarts" implements the same interface as AthletOutput and combines an arbitrary

number of restart files into one virtual dataset by reading and concatenating respective sections on demand. No additional files are generated in this process, which could be prohibitively expensive in terms of both storage and time for very large models.

Since a lot of plots for the evaluation of ATHLET's simulation results follow repetitive patterns, it was decided to collect them in parametrizable Batchplot functions for the standardized depiction of temporal and spatial variables in thermal-fluid (TFO) and heat conducting (HCO) objects.

The function "plotTemporalEvolution" (Fig. 5.2) plots the temporal behaviour in one or more control volumes or junctions of a TFO or HCO. All curves are individually labelled in a user configurable way for the identification in the legend. Further optional parameters enable the user to adjust the physical units on both coordinate axes. The user can choose between a step function representation or linear connections between the individual data points.

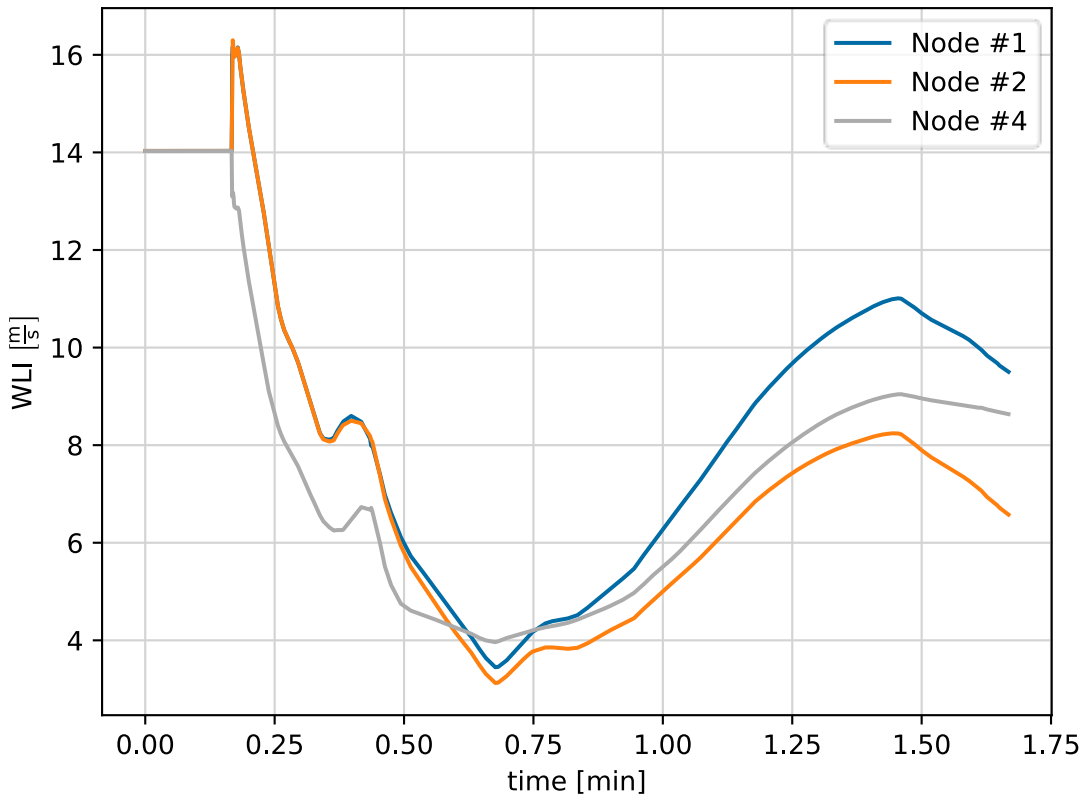

Fig. 5.2 Sample output of the function plotTemporalEvolution()

Several functions are provided for spatial distributions on TFOs and HCOs. They offer an additional stairs representation, which consists of parallel lines constant over each control volume. Parameters for selecting the physical units are also provided.

Using "plotAxialDistribution" (Fig. 5.3) the user can display a variable over the calculation nodes of TFOs and HCOs parallel to the (axial) flow direction at one or more simulation times. The data of several TFOs can be concatenated. However, it is assumed that the objects are connected at their ends, and no effort is made to verify this condition. Optionally, the grid generated by the control volumes is drawn. Analogously, the object boundaries can be depicted, and the object names be placed at the respective start nodes. If an object's order of nodes set by the output data does not fit the spatial orientation of its neighbours, the function allows to reverse it. As vertical pipes are prevalent in reactors plotAxialDistribution provides a setting for exchanging the coordinate axes and determining the orientation of the spatial one. For TFOs equipped with a mixture level model, the associated value will be automatically depicted by splitting the relevant control volume at the mixture level elevation and adding the data point above the level. This functionality is still at the test stage. The same holds for the support of SAFT objects, which can only be used in combination with pd files so far.

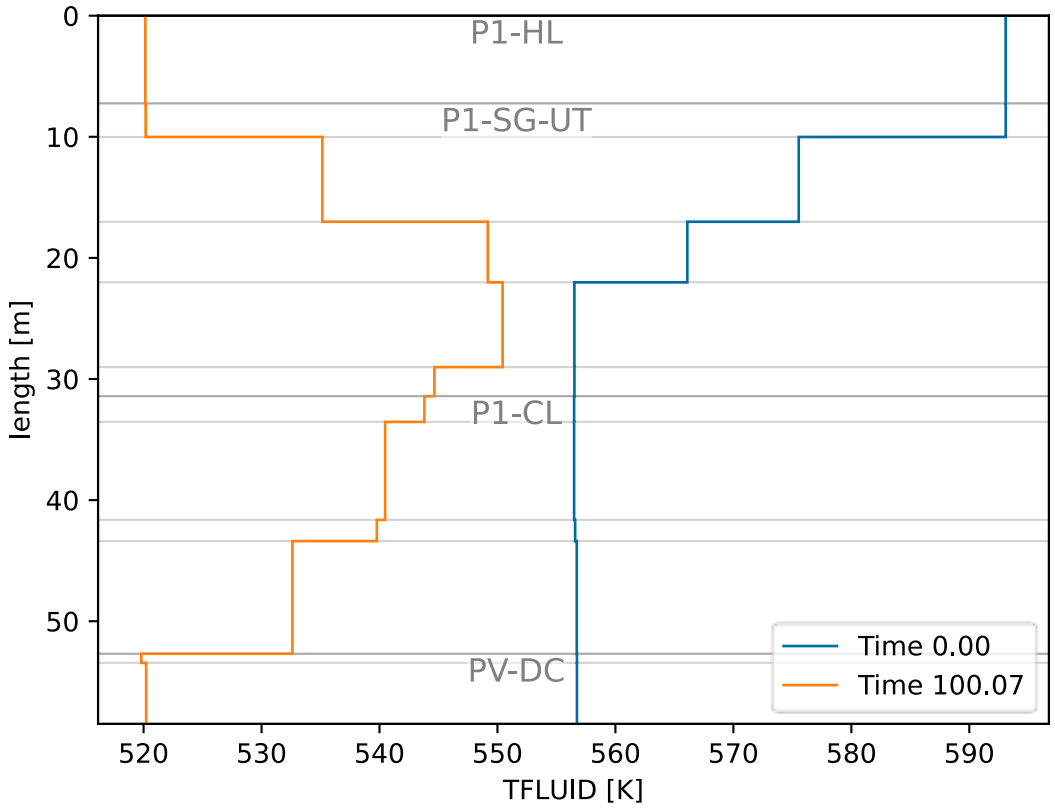

Fig. 5.3 Sample output of the function plotAxialDistribution(). The abscissa axis has been aligned vertically facing downward using the setting `orientation="verticalDown"`

For displaying radial variables over the material zones and layers of a HCV the function "plotRadialDistribution" (Fig. 5.4) was designed. A peculiarity of this plot is the option to incorporate temporal variations of the gap widths between the zones due to thermal effects instead of displaying the (constant) cold geometry. For this reason, the function is restricted to a single pair of time and axial position. Zone and layer grids are both configurable. A user-definable tolerance value for the gap width determines if a gap is considered closed, in which case the discontinuity of distribution at this place is removed when the stairs representation is employed, whereas the linear representation is always continuous.

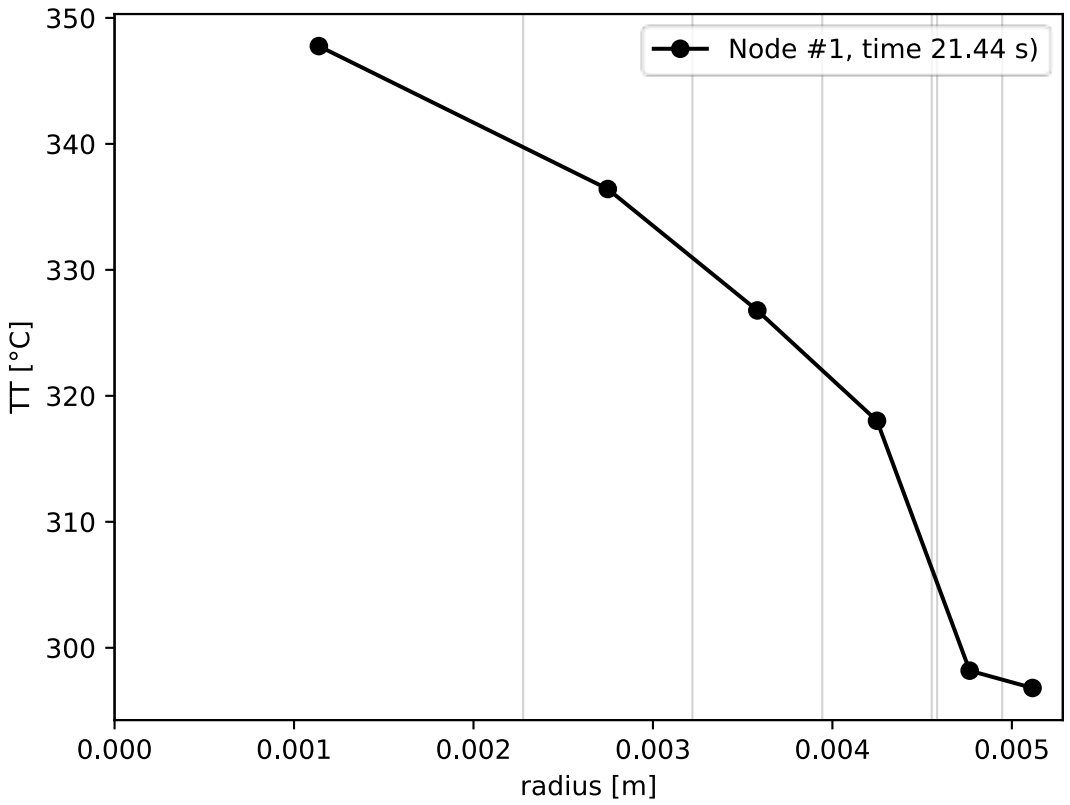

Fig. 5.4 Sample output of the function plotRadialDistribution(). The auxiliary line between the data points is not interrupted by the gap between two zones when the value “plot” is used for the parameter “plotFun”

The variant "plotRadialTemperature" (Fig. 5.5) for HCV layer temperature distributions offers the option to include the HCV surface temperatures into the graph. In addition, the temperatures of potential neighbouring fluid volumes are indicated using inwards-oriented arrows at the inner and outer layer boundaries.

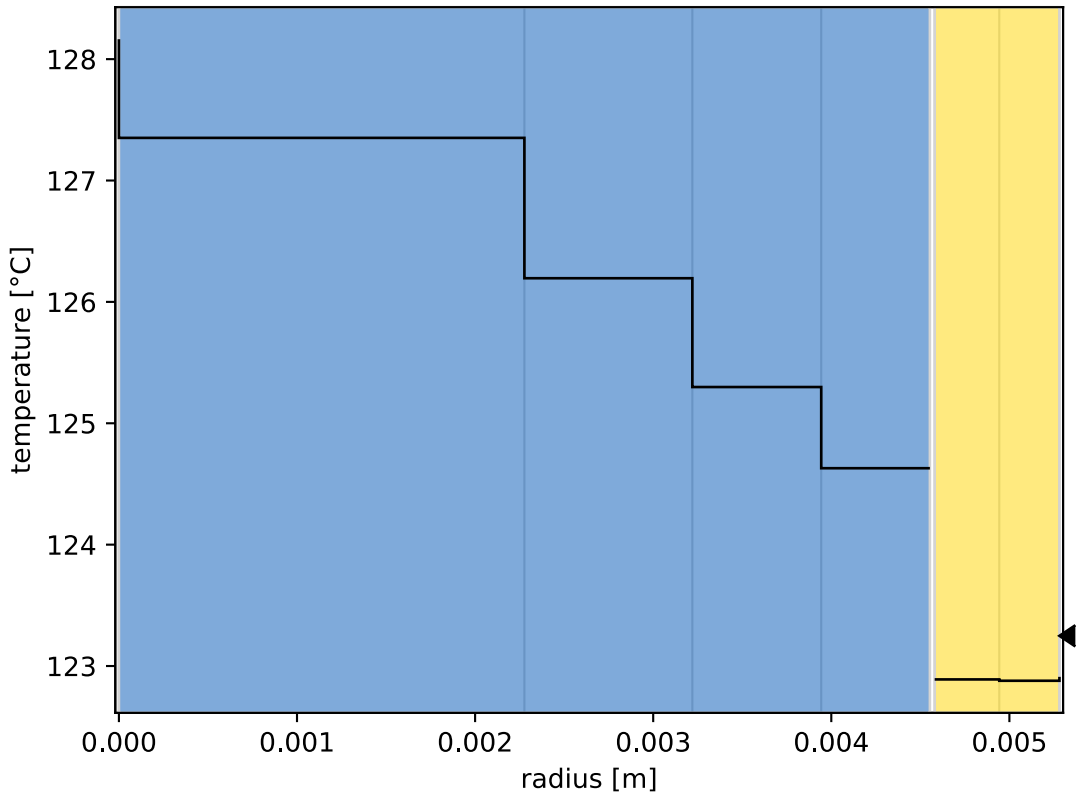

Fig. 5.5 Sample output of the function plotRadialTemperature. On the right-hand side, the arrow indicates the value of the HCV-adjacent fluid temperature.

In order to also make colour-coded visualisations of simulation results based on AIG-2 templates scriptable, Batchplot has been extended by the function "plotObjects" (Fig. 5.6) which reads an AIG-2-generated SVG file, identifies the included TFOs and HCOs and colours their control volumes according to the data at the selected time. Mixture level data present in TFOs are automatically overlayed although the present solution works only for mixture level models which span the whole length of the corresponding TFOs, since more detailed information is missing in the output files currently.

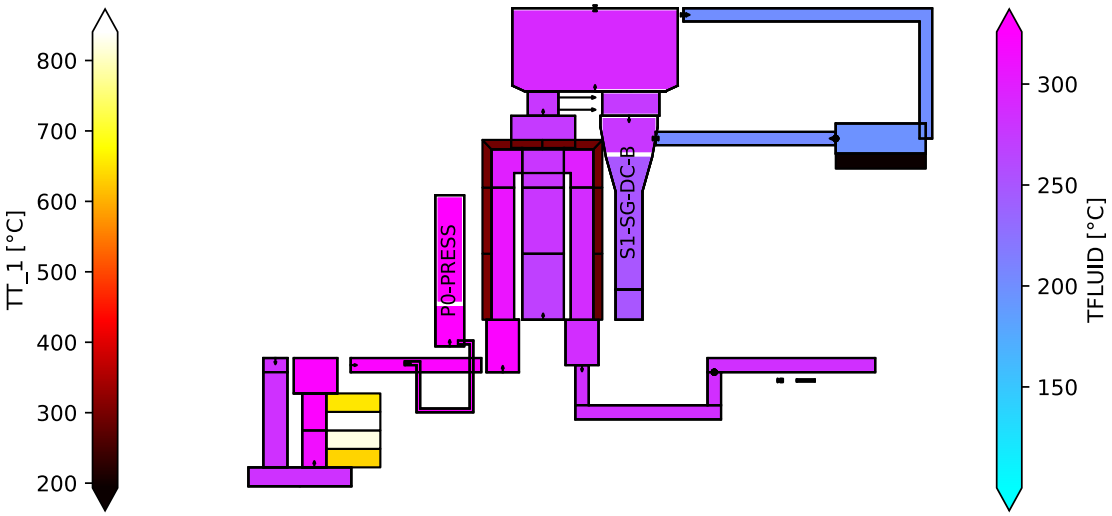

Fig. 5.6 Sample output of the function plotObjects(). The TFOs containing mixture levels are labelled, the level position is indicated using a white horizontal bar.

5.4.2 3D Visualization with ParaView

Profiting from Batchplot's data structures for accessing simulation results, the experimental and still in-house tool aiming at the preparation of ATHLET plot data for 3D-visualisation in ParaView (dating back to project RS1199 from 2015 /SCH 15/) was thoroughly revised. The code was simplified and modularised so that, e.g., the potential introduction of a new 3D output format in place of EXODUS-II becomes feasible.

The generation of the geometry and the assignment of simulation data to the geometry take place in the same program now. The user can restrict the converted time interval, which is especially useful for excluding ATHLET's zero-transient calculation results. Time-invariant geometrical values are efficiently stored in static attributes of the EXODUS-II model instead of using time dependent variables. In the same vein the use of data compression solves the storage problem, which arises from the fact that EXODUS requires a distinct variable value for every cell (triangle, tetrahedron), even though the values for the numerous cells of a control volume's 3D representation are the same. The previous version of the program stored the variable data non-redundantly in non-cell related structures and relied on a ParaView programmable filter for data multiplication. The viability of this approach was hampered by slow execution and the instability of ParaView’s Python API, resulting in an externally driven maintenance burden.

Finally, the installation of the converter has been streamlined by providing support for Python's "pip" package manager. By using a Python package for the generation of volume representations of triangle surface models by tetrahedralization it was possible to also eliminate the compilation of the previously used C library from the distribution process and the corresponding Python interface code.

5.4.3 AC²-GUI

The AC² graphical user interface has been extended to support both remote and local utilization of the Numerical Toolkit NuT, which have been introduced with the release of AC² 2025 /STE 25/. Consequently, ATHLET and COCOSYS can now be launched not only via NuT Remote but also through NuT Local, providing users with greater flexibility in how simulations are started. In addition, the options for FENNECS have been enhanced, offering additional options for defining simulation parameters.

5.4.4 ATHLET Input Graphics

Following users' request for better support of the work with ATHLET on the Linux operating system, the ATHLET Input Graphics (AIG-2) was slightly adapted and can now be distributed also in a Linux version.

With the introduction of horizontal coupling for plate HCOs in ATHLET (see 4.1), AIG-2 had to be extended as well, because the standard logic to display HCOs, which were so far always aligned along the axis of a TFO, does not yield a satisfying result for horizontal plates. Thus, they are treated independently in the routines computing the display coordinates. Bypassing most of the code for standard HCOs, each horizontal plate HCO is drawn explicitly as a tetragon, with only two points over its length. No subdivision is necessary because a horizontal plate consists always of just 1 HCV.

With this extension, horizontal plate HCOs can now reasonably be displayed in AIG-2, as demonstrated in Fig. 5.7 for some arbitrary objects (names of horizontal plate HCOs ending in -HOR). Also, after export to the APG format, the values of variables in a plate HCO can be visualized in ATLAS, just like for any other HCO or TFO.

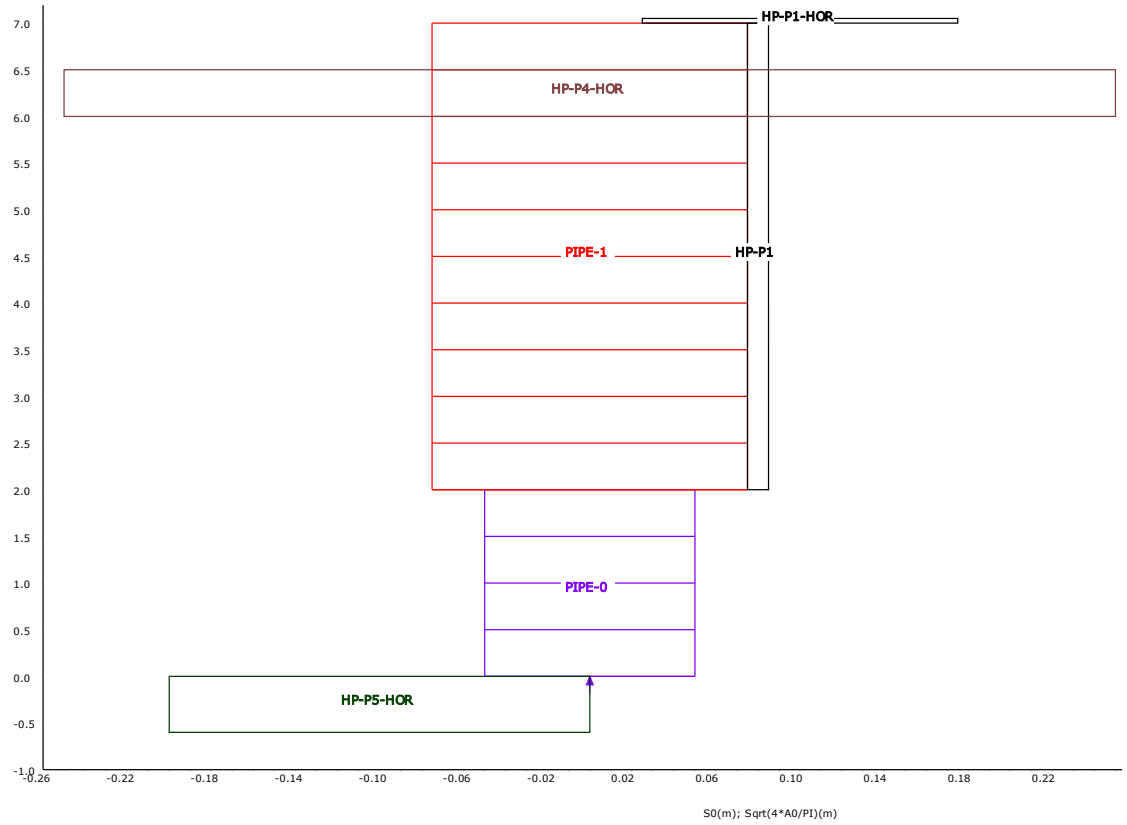

Fig. 5.7 Representation of horizontal plate HCOs in AIG-2

5.4.5 GCSM Input Graphics

The possible output formats for the graphical representation of GCSM signals are changed. The vector format CGM (Computer Graphics Metafile) has been superseded by more modern vector formats, and it cannot be directly included anymore in Microsoft Word documents. Therefore, CGM export was removed, and SVG (Scalable Vector Graphics) export was implemented. Furthermore, in addition to BMP (bitmap) as a raster graphics format, the possibility to save the graphics in the PNG (Portable Network Graphics) format was added to GIG.

5.4.6 ATHLET Developer Tools

To support program development, several tools were developed in the past aiming at easier and faster debugging in case of obvious program errors. One of these tools, which can be invoked via the input data under CW `INTEGRAT` / PW `DEBUG`, enables the monitoring of the increments of one selected solution variable for every time step. All contributions (time derivative, partial time derivative, Jacobian matrix) are listed for further

investigation. However, in the former implementation the reported time increment could be erroneous, which has been corrected now.

6 Program Improvements after User Feedback

6.1 Pressure Loss in Pipe Bundle Cross Flow

To improve the modelling of cross flow through pipe bundles, e.g. in the core, and considering the form loss dependence on the Reynolds number, suitable correlations were incorporated into the code using the possibilities created by the introduction of CW `FORMLOSS`. In their implemented form, following the formulas given in /VDI 13/, the correlations are valid for isothermal flow (that is, without any corrections due to the change of the fluid properties with temperature) and for pipe bundles in staggered or aligned arrangements (Fig. 6.1) over a wide Reynolds number range. For the staggered case, the correlations also distinguish between cases with the narrowest cross section perpendicular to the flow, and the narrowest cross section in the diagonal.

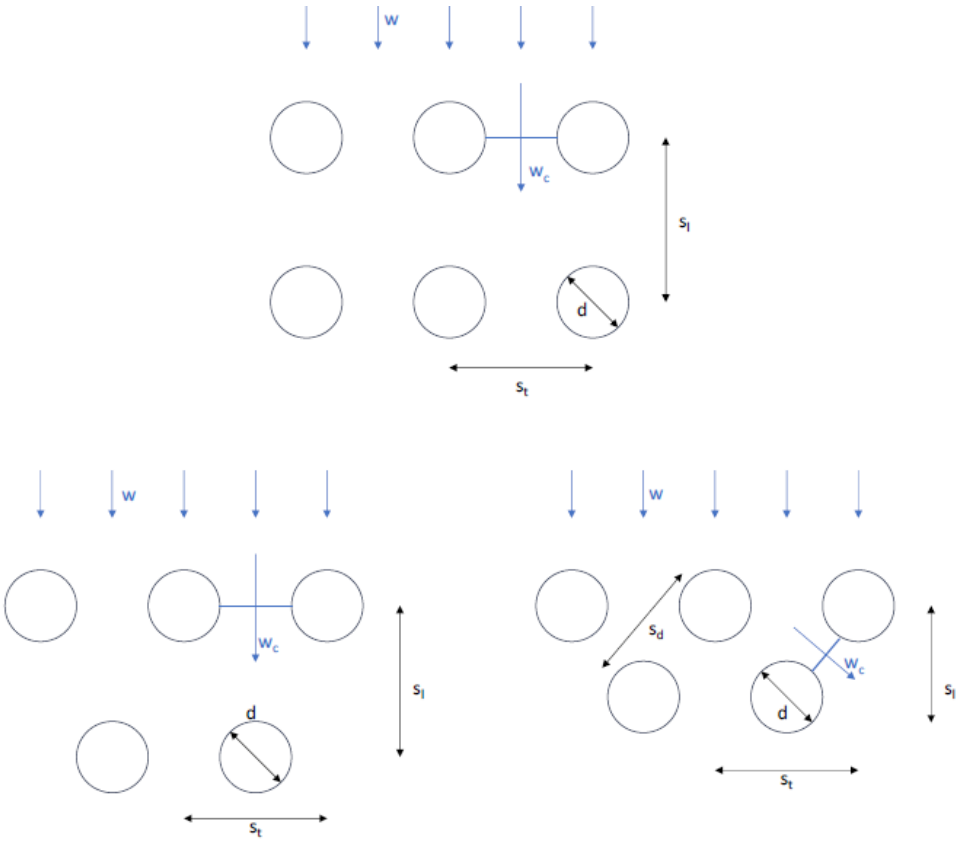

Fig. 6.1 Schematical representation of the considered bundle configurations. Top: In-line arrangement of pipes. Bottom; staggered arrangement of pipes with the narrowest cross section either perpendicular to the main flow direction (left) or in the diagonal (right)

The following pictures show the resulting contribution of each line of pipes to the form loss for in-line (Fig. 6.2) and staggered (Fig. 6.3) arrangement for different values of the geometry parameters

$$a = \frac{s_t}{d}\,, b = \frac{s_l}{d}$$

where s_t and s_l are the transversal resp. the longitudinal distance between the pipe centres (see Fig. 6.1).

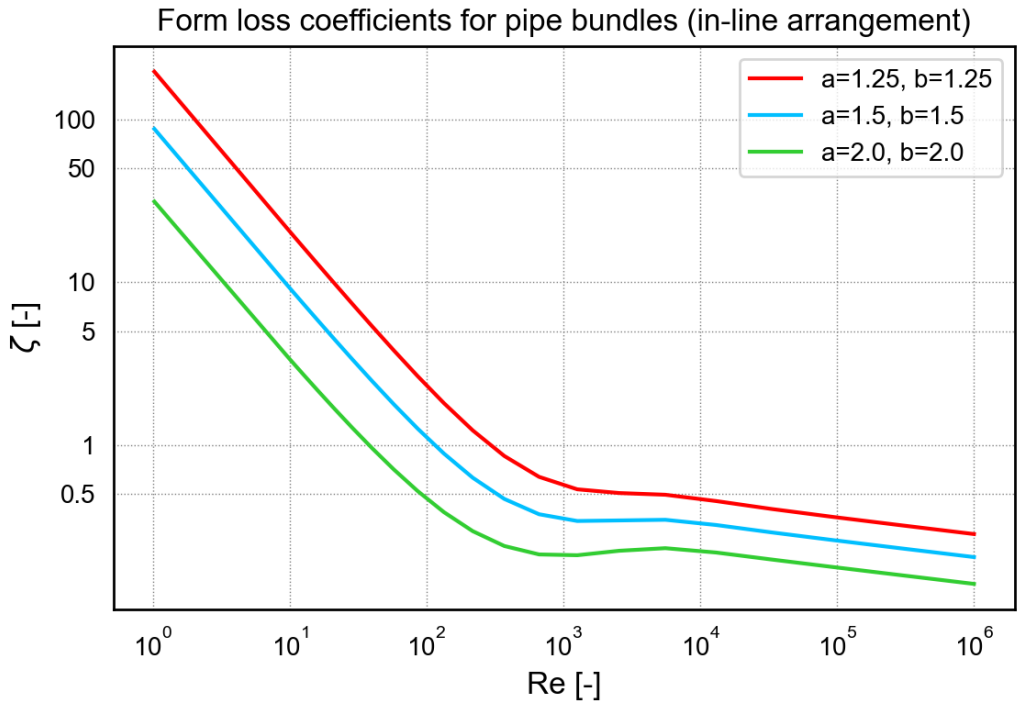

Fig. 6.2 Contribution of each line of pipes to the form loss coefficient for a pipe bundle in in-line arrangement

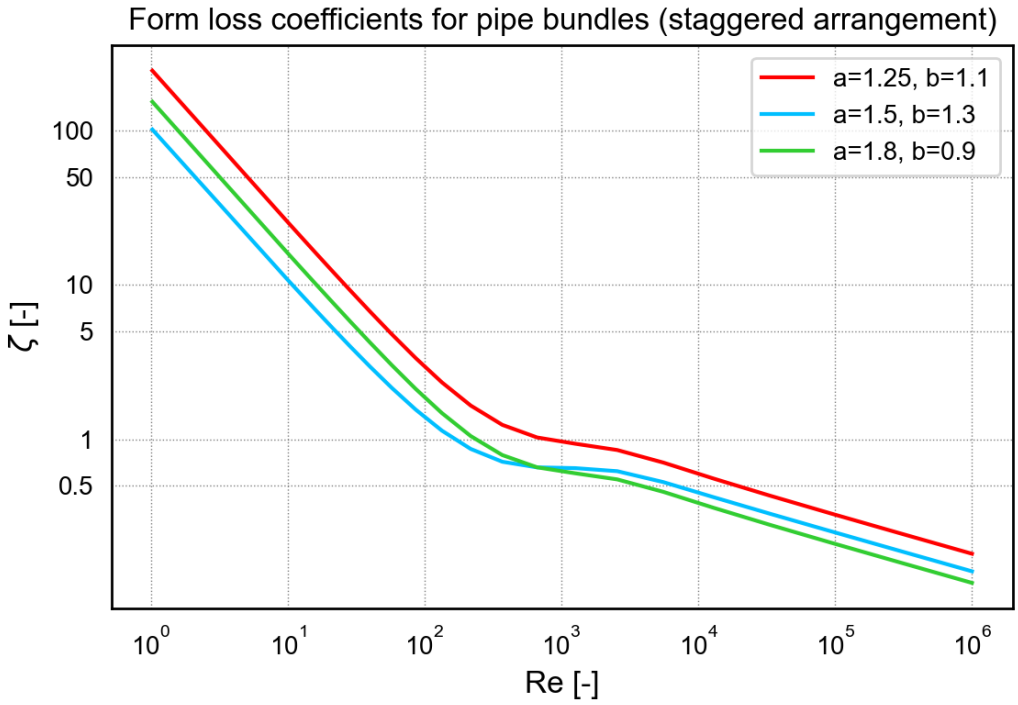

Fig. 6.3 Contribution of each line of pipes to the form loss coefficient for a pipe bundle in staggered arrangement

The implemented correlations are valid for a wide range of the bundle Reynolds number (i.e. based on the velocity in the narrowest cross section and the pipe diameter) up to a critical bundle Reynolds number where a local minimum of the form loss coefficients has been found in the experiments. The transition to supercritical regime taking place here is not considered in ATHLET, resulting in slightly underestimated form loss coefficient for very high bundle Reynolds numbers.

6.2 Automatic Nodalization of HCO

In ATHLET, the nodalization of the HCOs is automatically derived on the basis of the user-provided nodalization of the coupled TFO(s). The nodalization is done in such a way that matching grids are generated. Calculation on SMR with helical heat exchanger has shown an issue with the automatic nodalization of HCOs, based on the nodalization of the connected TFOs (on both inner and outer side). The error in the nodalization occurred under certain conditions: Inner and outer TFO were not congruent (which is typical for e.g. helical heat exchangers), and the outer TFO was defined with different orientation (as illustrated by the darts in Fig. 6.4) than the HCO.

In Fig. 6.4, the SMR configuration with inclined TFO “SG1TUBE” representing the helical coil, vertical pipe “PDT” representing the downcomer the heat exchanger is inserted in, and the HCO “HSG1” (in red), which represents the wall of the helically shaped heat exchanger pipe. From the figure it can be seen that erroneous nodes had been introduced in the lower part of the HCO, eventually resulting in a code failure.

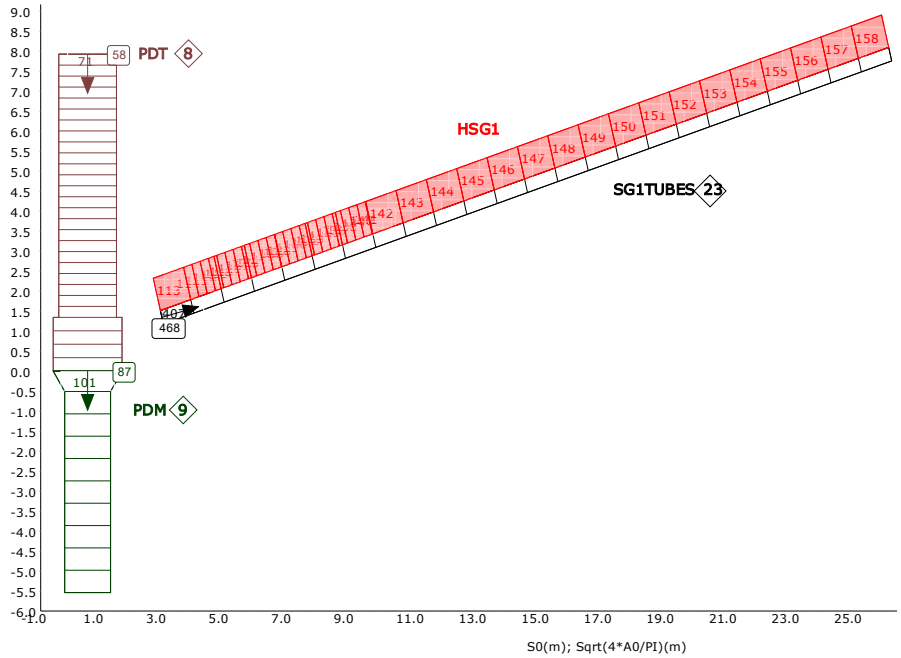

Fig. 6.4 Erroneous nodalization of HCO HSG1 with non-matching grids in lower pipe section

Having improved the implementation of the HCO nodalization, the correct HCO grid could be achieved (see Fig. 6.5). This code improvement enhances the code’s user friendliness with regard to the modelling of heat exchangers with a complex geometry, as they are used in passive systems (such as. helical heat exchangers or emergency condensers).

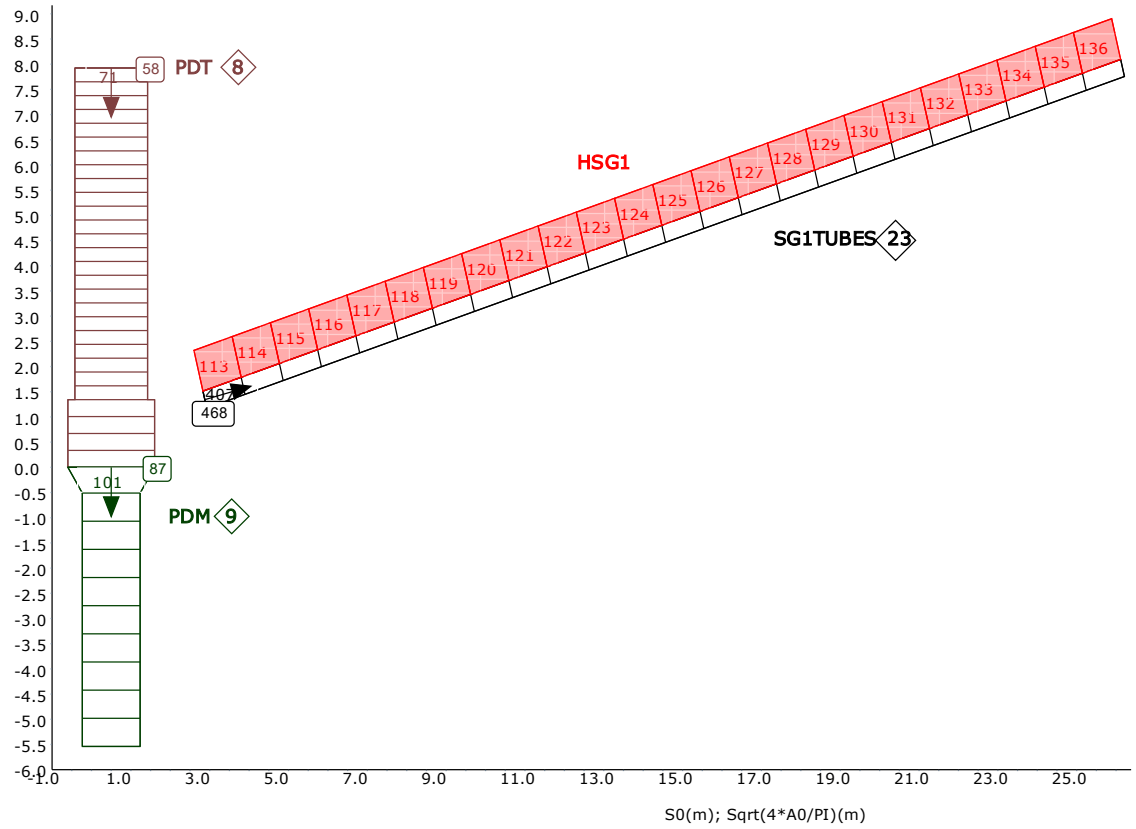

Fig. 6.5 Correct nodalization of HCO HSG1 resulting in completely matching grids on both sides of HCO

6.3 Laminar-turbulent Transition Friction Factor Calculation

Concerning the calculation of wall friction, ATHLET's approach has been to determine the Darcy-Weisbach friction factor as the maximum of the friction factor for laminar flow (acc. to Hagen-Poiseuille) and the friction factor for turbulent flow (acc. to Colebrook):

$$\lambda_L = \max\left(\lambda_{\mathrm{lam},L}, \lambda_{\mathrm{turb},L}\right) \tag{6.1}$$

Herein, the lower limit for the Reynolds number has been set to 500.

Now, the implementation has been revised considering following two key aspects. On the one hand, the lower Reynolds number has been moved to 5:

$$Re_L = \max\left(\frac{|G| \cdot D_H}{A \cdot \mu_L}, 5\right) \tag{6.2}$$

And on the other hand, the transition between laminar and turbulent friction factor is calculated via a cosine interpolation

$$\lambda_L = \begin{cases} \lambda_{\mathrm{lam},L} & \text{for } \mathrm{Re}_L \le \mathrm{Re}_{\min} \\ \lambda_{\mathrm{lam},L} + \dfrac{\lambda_{\mathrm{turb},L} - \lambda_{\mathrm{lam},L}}{2}\left(1 - \cos\left(\pi\left(\dfrac{\mathrm{Re}_L - \mathrm{Re}_{\min}}{\mathrm{Re}_{\min} - \mathrm{Re}_{\max}}\right)\right)\right) & \text{for } \mathrm{Re}_{\min} \le \mathrm{Re}_L \le \mathrm{Re}_{\max} \\ \lambda_{\mathrm{turb},L} & \text{for } Re_{\max} \le \mathrm{Re}_L \end{cases} \quad (6.3)$$

with $\mathrm{Re}_{\min}$ and $\mathrm{Re}_{\max}$ as interpolation boundaries. Both can be altered by user input. Default values are $\mathrm{Re}_{\min} = 2300$ and $\mathrm{Re}_{\max} = 4000$. The modified approach is used automatically for pipe and annulus geometry. For bundle geometry, it can be optionally activated through input data settings.

The new approach enables a more accurate prediction of the wall friction in laminar and laminar-to-turbulent transition region, which is of particular interest e.g. for the simulation of passive systems at start-up. The described code modification is based on an original implementation developed by IKE Stuttgart /ABD 25/. In order to generally employ the wall friction model and distribute it to all users, the implementation has been revised, quality-assured, integrated with other ATHLET code options and finally validated.

6.4 Improved Condensation Model

In the frame of a LSTF LB-LOCA post-test calculation, extremely superheated liquid conditions were calculated by ATHLET, which finally resulted in a program stop. The detailed investigation of the simulation revealed the bulk condensation model as source for the steep temperature increase leading to the program stop.

The bulk condensation model becomes active in case of (even small) liquid subcooling. In this case, a relatively high condensation rate (based on the calculated HTC and interfacial area) combined with a very small liquid mass fraction in the CV resulted in the observed strong liquid superheat, since the condensation of saturated vapor is accompanied by an energy flow heating up the liquid phase, here above saturation temperature.

In order to avoid the unphysical behavior with liquid superheating due to vapor condensation, the bulk condensation γ rate at high void fraction and low liquid subcooling has been limited. The limitation for a time step size Δt considers the existing liquid subcooling

in terms of the liquid enthalpy H_l as well as the amount of available liquid mass m_l in the CV:

$$(H_l - H')\, m_l \;\leq \gamma_{\max} \cdot \Delta t \cdot (H_v - H') \tag{6.4}$$

This yields as lower limit for the (negative) condensation rate:

$$\gamma_{\max} \geq \frac{(H_l - H')\, m_l}{(H_v - H')\, \Delta t} \tag{6.5}$$

If the CV under consideration is connected to a feed line for, e.g., emergency coolant injection, for which specific condensation models at the spray or jet surface can be activated (CW `INJECTION`), the subcooling of the injected liquid G_{inj} is taken into account when estimating the maximum condensation rate.

$$(H_l - H')\, m_l + G_{\text{inj}} \cdot \left(H_{\text{inj}} - H'\right) \leq \gamma_{\max} \cdot\; \Delta t \cdot (H_v - H') \tag{6.6}$$

For the spray injection device, the extended implementation was successfully verified using condensation tests (STRA23 and STRA29) from the DHVA (Druckhalterversuchsanlage) facility in Zittau /WEB 93/. To this end, an existing dataset /CRO 12/, which had originally been created for ATHLET version 2.2, was updated and eventually integrated into the ATHLET CI.

6.5 Corrected Pressure Iteration

If a priority chain representing a closed loop (usually the first PC of a TFD system) with stagnant fluid is modelled, which cannot reach a true steady state, e.g. because there is a running pump or heat addition in the loop, it is expected that the user-provided pressure in the first CV of that PC is kept constant throughout the SSC and that a pressure jump may occur from the last to the first CV. However, the expected behavior could only be observed if the closed loop with the stagnant system is the very first PC of the whole data set. For all subsequent PCs forming closed loops with stagnant fluid, the pressure in their respective first CVs could be overwritten during the SSC. The SSC has been corrected to achieve the expected code behavior.

6.6 Extended Plugin Interfaces

The concept behind plugins aims to give users the opportunity to apply ATHLET more individually by developing specific features on their own and coupling them to the related plugin interface provided in the ATHLET release versions. Various interfaces, which have been extended in their scope of application recently, are accessible in ATHLET, e.g. for the coupling of user-provided HTC or XL correlations.

The following enhancements have been implemented and made available to users:

- A new interface has been introduced for HTC correlations predicting the convective heat transfer to vapor in (dispersed flow) film boiling heat transfer mode.
- The possibility to access ATHLET module variables through plugins in an OMP-safe way has been prepared and illustrated in an example plugin. The extension enables plugins to make use of module variables in both serial as well as parallelized calculations.
- The MASL (Minimaler Abstand zur Siedeübergangsleistung, minimum critical power ratio) plugin interface for coupling of proprietary XL correlations has been extended to recent needs of such correlations.

6.7 Friction Loss Calculation for Helical Coil Heat Exchanger

For junctions that belong to a TFO that is coupled to a helically coiled heat exchanger HCO, dedicated flow loss correlations are applied to calculate the pressure drop. The constant curvature of the pipe results in higher pressure losses compared to straight pipes. Furthermore, the pressure drop due to the flow around the outside of the helical pipes is considered. The model presented hereafter is a first approach based on the work by Krieger /KRI 24/ to consider the specific phenomena of heat transfer and pressure drop in a helically coiled heat exchanger. Further validation is needed in future.

For the inner side of the curved pipe, the friction factor can be calculated according to Ito /ITO 59/:

$$\lambda_c = \lambda_{\text{turb}} \left(\text{Re} \left(\frac{d_h}{d_c} \right)^2 \right)^{1/20} \tag{6.7}$$

λ_{turb} describes the turbulent friction factor for a straight pipe and is calculated based on the default ATHLET approach for the turbulent region, i.e. the Colebrook equation. The second factor corresponds to the Dean Number, which is used equivalent to the Reynolds number for helical pipes. Here, d_c is the diameter of the coil (i.e. the steam generator).

For the two-phase region, the pressure drop calculation is based on the Martinelli-Nelson model. For the liquid-only $\Phi_{tt,L}$ and vapor-only loss coefficients, the approach presented in /NAR 82/ is used:

$$\Phi_{tt,L} = \frac{\Phi_{tt,V}}{X_{tt}^{0.875}} \tag{6.8}$$

$$\Phi^2{}_{tt,V} = 0.895 + (X_{tt} + 0.076)^{0.875} + 1.21 \cdot 10^{(-0.334(\log X_{tt} + 0.668)^2} \tag{6.9}$$

For the flow on the outside of the curved heat exchanger pipes, the pressure drop is calculated as described in chap. 6.1 for pipe bundle crossflow.

6.8 Simulation of Reynolds Number-Dependent Form Losses

The implementation of the support for Reynolds number dependent form losses was slightly changed to allow the definition of an arbitrary number of form loss keywords under CW `FORMLOSS`. Now, a limit of 999 form loss keywords applies. All arrays are allocated based on the actual number of form loss keywords defined in the input deck. The number of form loss keywords that can be assigned to one junction was increased as well, from three to 32. The chosen value is arbitrary, and certainly large enough for any reasonable application of this feature. As before, only one form loss keyword can be assigned to a junction within a cross-connection object.

Because of an error in the implementation, it could happen – under certain circumstances, dependent on the order of the definition of form loss keywords in the input deck – that ATHLET tried to access a wrong or a non-existing table to interpolate the form loss value causing wrong results. After this bug had been discovered due to a report by an external user, a fix was prepared which has been included in the patch version 3.5.1 of ATHLET (see chap. 8.5).

6.9 Solved Code Errors

The implementation of ATHLET is continuously improved and observed code errors could be fixed:

- For the simulation of research reactors with narrow rectangular coolant channels, the Sudo-Kaminaga CHF correlation /SUD 93/ is implemented in ATHLET and is recommended. Optionally, and not limited to research reactors, the user can provide an own CHF correlation that is coupled with ATHLET through a plugin interface. To both approaches several corrections have been applied.

  a) The identification of upflow/downflow condition has been refined to consider unusual orientations of TFO and HCO.

  b) Sudo-Kaminaga implementation has been made more flexible, so that CHF calculation can be performed on both inner and outer sides of a HCO.

  c) Possible inconsistencies in Jacobian matrix calculation for the integral variant of the Sudo-Kaminaga correlation have been fixed.

  d) The calculation of the total heated area that is used as a parameter in the Sudo-Kaminaga correlation has been corrected.

- The valve model was corrected to avoid an access violation: The error was observed, when a valve was defined in a junction that eventually was not integrated (e.g. in case of coupling of two pipes within one common priority chain, so that only one of the coupled boundary junctions was integrated).

- An error in the table interpolation procedure used to calculate critical flow rates with the Moody model for critical discharge rate calculation has been fixed. Additionally, restart capability has been implemented for the Moody model.

- The ATHLET key file, which is used for post-processing e.g. with ATLAS, has been improved. As reported by HZDR, the former output format of the key file was not compatible with very huge systems. After modifying the output format, the key file could be successfully employed also for huge system configurations together with various post-processing tools.

- Several floating-point errors that had been triggered in rare cases in diverse parts of the code (e.g. for liquid density being less or only a bit larger than gas phase density) have been prevented.

- In ATHLET, the TDV can be used to apply a pressure boundary condition at the end of a flow path. If several flow paths were connected to the same TDV, they could interfere through a momentum flux calculation across the TDV. This undesired behavior has been removed.

- The McEligot HTC correlation is the ATHLET default for convection heat transfer to vapor calculation. Now, McEligot has also been activated for the inner tube side of helically coiled heat exchangers under film boiling conditions to avoid a program stop if CHF is exceeded.

- The implementation of the Shah correlation used multiplication instead of exponentiation for a model parameter, this was corrected for version 3.5.1.

- Concerning the Liu-Winterton correlation for nucleate boiling heat transfer, the boiling enhancement factor was only applied for saturated boiling conditions so far. The factor has now been applied for subcooled boiling conditions as well. Furthermore, the implementation of the correlation has been slightly modified in order to avoid potential discontinuities in the transition from subcooled to saturated boiling.

- Mass balance output under `FLUIDBAL` for coupled calculations with COCOSYS/CFD corrected. Mass flows into/out of an external coupling branch (`ICOPLO`>0) are added either to `LEAKMASS`, if coupled junction is discharge or coupling branch is not a TDV, or to `TDVMASS`, if coupling branch is TDV.

- In tests with debug versions and with Valgrind /VAL 26/, several instances were found where access violations to arrays could be triggered or where uninitialized variables were used in rare cases. The code was corrected accordingly.

7 International Cooperation

7.1 OECD/NEA RBHT-II Project

As a part of ATHLET development and validation, GRS participates in phase two of the OECD/NEA RBHT Project. Results from the first phase of the project have already been used in ATHLET validation and model development, see chapters 2.1.3.2 and 3.1.2. The RBHT Project features a series of reflooding tests, used in an open and blind phase as a benchmark for thermal-hydraulics system and subchannel codes with participants from ten nations. Phase two of the project focuses on low flooding rates, which proved difficult to capture for many simulation codes in phase one. Information on the test section has previously been provided in chapter 2.1.3.2.This phase of the project began in 2024 and is planned to be completed by late 2026. Workshops are held regularly, where results are presented by the participants, with the opportunity to discuss with the experimenters. GRS presented current simulation results at three occasions /DÜN 25a/, /DÜN 25b/, /DÜN 26/.

7.1.1 Test Parameters

Compared to phase one of the project, RBHT Phase II focuses on low flooding rates and also varies between three different pressure levels. The maximum reflooding rate is 2 cm/s and the lowest rate is 0.5 cm/s, pressures range from 1.38 bar to 4.13 bar. Two of the blind tests use a variable reflooding rate, which starts at 2 cm/s for the first 30 seconds of the tests and is then reduced to 1 cm/s. The heating power of the bundle lies between 25.3 kW and 144 kW depending on the test and reflooding starts, when the peak bundle temperature reaches a value between 922 K and 1000 K. Inlet subcooling is between 5 K and 20 K. The boundary conditions for the different open and blind tests are listed in Tab. 7.1. The numbering of the tests continues the pattern from phase one.

Tab. 7.1 Parameters of the RBHT Phase 2 open and blind tests

Test ID	Flooding rate [cm/s]	Inlet sub-cooling [K]	Pressure [kPa]	Bundle power [kW]	Peak init. temp. [K]
O-17	2	5	276	144	1000
O-18	2	20	276	144	1000
O-19	2	5	138	144	1000
O-20	2	5	276	144	1000

Test ID	Flooding rate [cm/s]	Inlet sub-cooling [K]	Pressure [kPa]	Bundle power [kW]	Peak init. temp. [K]
O-21	1	5	276	82.4	950
O-22	1	20	276	25.3	922
O-23	1	5	138	82.4	950
O-24	0.5	10	276	35	950
O-25	0.5	5	138	25.3	922
O-26	0.5	20	276	35	950
O-27	0.5	5	413	35	950
B-7	0.75	5	276	82.4	950
B-8	0.75	20	276	82.4	950
B-9	1.5	5	138	82.4	950
B-10	1.5	10	276	82.4	950
B-11	2.0 for 0<t<30 1.0 for 30<t	5	276	82.4	950
B-12	2.0 for 0<t<30 0.5 for 30<t	10	276	82.4	950

7.1.2 Simulation Results

In this section, some selected results will be presented to illustrate the effects of recent ATHLET model development. Additionally, scatter plots are used to qualify the results for different figures of merit across all the phase 2 tests. Access to the data is still restricted for people not participating in the project, so the number of graphs included will be limited.

Overall, results mostly agree well with the experimental data. Whereas the tests with low flooding rates produced the most deviation from the experiments in phase 1, the lesson learned and ATHLET developments since then have greatly improved ATHLET's performance in that parameter range. Fig. 7.1 shows the cladding temperature at 2.69 m elevation for test O-22, one of the slower tests. The simulation agrees well with the experiment. Temperature differences are mostly within a few degrees, and the quench occurs only about 20 seconds early.

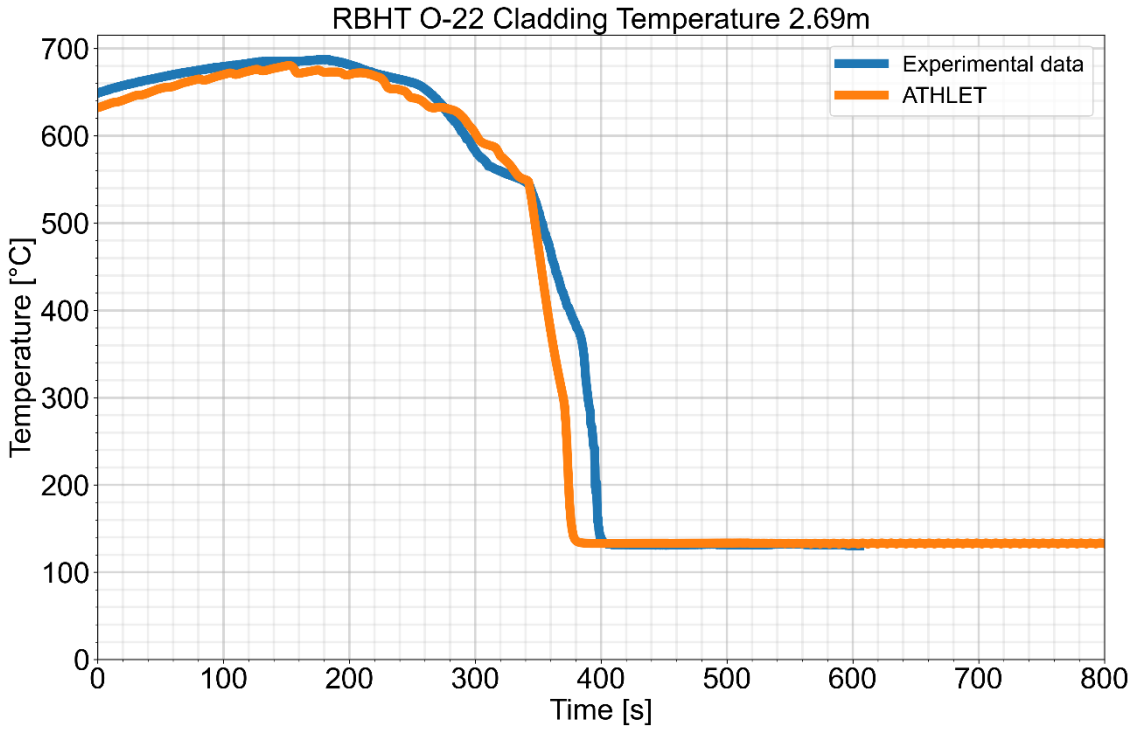

Fig. 7.1 Cladding temperature at 2.69 m for RBHT test O-22

The tests O-19 and B-9 with relatively high flooding rate for the parameter range and low pressure showed the most visible effect when applying the recently developed spacer model. The generally low velocities limit the effect of the model for this particular set of experiments. The thermocouple location at 2.89 m is situated just above a spacer, making it the location where the strongest effect is expected. Whereas simulation results without the spacer model deviate quantitively and qualitatively from the experimental observations, applying the spacer model reduces the peak temperature, accelerates the quenching process and even recreates the early cooling down of the cladding, followed by an additional heat up phase. These temperature trends are shown in Fig. 7.2 and Fig. 7.3. While there is still some deviation, the model greatly improves the simulation results.

Unfortunately, for the thermocouple location 2.69 m, which is far above the nearest upstream spacer, we do not observe similar improvements. While applying the spacer model prolongs the initial heat-up phase which qualitatively agrees better with the experimental data, the temperature increase is too strong, leading to a significant overestimation of the peak temperature, as shown in Fig. 7.4 for test O-19. The effect of the spacer model further away from the spacer locations still has to be further investigated.

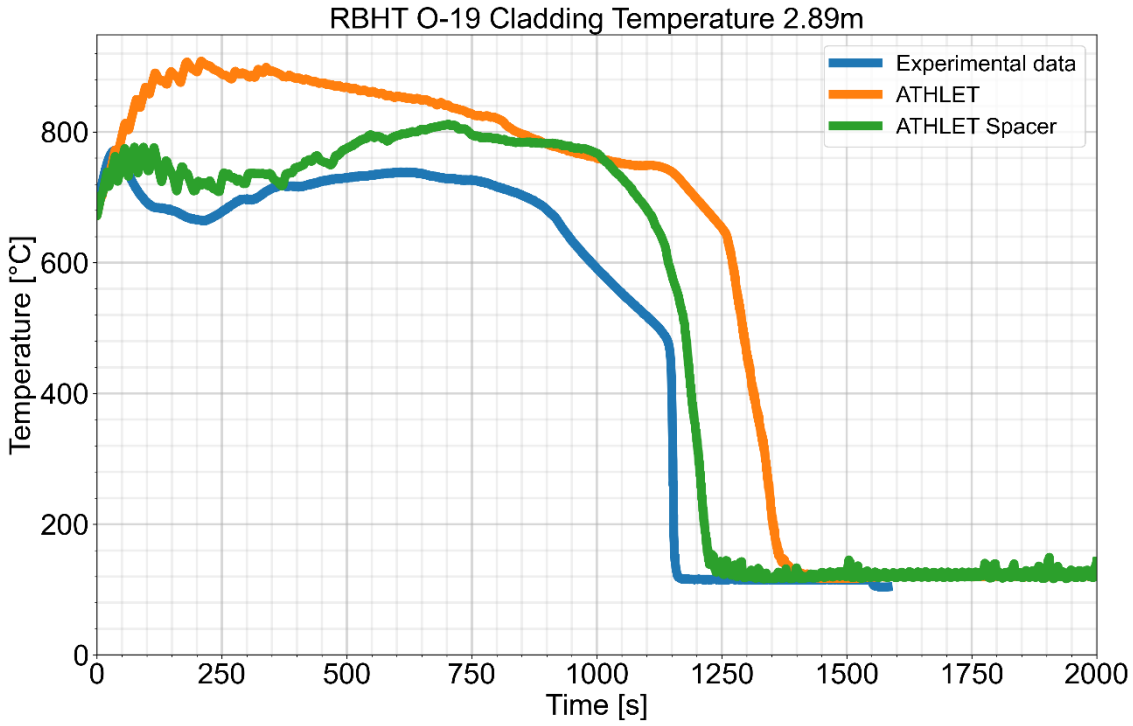

Fig. 7.2 Cladding temperature at 2.89 m for RBHT test O-19

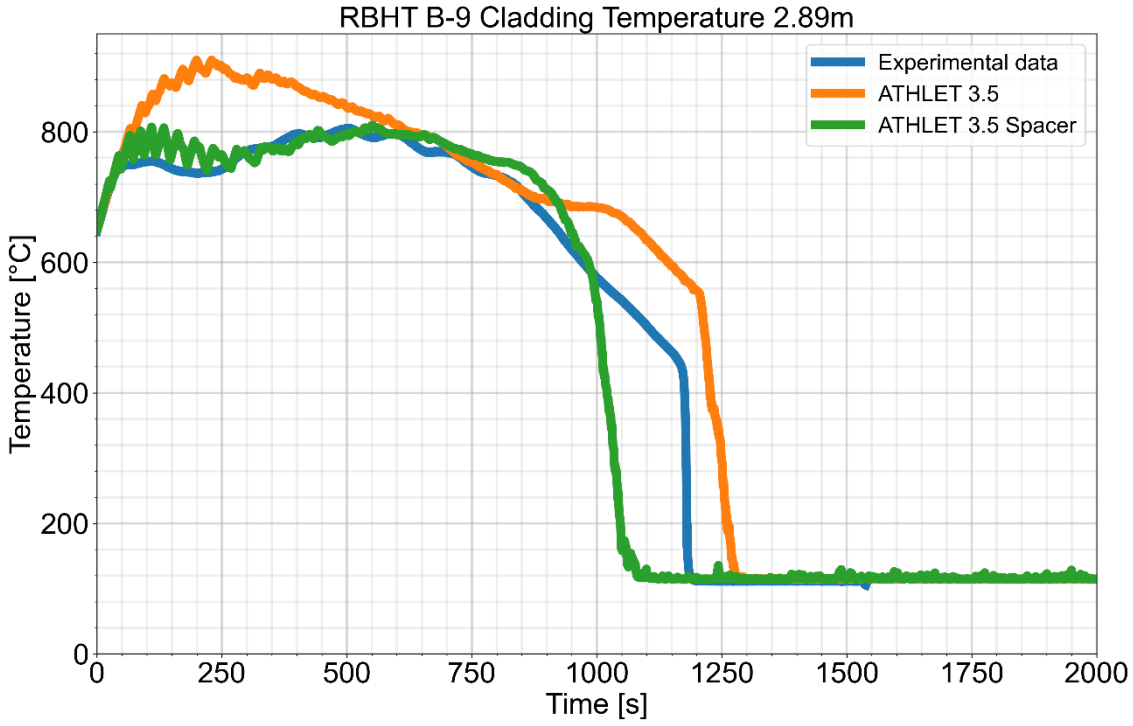

Fig. 7.3 Cladding temperature at 2.89 m for RBHT test B-9

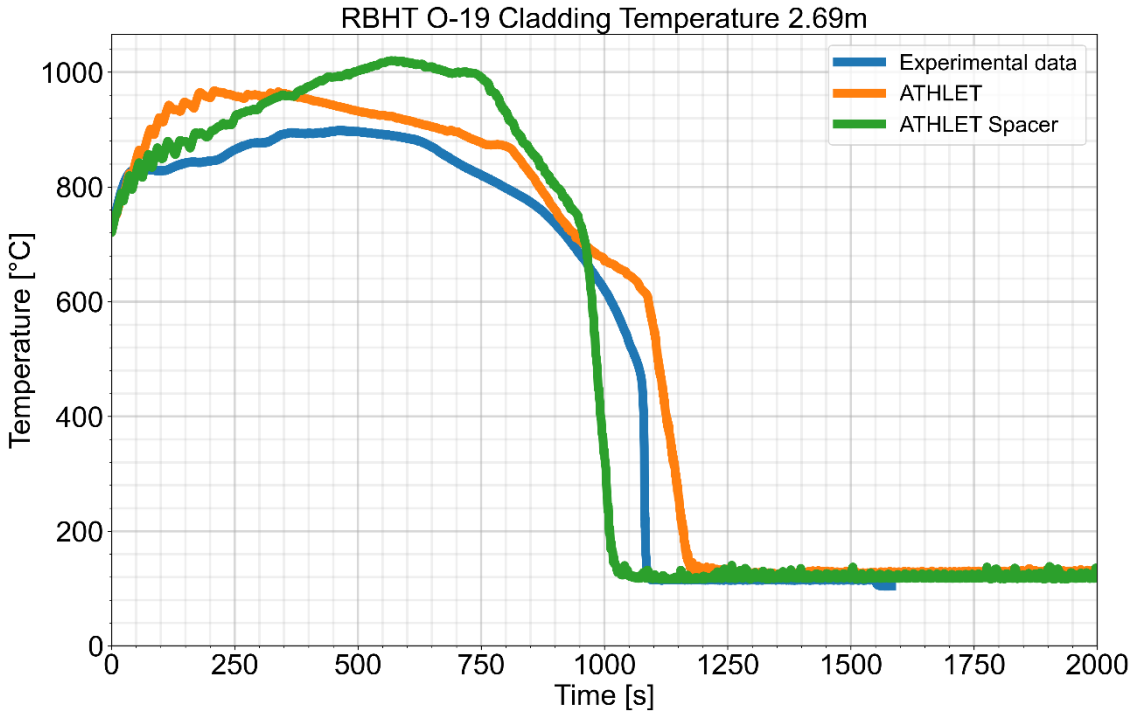

Fig. 7.4 Cladding temperature at 2.69 m for RBHT test O-19

Over the 17 tests of RBHT Phase II, divided into 11 open tests to understand the facility and adjust the model and 6 blind tests, we see that peak cladding temperatures agree well with the experimental data. As the scatter plot in Fig. 7.5 shows, most tests fall within 30 K deviation from the experiment (yellow dotted line), many even within 10 K deviation (green dotted line). Only 4 of the tests fall outside of these limits.

However, when considering the temporal figures of merit, time to reach PCT (Fig. 7.6) and the quench time of the point of maximum power at 2.69 m (Fig. 7.7), we see that only a minority of the tests fall into the area of good agreement, while most points lie outside of the ± 50 s range. Particularly, we observe a clear tendency for ATHLET to reach PCT and quench early. This points to overestimated heat removal.

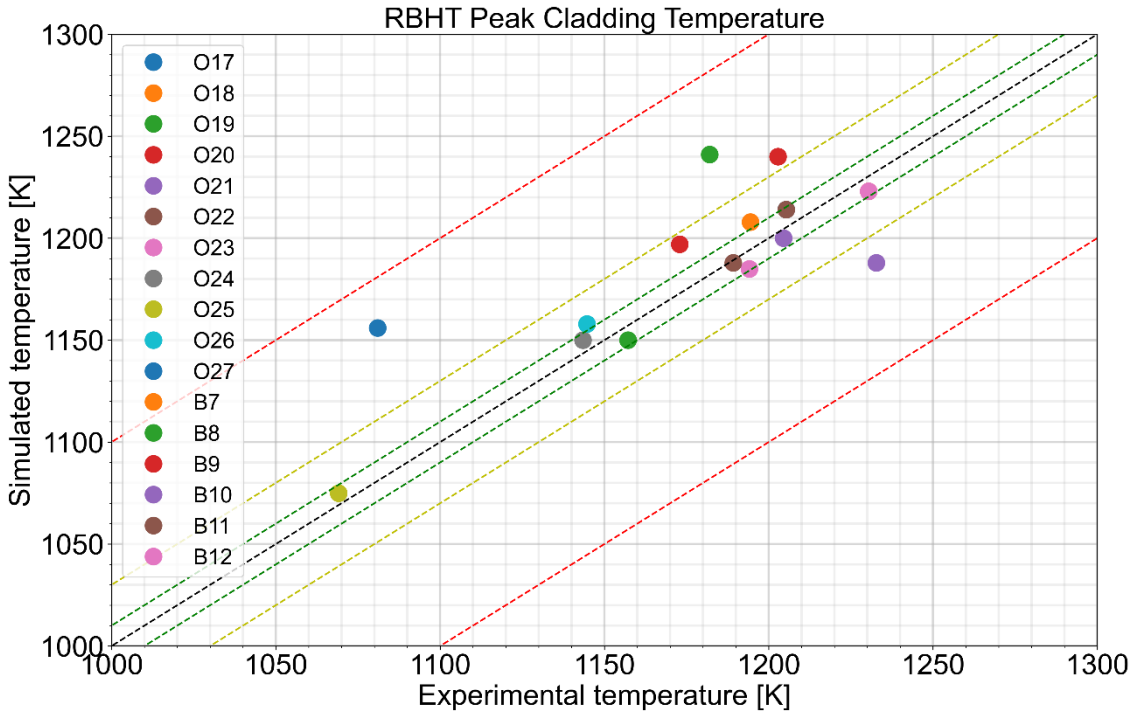

Fig. 7.5 Peak cladding temperatures across the 17 RBHT phase II tests

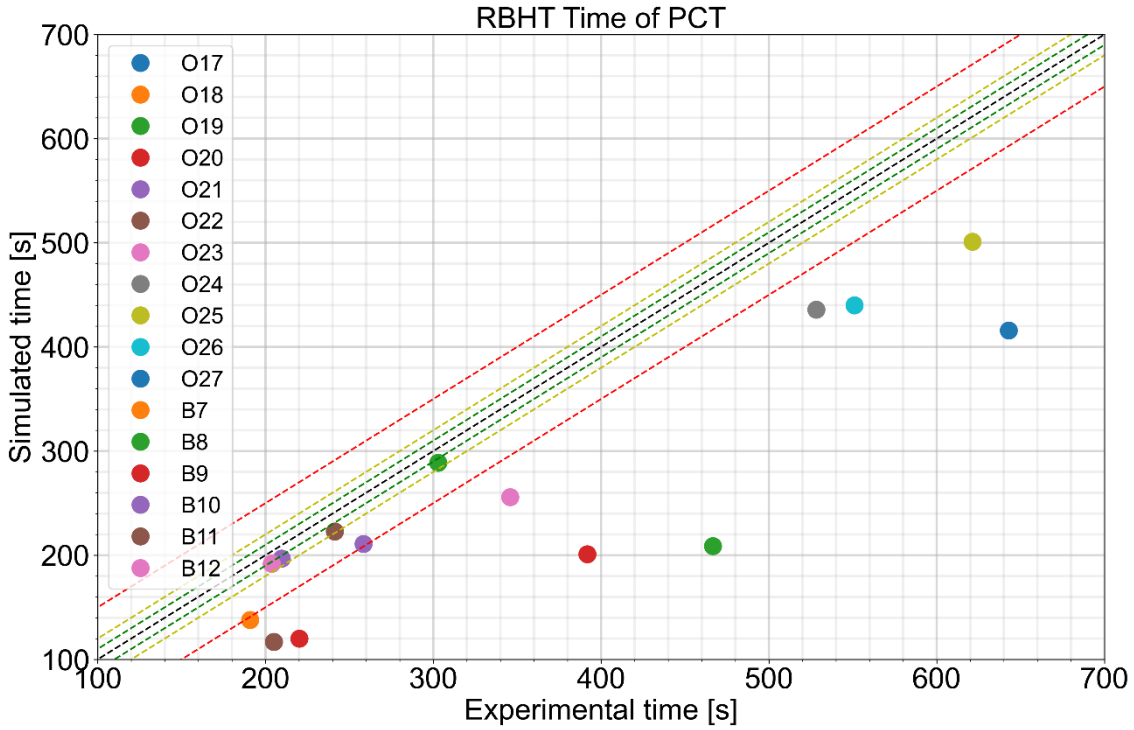

Fig. 7.6 Time to reach the peak cladding temperature in the 17 RBHT phase II tests

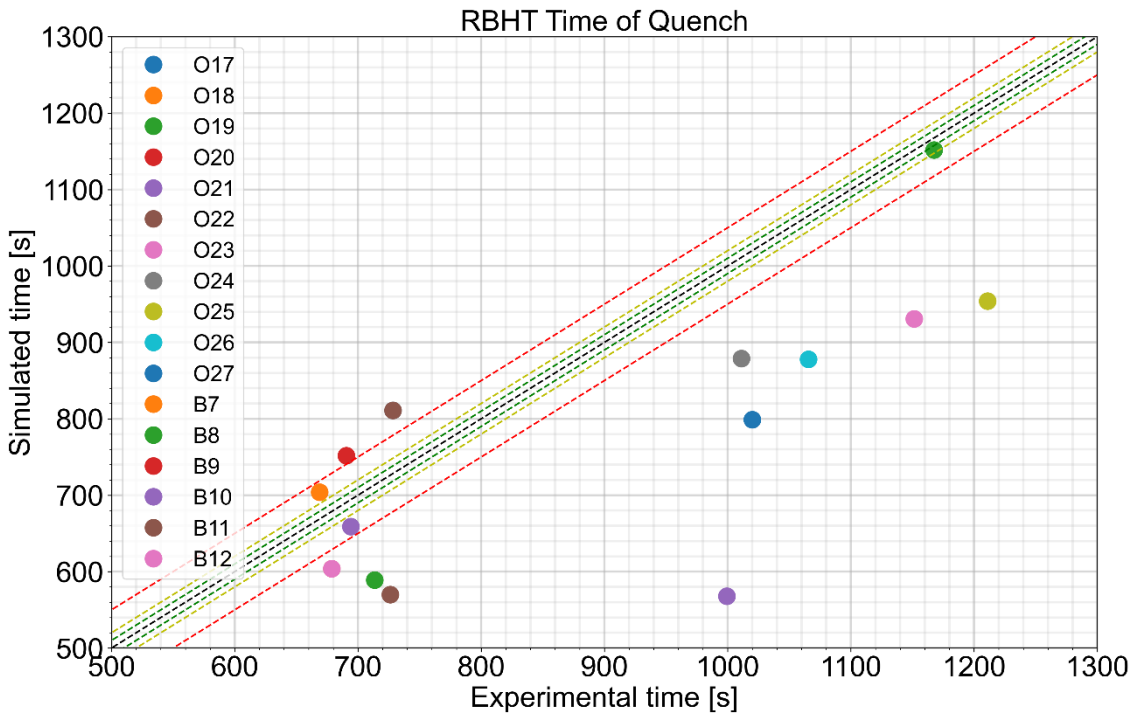

Fig. 7.7 Quench time of the point of maximum power in the 17 RBHT phase II tests

7.1.3 Summary

GRS participated in the OECD/NEA RBHT Phase II project, performing open and blind calculations to test the code performance in very low velocity reflooding cases. The international cooperation between different organisations and simulation codes allows to identify short comings of simulation codes in general and ATHLET in particular. The test data obtained from participating in the benchmark is used for model development and validation.

The recently developed spacer grid model performs well just above spacer location, especially for the fast tests at low pressure, reproducing characteristic trends of the cladding temperature that were not captured before and predicting peak temperatures better. For locations further away from nearest upstream spacer, the model needs to be revised to achieve improved results.

Overall, peak cladding temperatures calculated with ATHLET agreed very well with the experiments, while the times to reach the peak temperatures and to quench the bundle tend to be underestimated.

7.2 International AC² User Meeting 2025

To ensure an intensive exchange and effective use of external findings, a three-days hybrid AC^2 User Meeting 2025 was held at the premises of GRS Cologne in November 2025 with more than 70 external registrations from German and international research institutions, universities, technical safety organizations and authorities. In about 40 presentations the recent developments, validation results and application experiences related to AC^2 were overviewed by GRS and external code users and developers. E.g., new models and features of the current ATHLET program version 3.5 were presented to all participants /SCH 25a/. The highly informative event served in particular to exchange experiences and gather feedback on the program's application, so that this information can be taken into account in future program developments. Overall, the user meeting successfully gave the opportunity to maintain and strengthen bilateral contacts and advise program users in their application of ATHLET.

7.3 Co-operation within the FONESYS Network

Another aspect of the completed project concerned the collaboration within the international network FONESYS (The FOrum & NEtwork of SYStem Thermal-Hydraulic Codes in Nuclear Reactor Thermal-Hydraulics) of system code developing organizations /AHN 15/. Considered system codes are APROS, ARIANT, ATHLET, CATHARE, CATHENA, COSINE, LOCUST, MARS-KS, RELAP5, RELAP5-3D, SPACE and TRACE. One objective of the collaboration is to evaluate different system codes, to assess the suitability of the implemented models also with regard to the intended applications and to their scaling properties, and to derive suggestions for improving the implementation. To this end, the various system codes that are developed and applied by the FONESYS organizations are compared and assessed by benchmark activities. Current and future network activities were overview at the NURETH-21 conference /BES 25a/. Recently, GRS participated within several benchmarks presented in detail in the sections below. Related to these benchmarks and together with FONESYS partners, several papers were published at the NURETH-21 conference /BES 25b/ /BES 25c/ /SCH 25b/.

7.3.1 Core-3D Crossflow Benchmark

The Core-3D-Mixing benchmark initiated by the FONESYS network aimed at the investigation of the 3D flow modelling by system codes for the reactor core at reflooding conditions during IB- or SB-LOCA /SCH 25b/. The main objectives of the benchmark were:

- To investigate the predictions of radial transfers in a core bundle under single-phase vapor flow conditions
- To evaluate the sensitivity of crossflows to the modelling of radial friction pressure losses and of axial pressure losses induced by spacer grids
- To clarify the capabilities and limitations of momentum equations used in 3D solvers, in sub-channel models, or in parallel channel models with cross-flow junctions; e.g. in ATHLET, fully 3D as well as simplified parallel channel 1D momentum balance equations are available.
- To investigate the impact of the radial space resolution on the predictions.
- To evaluate the relative impacts of the radial diffusion and dispersion terms on the crossflows; those terms aren't implemented in ATHLET yet, however, depending on their significance, their implementation could be envisaged for the future.

The benchmark was split into two phases. Phase one focused on the bundle crossflow in the single-phase vapor region above the swell level. In phase two, the complete bundle height was simulated to additionally consider two-phase mixing below the swell level. Results are presented in the following sections. Complementary tests not presented here mainly investigated the influence of unbalanced mass flow and density inlet conditions applied to the simulated fuel assemblies.

7.3.1.1 Flow Mixing above Swell Level

Regarding the benchmark definition, a situation was considered with a partially uncovered PWR core with a decay power of about 3 % of the nominal power. A swell level was assumed with a pure vapor flow above. The part of a core above the swell level was simulated, consisting of two 17x17 PWR type assemblies of height 1.5 m with the right hot assembly (HA) having 42.8 % more power than the left cold assembly (CA) as shown in the Fig. 7.8. All the rods in each assembly have the same power and the power is axially constant. Two different pressures (7 MPa and 1 MPa) were considered as shown

in Tab. 7.2, mainly to produce different flow phenomena, chimney type (buoyancy-driven) and diverging type (friction-driven) crossflows, respectively. A pure saturated vapor flow was assumed at the inlet of the calculated zone with a radially homogeneous velocity profile.

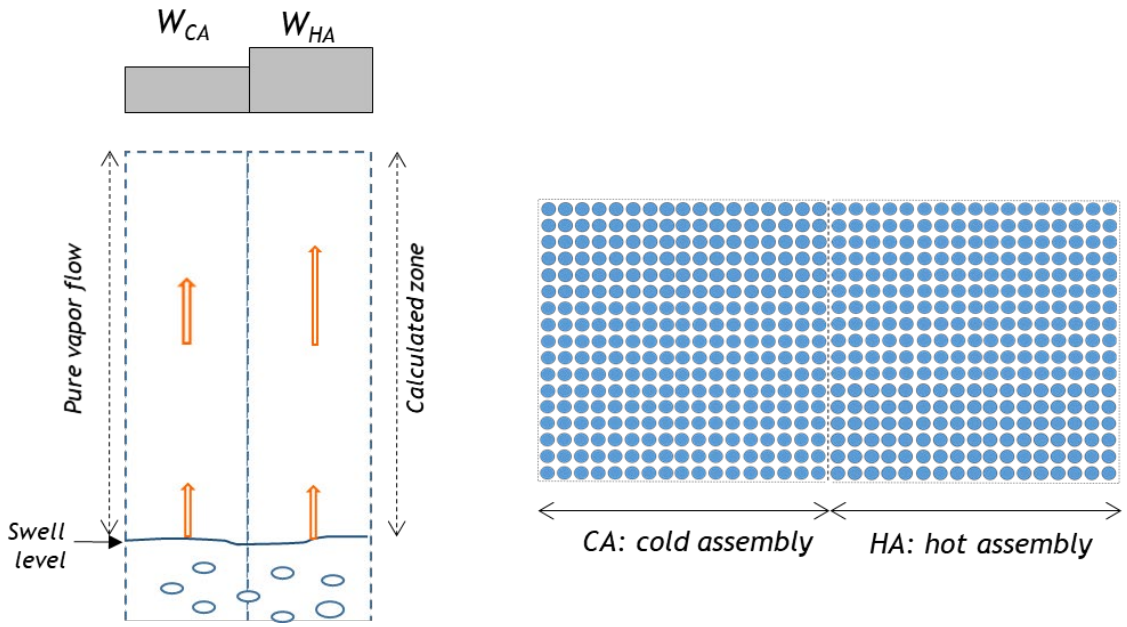

Fig. 7.8 Core crossflow benchmark definition /BES 23/

Tab. 7.2 Boundary conditions for cross flow benchmark

Reference	Exit Pressure MPa	Assembly	Heat flux W/m²	Inlet vapor flowrate kg/s
BC1	7.0	CA	$1.4\ 10^4$	0.175
		HA	$2.0\ 10^4$	0.175
BC2	1.0	CA	$1.4\ 10^4$	0.134
		HA	$2.0\ 10^4$	0.134

The nodalization adopted for the benchmark is depicted in Fig. 7.9. Each FA was represented by one TFO and one HCO with 15 axial nodes each. Both fluid channels were connected by crossflow junctions. FILL components at the bottom and a time-dependent volume (pressure-enthalpy boundary condition) at the top were used.

Three different sets of equation systems were investigated with ATHLET:

- 3D model based on 6-equation system (3D)
- 6-equation 1D model (2m)
- 5-equation 1D model with one common momentum equation and drift model for consideration of relative velocity between phases (1m)

It has to be noted that ATHLET's model equations come without specific terms for the simulation of radial turbulent diffusion or dispersion of void, energy or momentum. It is expected that these terms play a larger role for higher grid resolutions typical for a sub-channel approach. For the benchmark calculations presented here, a coarse nodalization (assembly-wise) was employed.

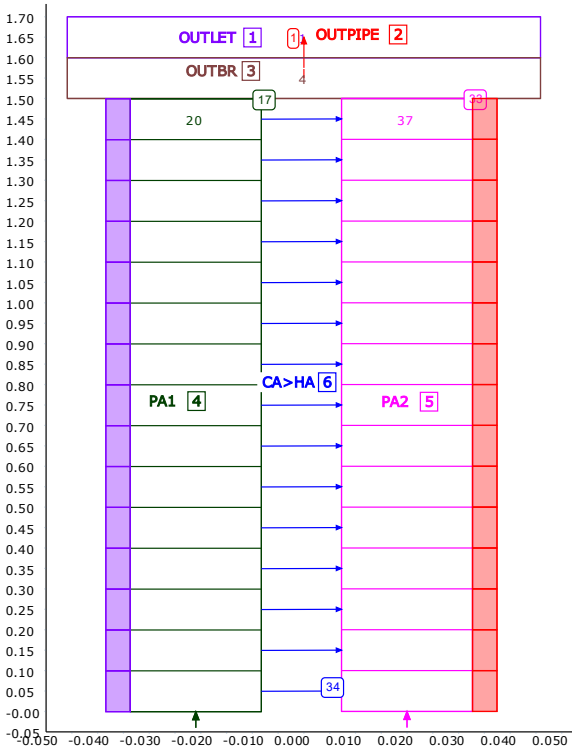

Fig. 7.9 Nodalization scheme for core crossflow benchmark

The results for the high-power boundary condition at 7 MPa are illustrated hereafter. Overall, the mass flow rate in the hot assembly increased along core height, whereas the mass flow rate in the cold channel decreased (Fig. 7.10). I.e., a chimney effect could be observed with improved cooling of the hot channel by mass flow entering the HA from the CA. At the spacer grids, which are simulated by a dimensionless form loss $\zeta = 1$ and

illustrated by the horizontal dashed lines in the figures, a homogenization of the flow could be observed. In general, results with 3D and 6-equation models were very similar. The 5-equation model behaved qualitatively comparably but provided some unexpectedly large spikes below bundle exit introduced by the boundary condition, as illustrated in Fig. 7.11.

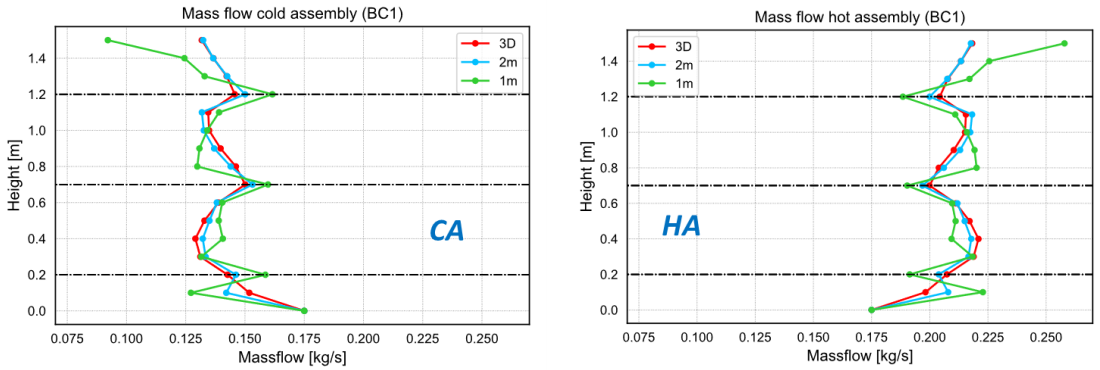

Fig. 7.10 Axial mass flow rate in cold and hot assembly at 7 MPa

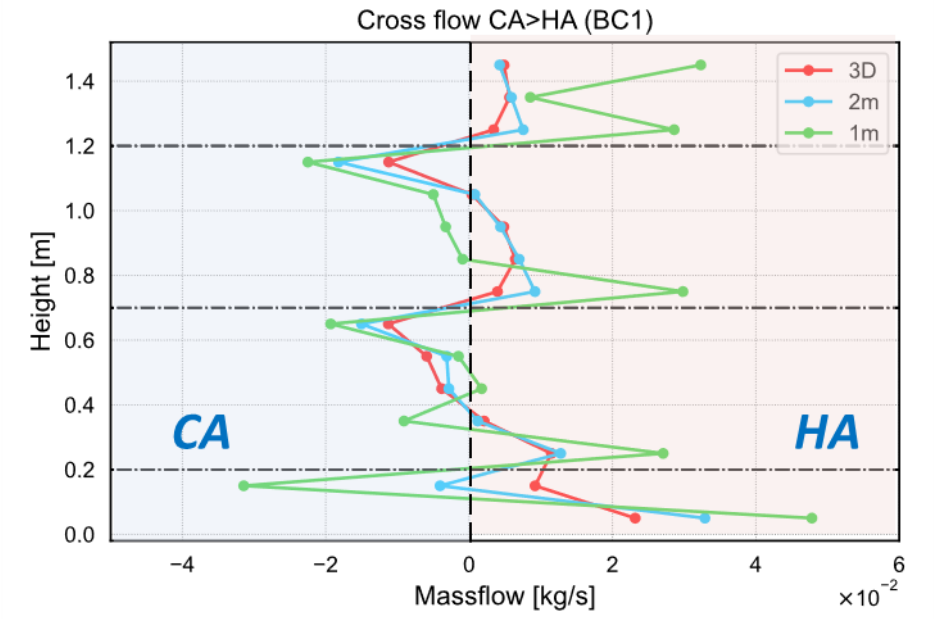

Fig. 7.11 Cross flow along fuel assemblies

The sensitivity of radial friction loss on crossflows was investigated by varying the friction loss coefficient for the horizontal flow. The range investigated covered typical values for laminar to turbulent flows perpendicular to a bundle. Only little impact on crossflow could be found for 3D and 2M 6-eq. models, as shown in Fig. 7.12.

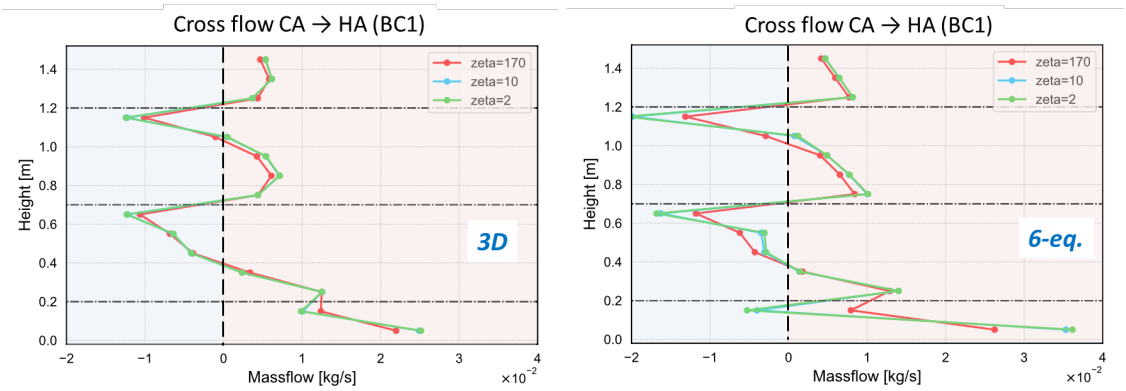

Fig. 7.12 Impact of friction loss coefficient on cross flow for 3D (left) and 6-equation (right) models

For the low-pressure boundary condition of 10 MPa, an overall crossflow from hot to cold assembly was found, that resulted in a reduced cooling of the hot channel. Again, results with 3D and 6-eq. models were very similar, whereas for the 5-eq. model a strong cross-flow below the bundle exit established.

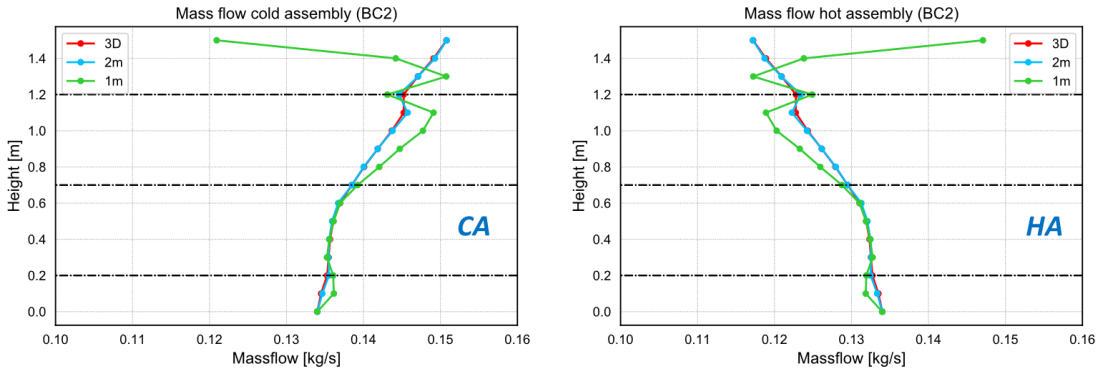

Fig. 7.13 Axial mass flow rate in cold (left) and hot (right) assembly at 1 MPa

As a result, ATHLET is able to predict the effect of pressure on cross flows that change their orientation from cold to hot assembly or vice versa depending on the pressure level. For high pressure, the gravitational contribution in the cold assembly dominates the high velocity frictional losses in the hot assembly, so that higher pressures in the cold assembly cause cross flows from cold to hot, denoted as chimney type flow. For low pressure, divergent flow from hot to cold assembly establishes, since frictional pressure losses dominate gravitational terms /BES 18/. These flow phenomena could be successfully reproduced by ATHLET, which is of high significance for the realistic prediction of the core cooling under SB-LOCA or IB-LOCA conditions.

All system codes that participated in the benchmark (ATHLET, CATHARE, COSINE, LOCUST, RELAP-3D and SPACE) were able to predict vapor friction-driven crossflows at low pressure (1 MPa) and buoyancy-driven crossflows (chimney effect) at higher pressure (7 MPa) /SCH 25b/. The diverging crossflows establishing under low pressure BC2 conditions yield significant effects on rod surface temperatures as depicted by Fig. 7.14 for ATHLET. The temperature difference between CA and HA depended on the codes and ranged from 270 k to 345 K for BC2. Root cause are the different wall to vapor HTCs. A detailed comparison of models and possibly further validation against experimental data is intended for the future to clarify the outcome.

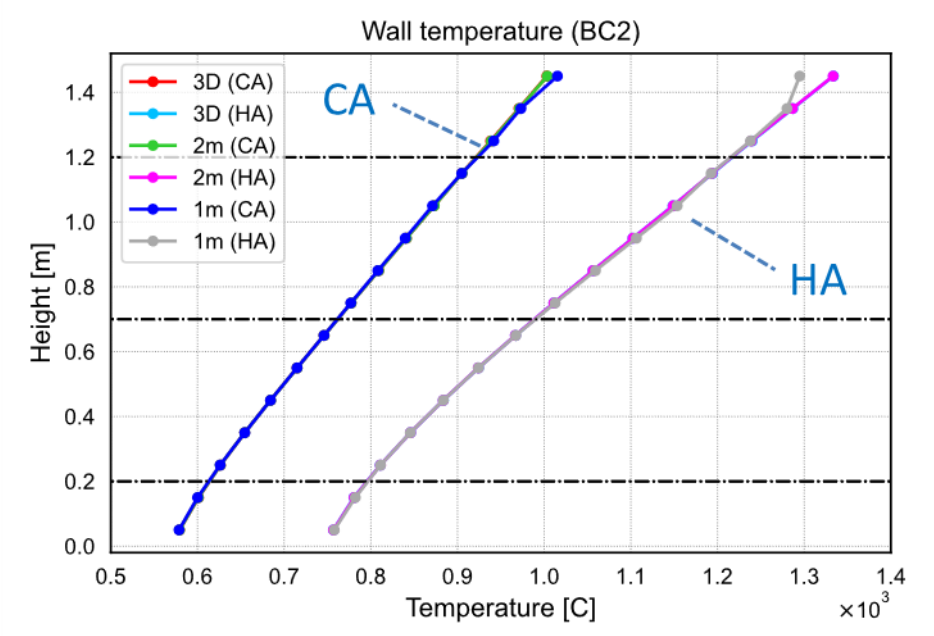

Fig. 7.14 CA and HA wall temperature for BC2 at 1 MPa

7.3.1.2 Core-3D Mixing with Full Height Bundle

The following complementary tests BC3 and BC4 are similar to the two cases with boundary conditions BC1 and BC2 but with a modelling of a lower plenum (LP), an upper plenum (UP) and a 3 m high core with a lower part in two-phase region and an upper part in single phase vapor region to investigate cross flow processes below and above the swell level. Another difference to BC1/BC2 is that the inlet flow rates at bottom of assemblies CA and HA are no longer imposed, but result from buoyancy and friction forces that may create recirculation through the lower plenum. Main objectives of these tests were to:

- compare radial crossflows between CA and HA in two-phase zone (and in vapor zone),
- compare the radial void homogenization in the two-fluid zone below the swell level,
- check if homogeneous swell levels in CA and HA as well as equal vapor flowrates at swell levels in CA and HA are predicted.

Boundary conditions for the two bundles with an un-balanced heating to induce cross-flows are summarized in Tab. 7.3:

Tab. 7.3 Boundary conditions for tests BC3 and BC4

Reference	Exit Pressure MPa	Assembly	Heat flux W/m²	Inlet liquid flowrate kg/s	Inlet liquid temperature °C
BC3	7	CA	$1.4\ 10^4$	0.35	285
		HA	$2.0\ 10^4$		
BC4	1	CA	$1.4\ 10^4$	0.286	179
		HA	$2.0\ 10^4$		

The ATHLET geometry model (Fig. 7.15) considers the lower and upper plenum by extra CVs to enable a free flow distribution to the bundles.

ATHLET, CATHARE and SPACE calculated very different inlet liquid flowrates in CA and HA, with two positive flowrates and higher flow rate in HA determined by ATHLET and SPACE, and recirculation through CA determined by CATHARE. The different inlet liquid flowrates may partly result from different interfacial friction values calculated in the bundle. The void profiles below the swell level in CA and HA were almost equal for the three codes, demonstrating an efficient void homogenization. For BC3, results achieved with ATHLET are illustrated in Fig. 7.16 and Fig. 7.17. The higher HA inlet flow rate enables consistent cross flows from HA towards CA below the swell level at about 1.5 m elevation. Above the swell level, results similar to those of BC1 were achieved. The void profiles determined for HA and CA were almost identical. 2m and 3D models provided comparable results.

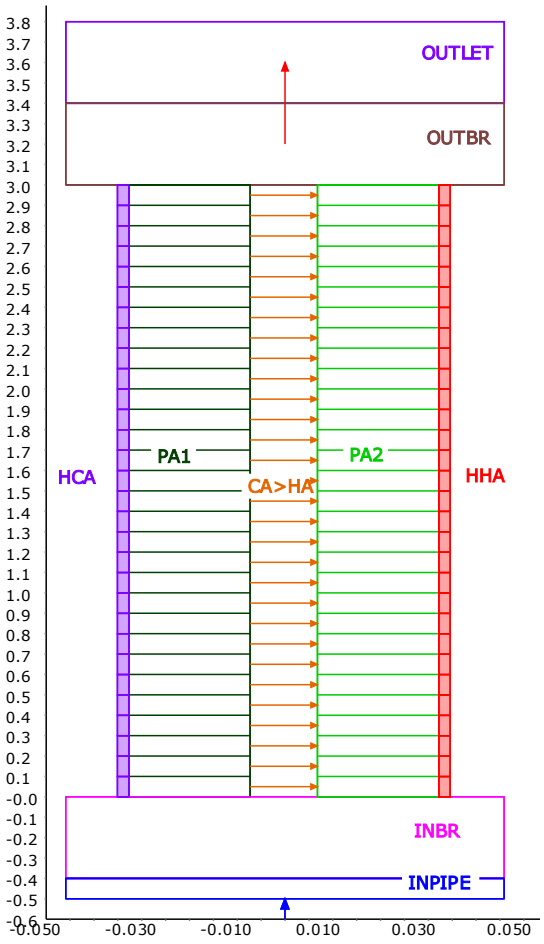

Fig. 7.15 Assembly-wise nodalization adopted to BC3 and BC4 cases

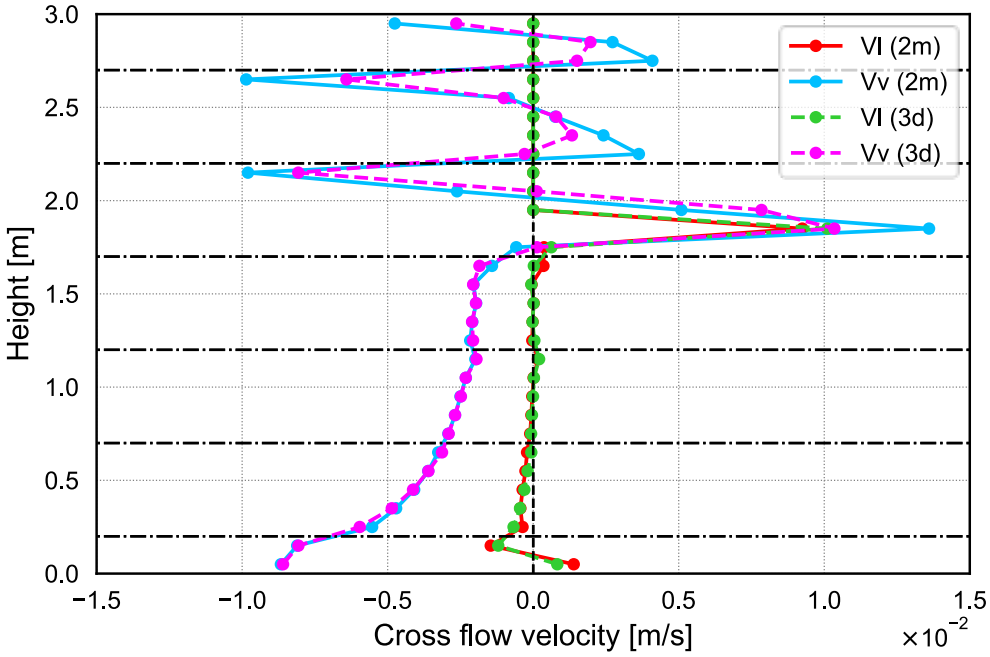

Fig. 7.16 Liquid and vapor cross flow velocity for BC3 (2m vs. 3D)

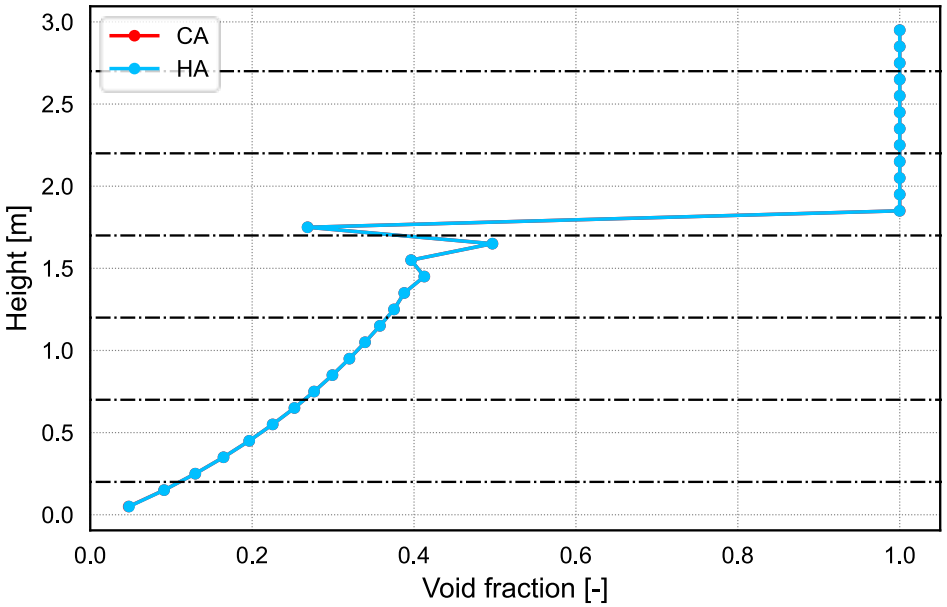

Fig. 7.17 Void fraction in CA and HA for BC3 (3D)

7.3.1.3 Summary

All codes predicted vapor friction-driven crossflows at low pressure and buoyancy-driven crossflows (chimney effect) at high pressure in the vapor region above the swell level in the bundle. The homogenization of void fraction below the swell level was predicted by

all codes, so that equal swell levels established in the simulated assemblies. Generally, the spacer grid form losses supported a flow homogenization between the assemblies.

Significant differences between the codes were found for the HTC for wall to vapor convection, causing differences in the rod surface temperatures. The interfacial friction and the (3D) wall friction are sensitive in the two-phase zone. Different models employed by the investigated system codes influenced inlet mass flow distribution to the assemblies and the cross flows below the swell level.

With regard to ATHLET, the three investigated model equation systems, 3D, 6-eq. and 5-eq. provided qualitatively comparable results, so that they are all suited to simulate the underlying physical phenomena. But the 5-equation model tends to provide cross flow with some non-realistic sharp spikes, in particular upstream the core exit. Most likely, this behavior is a consequence of the discretization approach selected for the momentum equation of the 5-equation model, which provides (compared to 3D and 6-eq.) a very loose coupling of momenta between subsequent junctions. Considering this, the 3D and 6-equation models are recommended.

For the future, the extension of the momentum equation by dispersion and turbulent diffusion terms could be conceivable. Under certain conditions and using finer (e.g. pinwise nodalizations), these terms can be relevant for the determination of cross flow transfers and related cladding temperatures /FU 19/. In future, tests from new experimental facilities like PRIUS (KAERI) and METERO (CEA) could be used to further derive and validate these terms. A related OECD/NEA project named PRIME is currently under preparation.

7.3.2 Bundle Interfacial Friction

Within the FONESYS group, one important activity was related to the investigation of the interfacial friction models for bundle geometry used in current system codes. The interfacial friction model is often derived from a drift flux approach (e.g. ATHLET or CATHARE). Rarely, the interfacial friction is purely calculated on the basis of flow regime dependent friction factor correlations. The interfacial friction model for a vertical bundle in ATHLET distinguishes between non-dispersed flow (based on a drift flux approach) and dispersed flow. For dispersed flow, a dedicated interfacial friction factor is calculated, which is then superposed with the non-dispersed flow interfacial shear coefficient. Only the non-dispersed interfacial friction was element of the benchmark.

Interfacial friction plays a dominant role in rod bundle thermal-hydraulics of LWR and determines, e.g., the initiation of DNB or dryout and the reflooding process. Therefore, it highly impacts the PCT as an important safety acceptance criterion. Thus, the interfacial friction modelling used in vertical bundles was selected for further analysis and comparison between participating codes.

The main objective of this benchmark was to investigate the scalability of the used core interfacial friction models with regard to effects of geometry, length scales, pressure, flowrate, and fluid properties. Analyzed conditions comprised low flowrate (when wall friction is small and void fraction depends only on a balance between buoyancy force and interfacial friction), the pre-CHF bubbly-slug-churn and annular flow regimes (without drop entrainment), and range of void fraction of $0 < \alpha < 0.8$.

The models used in the different system codes were theoretically analyzed on the basis of the model equations /BES 25b/. For this analysis, simplifications were adopted:

a) neglecting wall friction and momentum flux to get a simplified force balance, where buoyancy equals interfacial drag;

b) pressure constant along with the bundle elevation. In a second step, code calculations employing the full interfacial friction model and full momentum balance were performed to confirm the trends of the theoretical analysis.

7.3.2.1 Investigation of Model Scaling Properties

For the interfacial friction model analysis, the void fraction is the main output quantity. It depends on the quality of the inlet flow at the bottom of the bundle. To compare interfacial friction models, void fraction can be evaluated against the superficial vapor velocity in the test section, which can be altered by varying the inlet void fraction and keeping the total mass flux constant.

Simple bundle test section was defined:

- Unheated, no inverse flow regimes
- Void fraction variation, kept below $\alpha < 0.8$
- Pressure variation: for $G_0 = 10 \frac{\mathrm{kg}}{\mathrm{m^2\ s}}$: $P = 1, 2, 3, 5, 10, 20, 40, 70, 90, 120\ \mathrm{bar}$

- Mass flux variation: $G_0 = 10,\ 50,\ 100,\ 250\ \frac{\mathrm{kg}}{\mathrm{m^2\ s}}$
- Geometry variations: different LWR typical hydraulic diameters, see Tab. 7.4

Tab. 7.4 Geometrical characteristics of the rod or tube bundles in LWR

N°	Reference Geometry	Rod (or tube) diameter (m)	Pitch (m)	Hydraulic Diameter (m)
1	900 MW PWR Core	0.0095	0.0126	0.0118
2	Peach Bottom BWR Core	0.014	0.0187	0.01795
3	PWR Steam Generator (Patricia SG2)	0.02222	0.0325	0.0383

7.3.2.1.1 Analytical Investigation and Code Comparison

The influence of the pressure on the void fraction was analyzed first, see Fig. 7.18. For pressures from 20 to 120 bar, the results of the different models are rather close to each other, but for α > 0.7 the results show different slopes, possibly due to different treatments of the transition to annular-dispersed flow.

Differences are significantly larger between the codes for lower pressures. For 1 bar, the void fraction 0.5 is reached for a J_v equal to about 0.7 to 2.2 m/s. And for J_v=1m/s the void fractions vary in range 0. 3 to 0.55. Such big differences are beyond the measurement uncertainties and require further attention and validation against experimental data.

With regard to ATHLET and considering low pressure e.g. at 1 bar, two aspects are significant from Fig. 7.18: At low superficial vapor velocity (i.e. low velocity and/or low vapor fraction), ATHLET tends to a state with higher void fraction than the other codes. At higher superficial vapor velocity, the void fraction levels off first before rising rather steeply with a visible sudden dip in the curve.

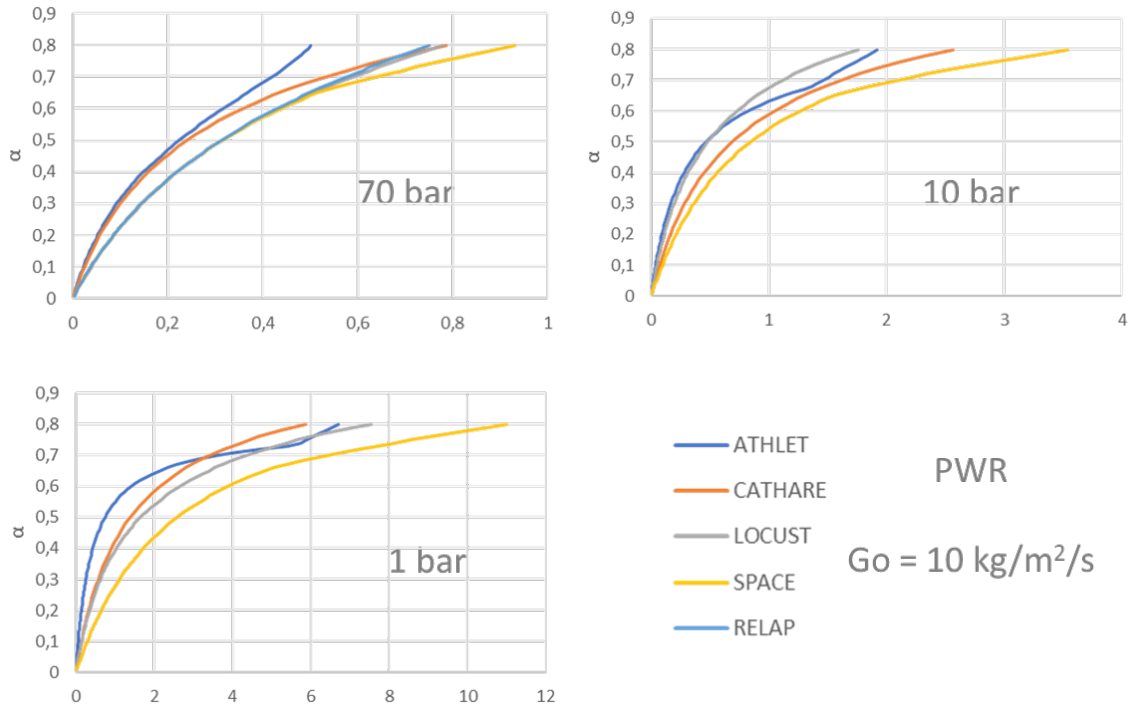

Fig. 7.18 Void fraction against vapor superficial velocity for different pressures /BES 25b/

For the evaluation of the density difference effect, model predictions for steam-water and air-water were compared. The different code models provided qualitatively comparable results.

For the evaluation of the geometry effect, the different hydraulic diameters presented in Tab. 7.4 were investigated. It was found that increasing d_h increases the interfacial friction and the void fraction in SPACE, LOCUST and RELAP-5 (all make use of an EPRI drift flux model) while it decreases the interfacial friction and the void fraction in ATHLET and CATHARE. To assess this contradictory outcome, one could compare the bundle trend with the trend found for pipe flows, by considering that for large hydraulic diameters bundle flow should approach the pipe flow behavior. Drift flux models for pipe flow predict a decreasing void fraction for increasing diameter, so that the results achieved by ATHLET and CATHARE seem to be more realistic.

Finally, the variation of mass flux has shown qualitatively similar results for all codes with decreasing void fraction when increasing the mass flux. Further details can be found in /BES 25b/.

7.3.2.1.2 ATHLET Calculations

Calculations performed with ATHLET for a simple bundle geometry as illustrated by Fig. 7.19 for the geometry 1 in Tab. 7.4 could confirm the trends derived from the theoretical interfacial friction model analysis.

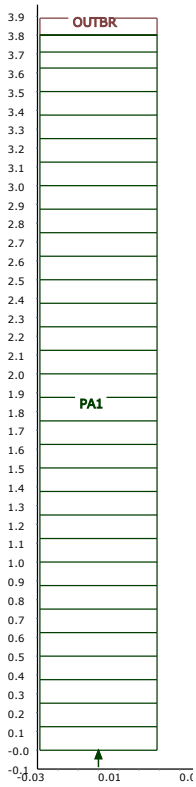

Fig. 7.19 Bundle nodalization for interfacial friction model analyses, mass flow boundary condition at the bottom and pressure boundary condition at the top

Further investigations focused on the origin of the void fraction dip found for interfacial friction calculation at low pressure, Fig. 7.18. Results of void fraction at an elevation of 3.2 m for mass flux $G_0 = 34 \frac{\mathrm{kg}}{\mathrm{m^2\ s}}$ are presented in Fig. 7.20. The curves reflect the expected trends with the dip observed for lower pressures. Calculations at pressures below 5 bar are not presented here. Due to the higher velocity (lower density) significant amount of entrainment was calculated by ATHLET, impairing the evaluation of the interfacial friction model based on drift flux model.

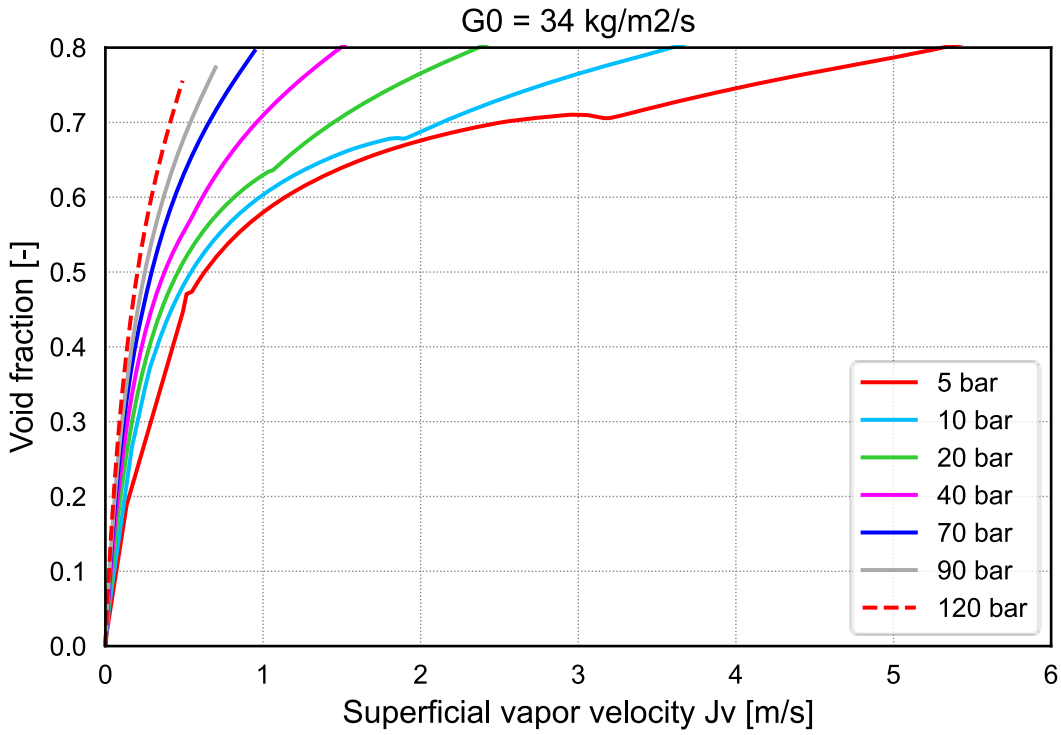

Fig. 7.20 Void fraction against vapor superficial velocity for different pressures

It was found that the dip can be attributed to the drift flux model formulation, where e.g. the flow regime dependent distribution parameter C_0 is determined based on a minimum criterion of three different correlations $C_0 = \min(C_{01}, C_{02}, C_{03})$ (for model details see /SCH 24b/). Fig. 7.21 illustrates the continuous, but not continuously differentiable course of the phase distribution parameter.

Fig. 7.22 and Fig. 7.23 illustrate the course of C_{01}, C_{02}, C_{03} and C_0 (dotted line) for low and high pressure. The not continuously differentiable course at low pressure and void fraction of about 0.7 is responsible for the unexpected behavior of the interfacial friction model. In future, efforts should be made to improve the drift-flux model and, in particular, to achieve more realistic interfacial friction behavior at low pressures.

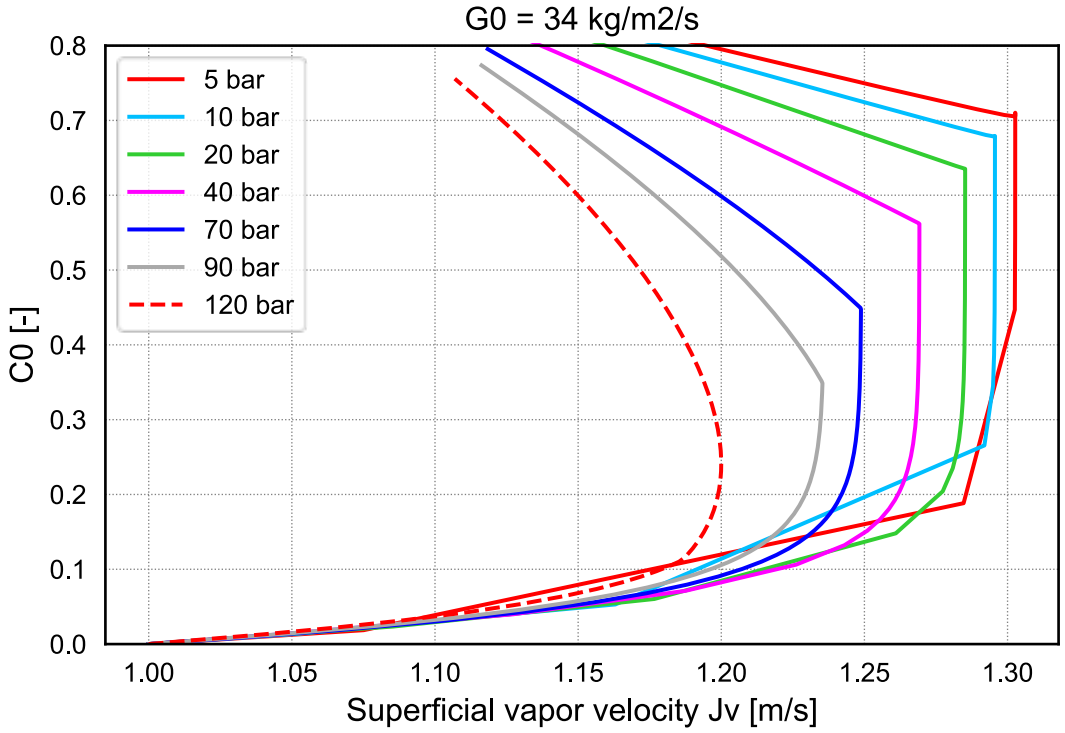

Fig. 7.21 Phase distribution parameter by superficial vapor velocity

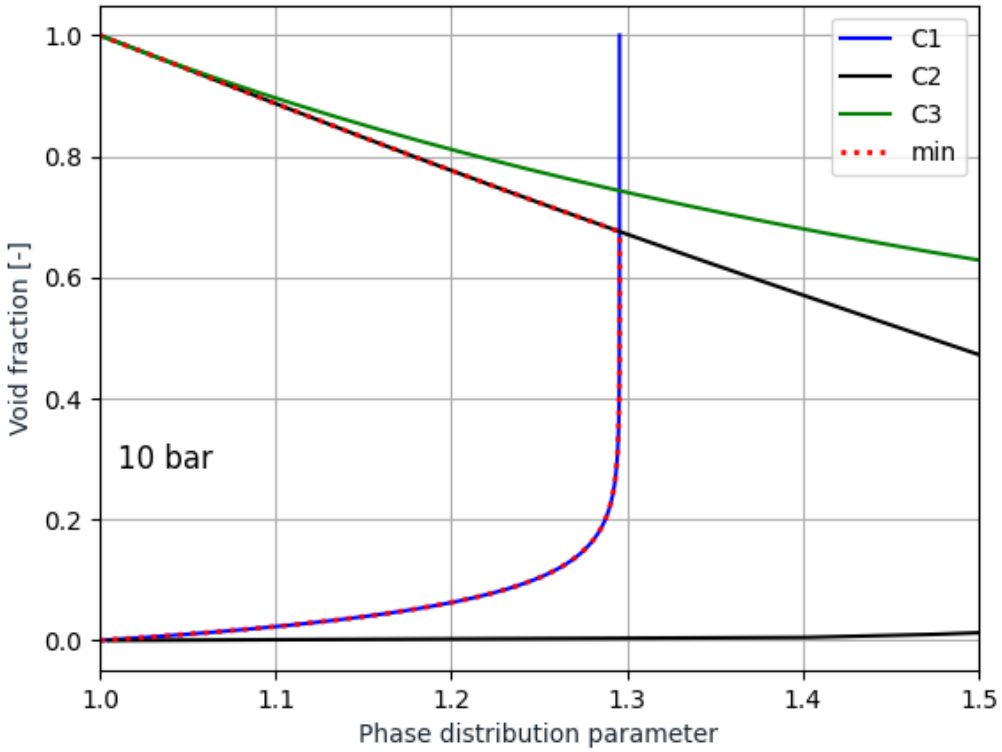

Fig. 7.22 Phase distribution parameter by void fraction at 10 bar

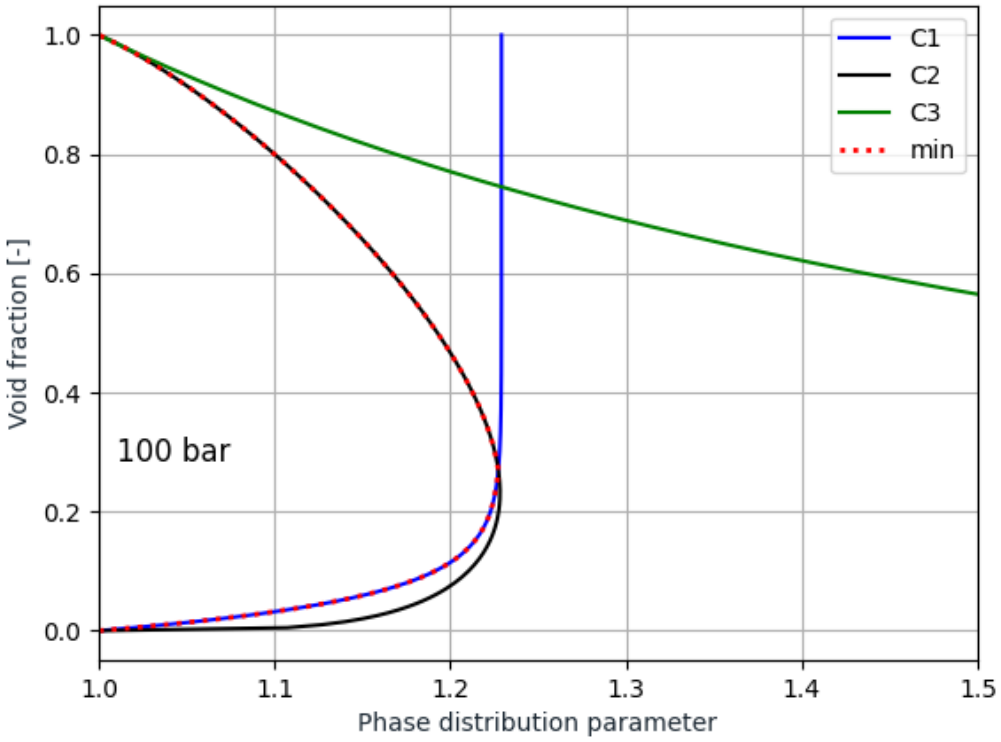

Fig. 7.23 Phase distribution parameter by void fraction at 100 bar

7.3.2.2 Bundle Interfacial Friction Validation against SIRIUS-3D Experiment

To strengthen the theoretical results, recent experimental data with detailed rod bundle void measurements were used to validate the interfacial friction model and assess its performance. For that purpose, the CRIEPI (Central Research Institute of Electric Power Industry) bundle experiment was selected /ARA 22/. The publication provides void fraction data in a 5x5 BWR type rod bundle using a subchannel void sensor (SCVS) recorded with a wire mesh sensor. The database covers the following range of thermal-hydraulic conditions:

- Pressure: 1, 3 and 7.2 MPa
- Inlet liquid velocity: j_L=0.1, 0.3, 0.5 m/s
- Inlet subcooling: ΔT_{sub}= 7 K
- Wall heat flux: 5.2, 15, 26, 36, 46 kW/m² (corresponds to bundle power between 15 and 135 kW)

Six combinations of pressure and inlet liquid velocity were selected, where for each of these BC experiments with the five different wall heat fluxes were carried out. Thus,

experimental data were provided for 30 test conditions (Tab. 7.5). Void fraction measurements were performed at eight elevations (Fig. 7.24), where data are given for five of them in /ARA 22/.

Tab. 7.5 BC for tests 1 to 30 for the SIRIUS-3D experiment

Test #	Pressure (bar)	Velocity (m/s)	Heat flux (kW/m²)
1 to 5	10	0.5	5.2 to 46
6 to 10	10	0.3	5.2 to 46
11 to 15	10	0.1	5.2 to 46
16 to 20	30	0.3	5.2 to 46
21 to 25	72	0.5	5.2 to 46
26 to 30	72	0.3	5.2 to 46

The axial and radial power profiles of the heated bundle are uniform. Heat losses are claimed to be negligeable. The geometry of the 5x5 square array rod bundle is:

- Rod diameter 10 mm
- Pitch 13 mm
- Heated length 3710 mm
- 7 spacer grids at elevations (measured from bottom of heated length) 465, 977, 1489, 2001, 2513, 3025, 3537 mm

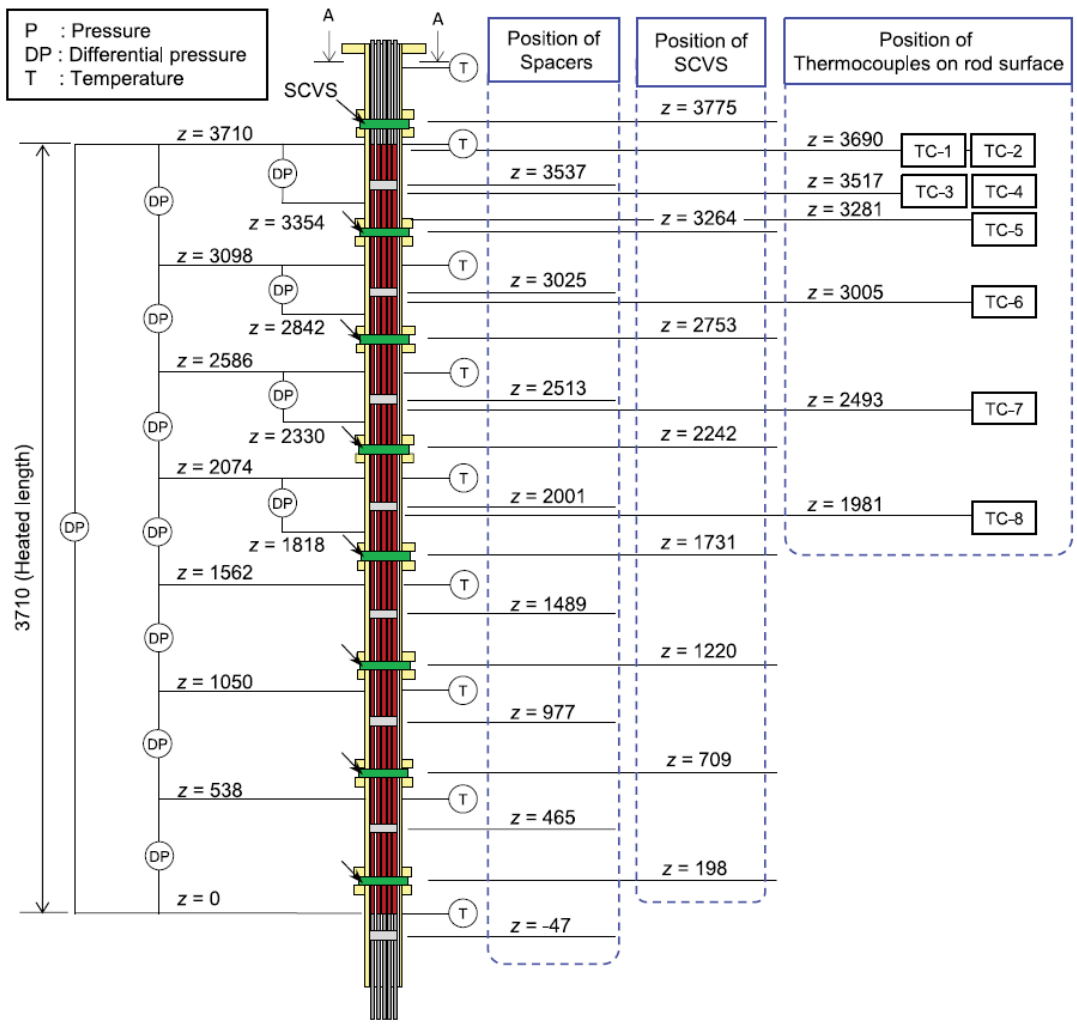

Fig. 7.24 Instrumentation for CRIEPI rod bundle test /ARA 22/

With ATHLET 3.4.2, post-test calculations with a single TH channel and with two parallel channels were carried out. Since the void fraction results didn't show a strong dependency on the nodalization, only results achieved with the single channel model depicted in Fig. 7.25 are presented here. Post test calculations were performed with both the 5-equation and the 6-equation models. Results are presented for the latter only. The friction losses at the spacer grids were considered by a constant dimensionless form loss factor $\zeta_{\mathrm{spacer}} = 1.4$.

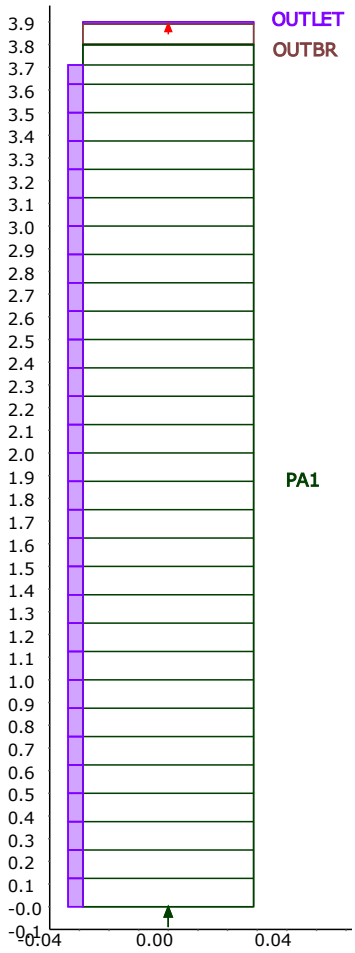

Fig. 7.25 Nodalization for CRIEPI rod bundle test calculations

The void fraction results found for the different BC and elevations are presented in Fig. 7.26 to Fig. 7.28 for low, medium and high-pressure conditions.

ATHLET tends to clearly overestimate void fraction at low void content, particularly for low pressure conditions. The overestimation is larger for low mass flux and low heat flux conditions. In addition, a slight underestimation of void fraction at high void content can be seen. It should be noted that particularly for high pressure and high mass flux conditions the interfacial friction model has to be proven to be highly performant.

Overall, sensitivity analyses performed with the 5-equation model provided quantitatively comparable results to the 6-equation model.

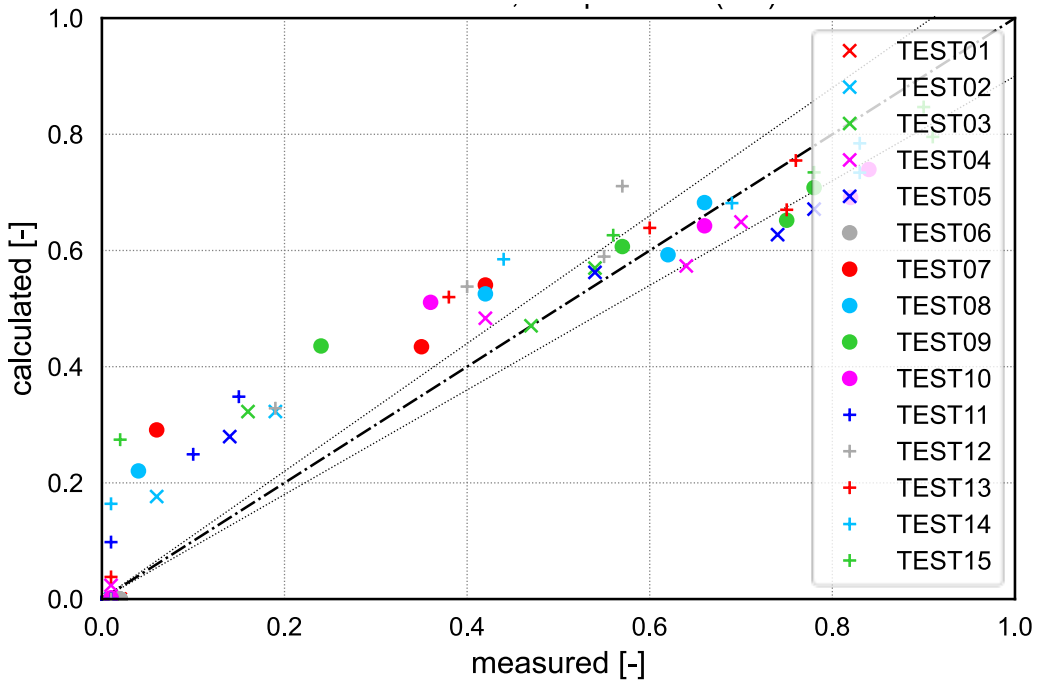

Fig. 7.26 Measured vs. calculated void fraction at 10 bar

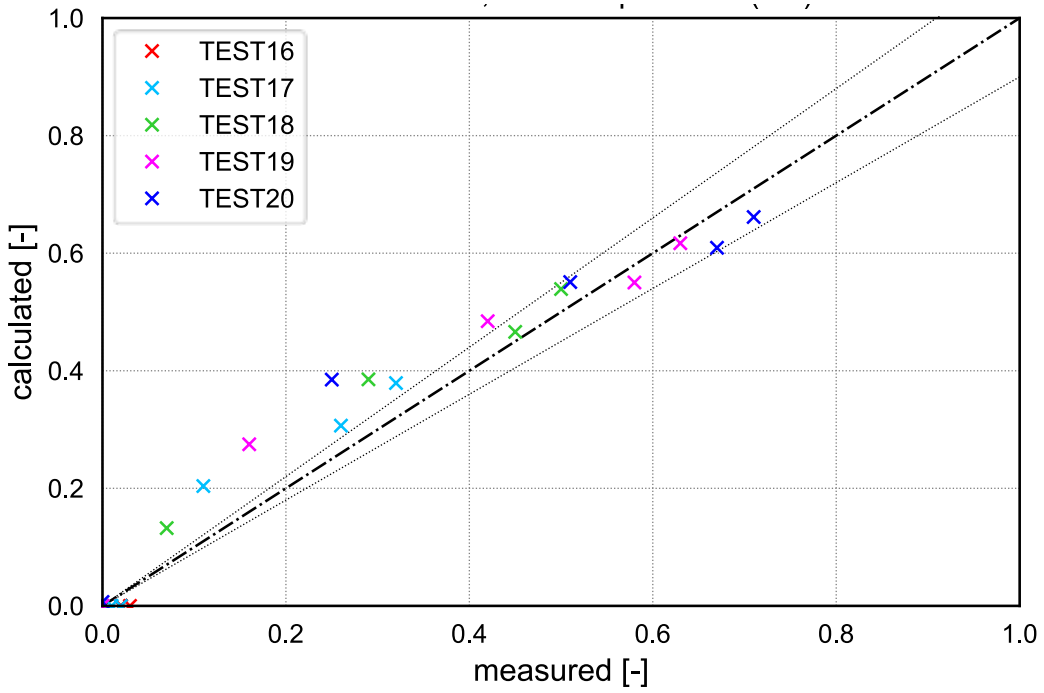

Fig. 7.27 Measured vs. calculated void fraction at 30 bar

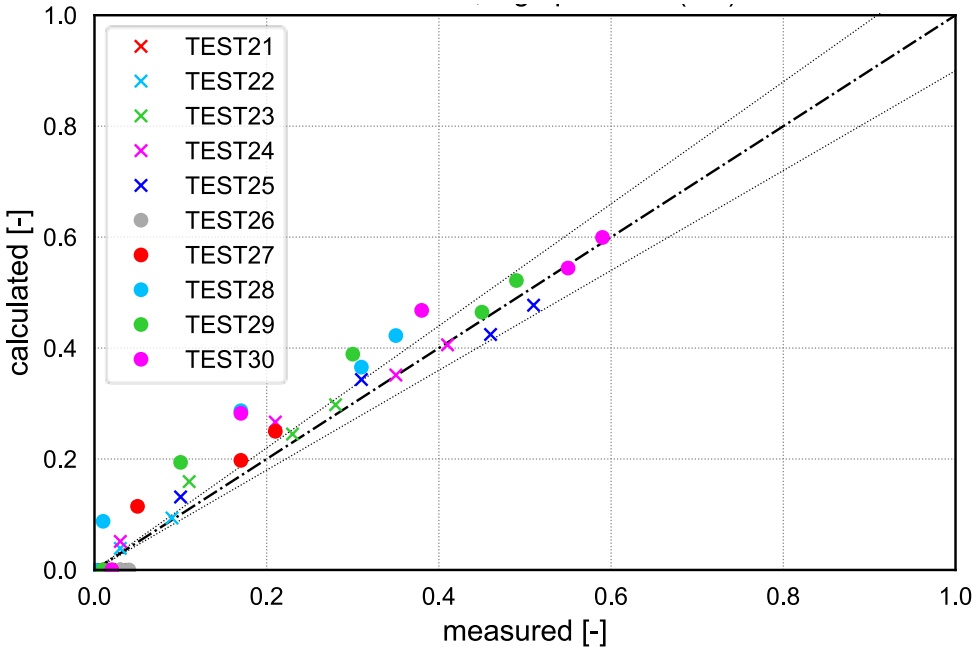

Fig. 7.28 Measured vs. calculated void fraction at 72 bar

The errors of ATHLET calculations against experiment data were calculated and they are given as a signed value (ME) and an absolute value (MAE) for void fraction as

$$\epsilon_\alpha = \frac{1}{n}\sum\left(\alpha_{\text{sim}} - \alpha_{\text{exp}}\right) \tag{7.1}$$

$$\epsilon_{\alpha,\text{abs}} = \frac{1}{n}\sum\left|\alpha_{\text{sim}} - \alpha_{\text{exp}}\right| \tag{7.2}$$

The ME, the MAE and the Root Mean Squared Error (RMSE) of these errors are tabulated (Tab. 7.6). The values are given in total for all experiments, but are also broken down by pressure level and power. Concerning pressure, largest errors are found for the low pressure (10 bar) experiments. In contrast, sensitivity to power is low, with a slight tendency to larger errors at highest power (46 kW/m²).

Tab. 7.6 Errors on void fraction with ATHLET 2M model and experiment

Experiments	ME	MAE	RMSE
All	0.020901	0.051556	0.073703
Low Press	0.027045	0.067013	0.092568
Mid Press	0.019284	0.042655	0.055358

Experiments	ME	MAE	RMSE
High Press	0.012493	0.032822	0.043713
Power 1	-0.00548	0.034519	0.053089
Power 2	0.044541	0.054541	0.079341
Power 3	0.039777	0.048606	0.069905
Power 4	0.019399	0.053681	0.07348
Power 5	0.006268	0.066433	0.088096

7.3.2.3 Summary

Main findings of the theoretical analysis of the bundle interfacial friction models used by different system codes are that significant uncertainties of the interfacial friction exist with regard to low pressure conditions and the dependency on the hydraulic diameter. For low pressure, the ATHLET model tends to higher void fractions than the other codes, a trend that is confirmed by the code validation against the CRIEPI rod bundle test. For high pressure, the benchmark shows a good agreement between the codes' interfacial friction models. The satisfying agreement between measured and calculated void fraction for the CRIEPI test indicates a certain maturity of the ATHLET modelling for high pressure conditions.

7.3.3 Singular Pressure Loss Calculation

System codes typically use 2-fluid 6-equation models (or even 3-field models) and predict wall friction and singular pressure losses by models originally developed for a unique mixture momentum equation. Two-phase multipliers exist to extrapolate 2-phase pressure losses from 1-phase models but the repartition between phases was not investigated in detail although it may have a significant effect on the phase distribution in the simulated system. The unclear repartition results in some uncertainty of predictions in high velocity flow and also in low flow natural circulation.

Considering this lack of knowledge, a code-to-code benchmark /BES 25c/ using ATHLET, CATHARE, MARS-KS, RELAP5, RELAP5-3D and SPACE codes was initiated to compare the predictions in three basic singular geometries comprising abrupt area restriction or enlargement, and diaphragm (Fig. 7.29). In a reactor circuit, there exist

several locations with comparable flow restrictions. Both vertical upward and downward flow were investigated in five different flow regimes (Tab. 7.7).

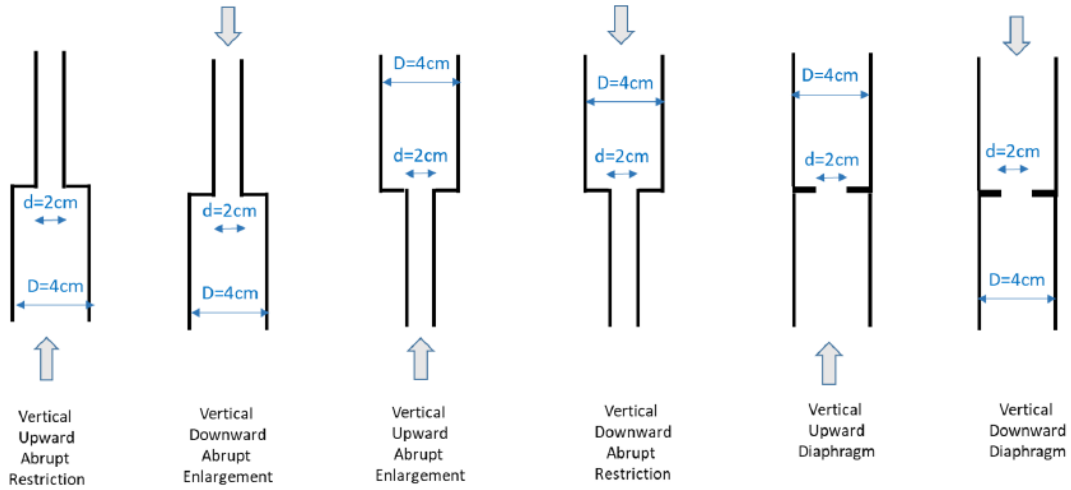

Fig. 7.29 Geometry and dimensions of the six geometrical singular pressure loss configurations /BES 25c/

Tab. 7.7 Inlet boundary conditions applied to the six geometrical singular pressure loss configurations

Reference	Velocity	Fow Regime	Total flowrate (kg/s)	Vapor flowrate (kg/s)
BC1	High	1-phase liquid	1	0
BC2	High	Bubbly	1	0.01
BC3	Medium	Slug-Churn	0.15	0.0084
BC4	Low	Slug-Churn	0.05	0.0028
BC5	High	Annular-Mist	0.1	0.062

The total pressure loss introduced by a local singular pressure loss may consist of two contributions, the actual form loss and an acceleration or deceleration pressure change. Both contributions were separately investigated in the frame of the benchmark.

The form loss coefficient K_{sing}, which is typically rather well known for single phase flow in simple geometries like the six investigated configurations, was given in the benchmark

definition. In ATHLET, the phase-specific singular pressure loss is calculated from the single-phase pressure loss coefficient as follows:

$$\Delta P_{\mathrm{sing},k} = -\alpha_k \frac{K_{\mathrm{sing}}}{A^2} \rho_{k,u} \frac{|V_k \cdot A| \cdot V_k \cdot A}{2} \tag{7.3}$$

Unlike the calculation of wall friction, no two-phase multiplier is used in ATHLET for the form loss calculation.

Spatial changes of the cross-sectional area result in a pressure drop (or pressure recovery) caused by flow acceleration (deceleration) due to flow area decrease (increase). This is considered by the momentum flux term of the phase specific momentum balance equations in either case, area restriction or area enlargement.

From the results achieved with the adopted system code, the following observations could be made:

- The total singular form loss ΔP_{sing} predicted by the various codes using the same coefficient K_{sing} had up to 50 % difference in the simplest case of a high velocity bubbly flow in area restriction or enlargement and up to a factor 2.2 in a diaphragm.
- In annular-mist flow regime, the ΔP_{sing} predicted by the various codes using the same coefficient K_{sing} had up to a factor 2.7 difference in area enlargement and in a diaphragm.
- The acceleration pressure change predicted by the various codes for area restriction or enlargement had up to 43 % differences. Highest deviations were found for the annular-mist flow regime, again.
- The differences between codes on form loss and acceleration pressure change are higher in vertical downward flow than in vertical upward flow. They are a little higher in an enlargement than in a restriction and highest for a diaphragm.
- The annular-mist flow is the flow regime with the highest uncertainty. It should be noted, that several codes (namely MARS, RELAP, RELAP3D, SPACE) had difficulties to achieve a stable steady state for annular-mist flow boundary conditions.

This benchmark also gave the opportunity to compare wall friction and gravity pressure gradients predicted by the various codes in established vertical flow upstream the singular pressure loss location:

- In the simplest case of a high velocity bubbly flow, there is a 36 % relative difference of predicted void fractions between codes in upward flow and a factor 2.7 in downward flow. The friction pressure gradients have a factor 2 maximum difference in bubbly flow.
- The relative difference in pressure loss in low velocity slug-churn flow is larger, but less important due to the generally small absolute pressure loss. However, for passive systems and natural circulation conditions, uncertainty can become significant.

With ATHLET, additional sensitivity calculations were performed investigating the impact of

a) the nodalization,

b) input settings with regard to the calculation of the momentum flux, and

c) the equation system, either one mixture momentum equation or two phase-separated momentum equations.

In general, results achieved with the different settings were in good agreement. However, larger relative differences for the singular pressure loss could be observed between the one and the two-momentum equation approach for BC3 and BC4 (medium or low velocity tests) and vertical downflow. Under these conditions, a negative relative velocity could partly establish pointing to a field with only poor validation basis.

Overall, and despite the fact that numerical results cannot directly be compared to experimental data, several conclusions can be drawn from the findings of the code-to-code benchmark. To improve code models for singular pressure losses, new experiments with local measurements of pressure and axial and radial void distribution may be necessary. New information could become available in future, since experiments on simple geometrical configurations are under preparation at the Bangor University, Wales, and may be accompanied by calculations within the FONESYS network. In addition, concerning developed flow in vertical pipe, the calculation of the interfacial friction, which depends also on the used flow regime map and drift flux model, needs to be revised to reduce existing uncertainties. With regard to the relevant models in ATHLET, potential for improvement

has already been identified in chap. 7.3.2 and, e.g., /SCH 24a/ and could be addressed in a follow-up project to UMRS1615. Furthermore, for several codes the simulation of annular flow turned out to be particularly difficult with regard to both physical results as well as numerical performance. Improved models and correlations seem to be indispensable to achieve a more realistic representation of phenomena in annular and annular-mist flow. In general, model uncertainties seem to be larger for downward flow than for upward flow.

8 Quality assurance

8.1 Refactoring

- In `gcmain`, the interpolation routine `gsvipo` is called for each GCSM block. It interpolated all process signals defined in the GCSM input irrespective of whether they were actually needed for the block or not. To address this problem, the process signals are re-ordered during input processing based on their appearance as input signals to controllers in the GCSM blocks. For each GCSM block, the process signal index of the first and the last signal to be iterated is saved. Then, `gsvipo` only iterates the process signals in that index range. This significantly reduces the computational overhead for defining a new GCSM block (and process signals for output purposes only) and avoids numerous unnecessary computations of process signals. The speed-up of GCSM depends on model size and structure, but is noticeable for large, complex models. Due to the limitations of the implementation (only the first and last process signal index are stored), the user still needs to support the effective evaluation of process signals by limiting the number of signals appearing in multiple blocks and by placing input blocks using the same process signals close to each other in the input deck.

- The work of putting subroutines into existing modules or specifically defined procedure modules was finalized, also for new procedures. Where this is not sensible, because procedures are exported externally without use of *libfde*, e.g. the main ATHLET procedure or the external coupling data interface, explicit interfaces are provided when these procedures are called in ATHLET. This enables additional compiler checks for detecting programming errors. It also facilitates the use of optional arguments or generic procedure interfaces for improving the code.

- In several procedures in ATHLET, e.g. in a MINPACK version and in interfaces to *libfde* procedures, internal procedures were passed on via a procedure pointer to subroutines called in the implementation (e.g. for iteratively determining a zero of a function). However, this requires giving the stack the executable flag, e.g. under recent Linux distributions. Since this is considered as an IT security weakness, the code was changed so that only module procedures or separate procedures with an explicit interface are passed on as procedure pointers. This included changes to the default hdf5 writer plugin of ATHLET.

- Runtime errors during input processing were prevented by using error branching for most of the read statements in ATHLET and several write statements, including repeatedly used write statements to generate files such as the .pd file. Now, errors in these input and output operations will trigger a controlled error end of ATHLET.

- The minmax file for minimum and maximum values of each plot variable determined by ATHLET during the transient calculation phase was removed. This post-processing task (on the plot vector) has no place in a transient simulation process.

- The extended input file that is generated when include files are processed is saved in the output directory (working directory) for the calculation instead of the location of the input file.

- If ATHLET is run coupled to COCOSYS, CW `CONTROL IPUNC` options for the restart file are adjusted to the only valid option `IPUNC` = 1

- During calculations for an RBMK input deck, it was noticed that the calculations ran into the lower time step limit imposed by the numerical resolution of `spacing(TIME)` for a double precision real variable at a simulation time of about 120,000 s. Since such analysis periods are expected to become important for future applications of ATHLET, e.g. for SMR relying on passive safety features, research reactors as well as interim storage casks, this limitation had to be addressed.
  Unfortunately, a lot of the models are calculating the current time step size based on the current absolute time value reached by FEBE during the time step and the absolute time value at the start of the time step. This is also due to FEBE not providing the current sub-time step value as a global variable, so that only the final time step value is available directly. Considering the numerical precision at around 100,000 s, numerical errors for small time steps at such simulation times could become considerable.
  The solution was to switch the main absolute time values in ATHLET to quadruple precision (128 bit). This allows to determine time differences in the respective ATHLET modules with sufficient precision. Wherever sensible, time values are reconverted to double precision values to utilize the significantly more performant numerics for 64-bit floating-point numbers. Importantly, all conversions to and from quadruple precision need to be explicit in the code, since automatic kind conversions produce numerical errors with the *ifort* compiler.

- In several procedures in ATHLET, numerically expensive time-dependent attenuation factors, e.g. of the type $\exp(-(T-T_0)/\tau)$, were computed in each iteration of

loops over all CV or junctions. Such common factors are now computed once outside of the loop and then used via simple multiplications in the loop, speeding up the code.

- In FEBE, the (minimum) perturbation of a solution variable for calculating the Jacobian was determined based on an L_2-norm of solution variable values. The drawback of this approach was that this perturbation value depended on model size (number of CV), as well as overall pressure and temperature levels, etc. For large models, minimum perturbations could be unreasonably large for quality-type solution variables. Now, the minimum perturbation is determined per solution variable using

  $$R_i \approx \max\left(10^{-6} \cdot |Y_i|,\ 10^{-6} \cdot \frac{\mathrm{CLIMV}_i}{\mathrm{EPS}},\ 3.648 \cdot 10^{-12} \left|\frac{dY_i}{dt}\right| \Delta T,\ 10^{-9}\right)$$

  For each variable, this combines a small fraction of its current value, the required accuracy, its time derivative multiplied with the time step and an absolute cut-off of 10^{-9}. This improves numerical efficiency.

- The error acceptance behaviour and time step reduction of FEBE were changed. Previously, an acceptance limit of 1.25 (on the maximum relative error) was used in all situations. Now, if the current time step `DT` < `ECKSCH`, the time step size for jumping over discontinuities, the acceptance limit is set to 1.5. Note that HXX events are already ignored, unless the `HXWSP` flag is set as well (e.g. for property package bound violations).

  If the time step falls further with `DT` $< 10 \cdot \max($`GRESCH`, `ECKSCH`$/100)$,

  a) the acceptance limit is increased to 2.0,

  b) if the time step is accepted, no decrease of time step size via error metric for the next time step is possible,

  c) if the time step is not accepted, the further reduction of the time step via error metric is limited to a factor of 0.8 (HXWSP events are not affected).

  Note that the calculation stops if the time step falls below `GRESCH`. Via input checks it is assured that `GRESCH` $\gg$ `spacing(TIME)` for the whole analysis period. These changes increase the resilience of ATHLET against stops due to numerical problems for a specific solution variable.

- TFD system names under CW `TOPOLOGY` can be input as strings and as positive integer numbers. If an integer number *n* is input, ATHLET assumes it is the nth TFD system in the input order. For a string, the system number in input order is also determined, and ATHLET requires that all TFD system are input in consecutive order,

starting with 1. In previous versions, it was not possible to effectively mix string and integer input for TFD systems, because integer input did not increase the counter for input order. This restriction was removed.

- Previously, plugins could not connect to a suitable hook for writing data into the plot file(s) and for reading restart data. These hooks were added and the hook for writing restart data was moved to a better location. In addition, variables for writing to and reading from the correct restart file were made available to plugins. Finally, a dedicated control word `PLUGININP` for input data to a user-defined plugin was provided. Therefore, plugins can now treat internal state variables and do consistent restarts and traceback and add data to the plot files. This has been demonstrated through a sample plugin. Further improvements to ensure that multiple plugins can reliably make use of these functions will be needed in the future.

- Tracebacks for a detected error or runtime error in ATHLET were only written to the .out-file if ATHLET was compiled with the Intel® Fortran compiler and run under Windows®. Now, this traceback information is also available for the Intel compiler under Linux® and when compiled with *gfortran*.

- At the end of an ATHLET run, file units were not systematically closed, relying instead on the default behaviour of the ATHLET process being terminated to achieve that. Also, the hdf5 file would not be flushed and closed unconditionally, e.g. in case of an error end to ATHLET. For external ATHLET controllers, such as the python controller, this could cause problems if multiple ATHLET simulations should be started from the same process. A dedicated finalisation procedure was written for ATHLET that comprehensively closes all potentially open file units, and triggers the same for ATHLET-CD. The hdf5 output is finalised also for error conditions in the calculation. In addition, the finalisation procedure closes the communicators, ends MPI if started by ATHLET and triggers finalisation of NuT. Runtime errors in that process have been prevented by refactoring ATHLET and by changes to NuT.

- In this context, the behaviour of the external control of ATHLET runs was changed. Previously, `KEXT == 709` was used to stop the run. This included the finalisation of ATHLET, to the extent implemented. That code was also returned upon leaving *atrans*, to signal that the end of the current integration period requested externally was reached. Now, `KEXT == 709` will never finalize ATHLET, resolving that rather unfortunate overloading of the control code. Instead `KEXT == 719` will have to be

called to finalize ATHLET, or `KEXT == 710` to combine both effects. The ATHLET python controller has been adapted accordingly.

- For allowing external controllers to restart an ATHLET calculation with changes in model dimensions, ATHLET uses the *libdfe* _REALLOCATE macros. In several instances, default Fortran allocation had been used, however, which would trigger either runtime errors or access violations in such a case. This has been changed to using _REALLOCATE or an equivalent method.

8.2 Documentation

The ATHLET program documentation package consisting of the User's Manual, Models and Methods Manual, Validation Manual, Programmer's Manual, and Program Updates Manual was updated for the release of the new program version ATHLET 3.5. Particularly the Programmer's Manual has been further extended with information for internal and external developers on ATHLET data structures and programming boundary conditions.

For the automatically generated documentation of the ATHLET source code, the description of the global variables has been supplemented or corrected where necessary. Parts of the manuals, which were previously edited using Microsoft Word, have been transferred to LaTeX. With code version ATHLET 3.5, the ATHLET User's Manual is completely generated from LaTeX sources. The transfer of the Models and Methods Manual into LaTeX is ongoing.

A collection of Python scripts was developed in the past to automatically generate the source code documentation in the Programmer's Manual including information about the module variables and the dependencies within the ATHLET source code, and to update the procedure headers in the source code itself, e.g. with information where these procedures are called. The generated documentation supports both code developers and (experienced) code users. These tools need regular maintenance work. In particular, the use of submodules, a more modern feature of Fortran which is now omnipresent in the ATHLET code, was not well supported so far by the documentation tools and led to many wrong entries in the output tables. This problem could be fixed. Furthermore, the formatting of the tables had to be improved in view of the change to LaTeX for typesetting the manuals.

Because of the maintenance work required for these tools, it was also evaluated whether they can be replaced by some standard tools of similar scope which are available commercially or as open-source projects. While these tools can do the general tasks like displaying call trees, the extraction of the information which is currently shown in the tables in the Programmer's manual would at least require large additional effort, if it is possible at all. Furthermore, a general problem is the limited support of the Fortran language by some of the strongest tools; for example, the powerful and popular open-source tool Doxygen does support Fortran to some extent, but it fails to read subroutines in submodules and is thus practically not useable with the ATHLET code. Another open-source tool, FORD (FORtran Documentation generator), specifically targets modern Fortran language and is known to have at least basic submodule support. This tool will be evaluated as well in the future. However, all these tools need a specific formatting of the documentation (in form of comments) of variables and subroutines in the source code and cannot immediately be applied to the ATHLET code. Thus, a transition to a different documentation generator would require again substantial manual work, or the development and testing of an own tool to adapt the formatting of the source code comments to the requirements. With the introduction of artificial intelligence tools into the GRS code development process, new options for code documentation will become available, and will be explored for ATHLET.

8.3 Continuous Integration

Activities related to continuous integration (CI) were primarily focused on the improvement and consolidation of an automated regression testing pipeline for ATHLET, hereafter referred to simply as the regression pipeline. The pipeline was developed and integrated within the same GitLab® development environment of ATHLET, making use of the CI capabilities provided by the GitLab® DevOps platform. The objective of these activities was to strengthen the reliability, traceability, and overall effectiveness of the code verification and validation process. For further details concerning the initial development of the regression testing pipeline, as well as previous maintenance and improvement activities, reference is made respectively to /DIN 23/.

With reference to the regression testing pipeline of ATHLET, the improvement and consolidation activities carried out during the year 2025 led to the following key accomplishments:

- Development of technical documentation for the regression pipeline: comprehensive technical documentation covering the scope and description of the regression testing pipeline, providing detailed guidance on pipeline structure, configuration options, and usage. As in the case of the regression testing pipeline configuration, the documentation is hosted within a dedicated GitLab® project and is systematically maintained.
- Development of features for the automatic verification of ATHLET restart capabilities: new pipeline features were enabled to automatically verify the correct functioning of ATHLET restart capabilities in simulations.
- Development of features to test executables in debug mode: the pipeline was extended to test, on user demand, executables built in debug mode, which had previously been supported and tested only when compiled in release mode.
- Development of features enabling MPI-based testing with NuT: enabling the execution of tests in an MPI environment using NuT /STE 25/ through the introduction of dedicated configuration variables. Further details are provided in the pipeline documentation introduced above.
- Extension of the regression testing report: the regression testing pipeline report can be extended to include structured documentation for the tests considered in the test matrix. This documentation is contingent upon the introduction of user-provided inputs and is intended to associate each test in the matrix with detailed information on the experimental facility, test setup and execution, as well as the ATHLET models and simulation capabilities involved. This approach is aimed at providing clearer guidance for validation activities, for example by distinguishing between unit-level and integral tests and by identifying the applied physical models (e.g. spray models, thermal radiation, valves, or thermo-mechanical modules).

In connection with the last item above, the matrix of test cases applied in conjunction with the regression testing pipeline for checking the regression of ATHLET was extended through the integration of new validation cases, comprising e.g. tests based on the COAL experiments /REP 24/. These cases already include useful information on how to document tests within the regression testing report, thereby serving as guidelines for pipeline users.

With regard to future developments of the regression testing pipeline, several improvements are proposed to further enhance the testing infrastructure. In particular, efforts should be directed toward:

- Optimization of the regression testing pipeline through the incorporation of increasingly advanced features made available by the GitLab® DevOps platform, together with a simplification and streamlining of the associated pipeline configuration. These activities are expected to improve maintainability, scalability, and overall efficiency of the CI workflow.
- Introduction of cross-platform comparison capabilities as a valuable extension of the regression testing framework; that is, the ability to compare trends obtained from executables built on different operating systems (e.g. Windows® versus Linux®), which would further strengthen the validation process by ensuring consistency and reproducibility of simulation results across platforms.

8.4 Quality Assurance and Build Tools

The CI pipeline of AC²/ATHLET has been updated to target the latest Docker® images that are based on Windows 2025 and Debian 11. In parallel, a series of maintenance tasks were carried out on the ATHLET code base: the build script was refined, the newly introduced VTK library, required for generation and output of 3D geometry data, was integrated, and the FDE and NuT libraries were updated to their latest development state. A comprehensive refactoring of ATHLET's source code and its components was performed to guarantee that the software runs correctly on current platforms, notably by eliminating the use of an executable stack (execstack).

Preparations for building ATHLET with Intel's ifx Fortran compiler have also been completed. This involved creating up-to-date CI Docker® images that contain the ifx compiler, adjusting the CMake® configuration files to accommodate ifx-specific options, and executing extensive tests with ifx. Issues encountered during testing were communicated to Intel support and are being resolved. Because ifx has not yet reached the desired level of stability, the AC² 2025 release builds continue to use an updated version of the ifort Intel Fortran compiler from oneAPI ® 2024.2.1 together with GCC 10 on Linux and Microsoft Visual Studio 2022 on Windows.

Finally, an automated process for generating the VTK library has been implemented. The new workflow produces the required build files and assembles the appropriate licenses, enabling seamless integration of VTK into both ATHLET and the AC² framework.

8.5 ATHLET Release Management

During the project period, several new program versions were finalized, extensively validated, generally released and distributed to program users with a valid AC² program license via the AC² User Area. Related program versions are the patches ATHLET 3.4.2 /SCH 24c/ and ATHLET 3.4.3 as well as the current program version ATHLET 3.5.0 (included in AC² 2025.0) /SCH 25c/. The future patch ATHLET 3.5.1 is currently under preparation and will be released in summer 2026.

8.5.1 Code Version ATHLET 3.5.0

The code version ATHLET 3.5.0 was released in December 2025 and included the following new and improved features:

New models and features in TFD module:

- Extended spacer grid model considering convective heat transfer enhancement downstream the spacer grid and droplet breakup in dispersed flow regime (see chap. 3.1 and 4.2)

- Dedicated friction loss correlations for TFOs coupled to a helically coiled heat exchanger HCO, applied on both sides inside curved tube and outside tube bundle

- New heat pipe module available, to be activated by PW `HEATPIPE` under CW `OBJECT`

- New model to calculate wall friction in the laminar and laminar-to-turbulent transition region. Further model options can be activated via new input parameter `ITRNS` under PW `FRICTION`.

- Limitation of bulk condensation rate (direct condensation model) at high void fraction and low liquid subcooling to avoid liquid superheat due to steam condensation

- For collapsed level calculation (ITML0=0 under PW MIXLEVEL): Print and plot data under keyword MIXLEVEL reduced to significant quantities

- Optional usage of centralized flow regime map module via parameter AA under CW MISCELLAN. Comes with new print/plot output data denoting the flow regime.

- 3D TFO data derived from input under CW TOPOLOGY and PW GEOMETRY. More detailed 3D data can be defined with new PW POSITION under CW OBJECT. The data can be used for a 3D graphical representation of the fluidic network (vtk plugin). The 3D data may be used by various models in future.

- New optional SW under CW TOPOLOGY for extended configuration control by switching on/off whole sets of PCs.

- New PW SSCFRIC under CW OBJECT: For priority chains with IPRI0>0 (i.e. adaptation of friction losses allowed), the adaptation of friction losses performed during the SSC can be individually controlled for single TFOs or junctions.

- Additional print and plot data for mass and energy balances:
  - mass balance per TDV (keyword TDVBAL)
  - energy loss per TFD system (under TFDGENERAL)
  - mass balance per NC gas component per TFD system (under TFDGENERAL/MCOMPBAL)

- Mass balance output under FLUIDBAL for coupled calculations with COCOSYS/CFD corrected. Mass flows into/out of an external coupling branch (ICOPLO>0) are added either to LEAKMASS, if coupled junction is discharge or coupling branch is not a TDV, or to TDVMASS, if coupling branch is TDV.

- In order to avoid a program stop, the mixture level simulation is terminated, if the mixture level passes a not-integrated junction (e.g. a closed valve).

- CW FORMLOSS: pressure loss correlation for cross flow through a pipe bundle added

- Zinc-Borate transport and deposition models expanded:

- Formation of mobile ZnB particles if Zn saturation concentration is exceeded
- ZnB particle deposition at spacer grids up to blockage of flow channel
- Deposition of ZnB on fuel rods and consideration of thermal resistance of ZnB layer for heat transfer calculation

- Unified calculation of onset of entrainment and entrainment fraction

New features in HECU module:

- New option to define a HCO that simulates a horizontally oriented plate located right above or below (or even within) a vertically oriented CV. The horizontal plate HCO always consists of a single HCV. A dedicated HTC correlation (Churchill) for natural convection heat transfer at bottom/top of a plate is employed (see chap. 4.1).

- HTC calculation under post-CHF conditions inside helical heat exchanger tubes uses Mc Eligot correlation; former implementation resulted in a program error if post-CHF heat transfer was reached.

- Print/plot output of `MODEL/R` corrected for heat transfer regime 21 (subcooled nucleate boiling)

- Extended radiation model enables radiation heat transfer between HCOs connected to different TFOs. Corresponding groups of radiation bodies can be defined under new KW `FLEXRAD`. The geometry and nodalization of the HCOs must meet certain requirements.

- 3D data for HCO derived from geometry input of HCO and connected TFO. Can be used for 3D graphical representation.

- Optional 2D/3D solution of heat conduction for HCOs, can be activated via CW `HCOCONNECT`. Also enables heat conduction calculation between HCOs. If activated, NuT is used for the solution of the heat conduction equation system.

- Each HCO may consist of more than three material zones.

- Additional built-in materials with specific properties data available: BORCARBIDE, INCONEL600, ALUMINA

- For a HCO with TFOs coupled on both sides (e.g. heat exchanger HCO) the mutual assignment of HCVs and CVs has been improved to facilitate input data definition.

- Additional print/plot output for an HCO, whose surfaces (left and/or right) are coupled to a TFO with mixture level. For each mixture level, heat flows, HTC and other quantities related to the sub-CV above the ML are printed under the new keyword ML_LEFT or ML_RIGHT.

- Calculation of thermal conductivity for liquid metal working fluids in Forster-Zuber HTC correlation corrected

  - Thermal resistance of oxide layer (see PW ZROXIDAT) is considered for calculation of wall-to-fluid heat transfer. Currently, the heat conductivity of zirconium oxide is used, independent of the cladding material selected by parameter MODOXI. Note: This program modification also affects existing input data sets that model an initial oxide layer via PW ZROXIDAT, parameter ZROX0.

New feature in neutron kinetic module:

- Average temperature TRHOEXP of CVs (or HCVs) for calculation of thermal expansion feedbacks provided as output quantity. Only CVs (HCVs) with a form factor greater than zero are considered.

New feature concerning numerical solver:

- Numerical Toolkit version increased to NuT 2.1.0 (for details see NuT documentation)

  - Enables local use of NuT; however, use of NuT worker (separate process) is still possible

  - By default, computation of 3D heat conduction in structures (CW HCOCONNECT) and inventory calculation by VENTINA make use of NuT's local interface and dedicated algorithms.

- Modified effective local error bound derived from the absolute and relative error bounds

Improved component models:

- Critical discharge model CDR1D: new option via `IAUR`=+/-5 to consider phase drift in evaporation and condensation model. Activation of extended CDR1D model changes meaning of input parameters `TURB` and `CMUEK`.

GCSM

- Additional input check for `FUNGEN` controller without `X2NAME` specified: `IOPT` must be -2 or 0 (other options for `IOPT` cause a program stop)
- Re-ordering of GCSM process signals during input processing to increase code efficiency

Plugins:

- Extension of the plugin MTHCEXT_CONVECTION to film boiling heat transfer regime with convective heat transfer to vapor
- Interfaces in MHTCEXT plugin updated
- MASL plugin provides additional options to control stationary MASL and thermal margin
- New plugin vtk for output of 3D TFO and HCO data using the format vtk (for visualization e.g. with ParaView)
- Plugins for CHF calculation, MHCHFEXT and MHCHFEXT_EXTERNAL_FLUID: index of inlet CV of core channel added to parameter list. This facilitates the access to core entrance flow conditions to be used in the user-provided CHF correlation.
- Update preCICE adapter to current preCICE version 3

General code updates:

- FMU controller to couple ATHLET with MODELICA-based models

- New output quantities under keyword MONITOR:
    a. IJLIM: time step size limiting CV or junction
    b. IJRED: time step size reducing CV or junction
- ATHLET internal time variables transferred to real(16); output format is still real(8)
- New sample sample1_vtk.in including 3D TFO data
- Input under CW COCOSYS, PW COUPLING changed: a user-defined name ACPLNAM for print and plot output has been added and S0INP has been removed.
- Some models originating from ATHLET-CD have been integrated in ATHLET:
    - VENTINA for initial inventory calculation and decay of isotopes
    - FPREL and SAFT for release, transport and deposition of radionuclides in LWR
    - THEMEC for fuel rod behavior, ballooning, and feedback on thermal-hydraulics (blockage)
- The output file named <input-name>*_EXP* is saved in the working directory instead of the input directory.
- Output file <problem-id>*.minmax* including minimum and maximum values of plot variables removed.
- HCO nodalization data (N10 etc.) written to gr-file (used e.g. by batchplot).
- New optional input data check to detect unused parameters; check can be activated by new PW IDLE_PARAM under CW SERVICES.
- Additional output quantity for mass residuum per CV
- All subroutines have been put into submodules with interface declaration to enable additional compiler checks for consistency.

Software tool updates:

- Batchplot extended to visualize 2D SVG images generated by AIG-2.
- The output format of the key file was modified so that very large systems with many output quantities can be properly handled.

8.5.2 User Area and Code Transfer

The released ATHLET program versions were distributed to all users with a valid program license via the AC² user area. Since the release of ATHLET 3.4.2 (AC²-2023.3) in autumn 2024, the program has been distributed to almost 25 organizations. ATHLET 3.5.0 (AC²-2025) has been distributed to around 10 organizations since its external release in January 2026.

The main purpose of the user area is to facilitate the communication between the AC² development team and external code users. In addition to access-restricted sites for code transfer or file exchange, it also offers discussion forums for exchanging user experiences. The user area has been continuously maintained.

9 Conclusion and Outlook

The AC² program package, consisting of the system codes ATHLET, ATHLET-CD and COCOSYS and complemented by further tools such as the ATLAS simulator software, is being developed, validated, and distributed by GRS for the investigation of current topics in reactor safety research and for reactor safety analyses. AC² can be used to analyze states of normal and abnormal operation, incidents and accidents anticipated for reactor plants and other nuclear facilities.

The main subject of the project at hand, which is the second phase of RS1600 /SCH 24a/, was the improvement of the thermal-hydraulic system code ATHLET in order to keep pace with the state of science and technology, and to enable the user community to perform safety analysis for existing and future nuclear reactors in accordance with the latest state of knowledge. To this end, firstly the code's functionality was extended to cope with the increasing modelling demands of existing reactors, innovative light water reactor designs and SMRs. Furthermore, to achieve targeted and efficient code development in accordance with the user needs, sharing of experience with all program users as well as common code developments with national partners were successfully intensified, and the cooperation in international working groups like the FONESYS network or the OECD/NEA RBHT project was strengthened. Measurements related to quality assurance of the program development were expanded and a new, comprehensively validated ATHLET code version 3.5.0 was released and distributed to the program users.

The following outlines the key objectives and outcomes of the project.

Flow regime map for post-CHF conditions

The central FLRM module had already been implemented in the frame of project phase A in RS1600. This implementation allows for the flexible addition of further application-specific flow regime maps. Taking advantage of this functionality, a dedicated flow regime map for post-CHF conditions (characterized by wall temperatures above the minimum film boiling temperature) was implemented. The map is based on established approaches from the literature and, in addition to droplet flow, also accounts for the flow patterns of inverted slug flow and inverted annular flow, which are new in ATHLET. For these two flow patterns, new closure laws were implemented so that interfacial friction and wall friction under film boiling flow conditions are captured more realistically.

The expanded FLRM module was validated against CHF and reflooding experiments from COSMOS and RBHT facilities. Promising results could be found for some of the applications, although further consolidation of the implementation is necessary, e.g. regarding the numerical performance of the model. This work is intended to be performed in a follow-up project. In general, the new implementation enables the mechanistic modeling of post-CHF conditions with ATHLET, thereby reducing previously observed uncertainties e.g. with regard to the phase distribution in the core or the predicted cladding temperatures.

The use of a dedicated flow regime map for post-CHF conditions reflects the current state-of-the-art of system code modelling, so that the extension of the FLRM contributes to maintaining ATHLET internationally competitive. In addition, it offers significant potential for future program improvements, as it makes detailed flow pattern maps accessible to all program parts. For example, the bulk evaporation model, which has so far considered a reduced and very simplified flow pattern map, could make use of the information from the new module. Heat transfer between the wall and the fluid can also be simulated more realistically using the FLRM module by assigning the heat flux for flow patterns with clear phase separation to that phase, which is in contact with the wall. For the flow patterns of annular flow and stratified flow, a modeling approach was developed that considered the distribution of heat flows from a more mechanistic perspective, thereby offering reduced uncertainties in the calculation of phase temperatures. The approach could be successfully verified against the COSMEA experiment that investigated condensation phenomena in a slightly inclined pipe. This development is of particular interest to the assessment of passive safety systems, which are primarily used by advanced reactor designs and SMRs.

Modelling of spacer grids

Based on observations that ATHLET sometimes calculates too high cladding temperatures during reflood above the swell level, the spacer grid model has been expanded. The presence of spacer grids along the entire rod bundle has various impacts on the thermal-hydraulic behavior in the reactor core. Due to the induced turbulent mixing, convective heat transfer rate increases significantly downstream of a spacer grid. In addition, the droplets entrained in the vapor phase in the DFFB regime break up into much smaller ones when impinging on the spacer grid, leading to significantly increased interfacial heat and mass transfer and, as a result, further enhancement of the clad cooling capability due to vapor de-superheating through droplet evaporation and flow acceleration.

The accurate prediction of these thermal-hydraulic effects is of particular interest, as PCT typically occurs in the upper core region under DFFB conditions. Consequently, new models have been implemented in ATHLET that adequately take these effects into account. The spacer grid model was validated using data from the RBHT experiment, which include detailed measurements of the conditions upstream and downstream of the spacer grids. In particular, the new modelling yielded significantly improved results regarding the conditions immediately downstream of the spacers. On the one hand, the calculated cladding temperatures agree more accurately, both qualitatively and quantitatively, with the experimental values. On the other hand, the vapor temperature is also simulated more realistically, which is mainly a consequence of the simulated droplet breakup and its influence on the interfacial transfer. Further improvement of the ATHLET spacer grid model is planned within an intended follow-up project e.g. to consider more accurately the influence of the flow pattern.

Thermo-mechanical simulation of structures

To precisely simulate structures of specific geometry such as horizontal components within huge vessels like the RPV or horizontal bottom of water pools of passive systems, the ATHLET heat conduction module HECU has been expanded to include the new structural type named ‘horizontal plate’. This enables users to model such geometries more realistically in ATHLET and to calculate heat transfer to the fluid above and below the structure with greater accuracy. Special heat transfer correlations for cooling or heating conditions have been implemented for both the bottom side and the top side of the horizontal structure. For example, this enables to account for heat transfer across the lower core plate between the core region and the lower plenum during a severe accident.

Thermal-hydraulic modelling

Concerning thermal-hydraulic modelling of complex flow phenomena, the CDR1D model of ATHLET used for the calculation of critical discharge rates of leaks has been improved and extended by a model that accounts for the phases’ relative velocity. This enhancement yields improved results against experimental data of the Super Moby Dick experiment, particularly under conditions close to saturation, when significant evaporation and two-phase flow acceleration occur in the outflow region. The model is currently available as an optional feature selectable in the input data set and may become the default approach in future, if more comprehensive validation results are available to enable a final model assessment.

Furthermore, a dedicated correlation simulating flow losses for cross flows through tube bundles has been implemented in ATHLET. The correlation is also applied to the outer side of structures representing the tubes of a helically coiled heat exchanger, making the calculation of pressure drop more realistically. Also advantageous for simulating helical heat exchangers is the improvement of the program section responsible for the automatic nodalization of HCOs that are inclined relative to the surrounding fluid (such as inclined tube bundles in a vertical channel), simplifying the specification of such geometrical configurations in the input data set. Further improvements implemented in the frame of UMRS1615, particularly with regard to enhanced numerical performance, were related to the simulation of injection systems with subcooled fluid and the simulation of non-condensable gases.

International cooperation

In the frame of the international FONESYS network, GRS is cooperating with organizations that are developing internationally applied system codes such as CATHARE, SPACE, APROS or LOCUST. Biannual meetings were held for exchanging information, subjecting current developments to critical reviews, and conducting several joint code-to-code benchmarks.

The Core-3D-Mixing benchmark investigated the dependence of cross flows in a bundle geometry with spacer grids on the pressure level for both single-phase vapor and two-phase inlet flow conditions. All codes that participated in the benchmark predicted vapor friction-driven crossflows (from high-power to low-power assembly) at low pressure and buoyancy-driven crossflows (from low-power to high-power assembly) at high pressure in the vapor region above the swell level in the bundle. The homogenization of void fraction below the swell level was similarly predicted by all codes, so that equal swell levels established in the simulated hot and cold assemblies. Generally, the spacer grid form losses supported a flow homogenization between the assemblies. Significant differences between the codes were found for the wall to vapor convection heat transfer HTC, causing remarkable differences in the rod surface temperatures.

Another FONESYS benchmark activity was related to the investigation of the scalability of interfacial friction models for bundle geometry used in current system codes. Main findings of the performed analysis were that significant uncertainties of the interfacial friction exist for low pressure conditions. In addition, the various interfacial friction models used by the codes exhibit different scaling properties with regard to the dependency on

the hydraulic diameter. Accompanying the benchmark activity, ATHLET was validated against the SIRIUS-3D bundle evaporation experiment. Good agreement of void fraction distribution at high pressure proves the maturity of the ATHLET interfacial friction model for such conditions. However, worse results at low pressure of about 10 bar confirm the above-mentioned benchmark finding of large deviations between the different codes for these conditions and indicate the need for code improvement that is intended to be addressed by a follow-up project to UMRS1615.

GRS also participated in the OECD/NEA Rod-Bundle Heat-Transfer Project (RBHT-II). Open and blind calculations were carried out on 7x7 rod bundle experiments from the RBHT test facility operated at Penn State University. The experimental data served to validate ATHLET, with a focus on those models that are of particular importance for the simulation of the flooding of the reactor core after a LOCA. Phase II of the project focused on low flooding rates, which proved to be most challenging for the codes during the first RBHT project phase. Overall, ATHLET was able to reproduce the maximum cladding temperatures very well. However, the timing of rewetting was frequently calculated too early. This appears to be caused by the heat transfer coefficients calculated too high in the film boiling regime above the quench front, as well as by the calculated progression speed of the quench front. Interestingly, large uncertainties for the wall to vapor convection heat transfer were also found by the FONESYS Core-3D-Mixing benchmark, which highlights the need for future improvement of this model.

User support and user friendliness

Another key focus of the project was put on continuously enhancing the usability of ATHLET and strengthening the modelling basis according to the demands of new applications. These developments often resulted from the frequent exchange with the numerous ATHLET users. For instance, the AC² User Meeting, regularly held every two years and organized in GRS Cologne in 2025, provided valuable insight into users' preferences for model extensions as well as into model gaps or weaknesses. Based on these user experiences, several models and methods used in ATHLET were improved. For example, a new approach to automatically adjust initial pressure losses to achieve an initially consistent system state was implemented, mainly to be used for system areas where knowledge on flow losses is incomplete und insecure. Additional input data error checks and extended program outputs were also added to make the code more robust against input data errors and to provide the user with comprehensive information. E.g., additional output parameters related to integral mass and energy balances were implemented to

assist users in evaluating their analyses. Furthermore, the pre- and post-processing tools distributed together with ATHLET were continuously improved. Concerning the plotting tool Batchplot, several new options were added to generate temporal evolution plots and axial or radial distribution plots. Batchplot makes use of the HDF5 plot data file, which has been supplemented with additional data on the geometry of the simulated system and with the units of the printed output quantities. AIG and GIG have also been updated with new features, including the availability of AIG for Linux operating systems. All these developments ensure that ATHLET can be applied more flexibly to different and new applications.

Release management

The main objective of the project was to provide the numerous ATHLET users with extended, quality-assured program versions that allow for investigations of current safety-related issues in existing facilities and new reactor designs. For that purpose, the code version ATHLET 3.5 was released and distributed during the project period. The new code version contains a significant number of new models and improved features, which were subjected to comprehensive quality assurance procedures before their integration into the main development branch of ATHLET. Many of the models developed within both UMRS1615 and its previous project phase RS1600 have been made available to all users with the recent ATHLET 3.5 code release.

Concluding remarks

Overall, the main objectives of phase B of the project with regard to model development, quality assurance, and national and international cooperation have been successfully achieved. This is reflected in the release of the current code version ATHLET 3.5 that includes numerous new and improved models and features. Still, the development of ATHLET needs to be continued to meet newly arising requirements from the program application necessary for the analysis of current, advanced and innovative reactor designs. Some of the work initiated during the project will be continued in future. For instance, GRS intends to further develop and consolidate the central flow regime map module and related closure laws in the frame of a follow-up project. In addition, GRS participation in international activities like the OECD RBHT project or the FONESYS network is ongoing. Furthermore, the work related to user support, code maintenance, and release management will be carried out continuously. This is of particular importance

since numerous projects, including those funded by BMUKN, are related to aspects of ATHLET development or application.

Nowadays, ATHLET is a versatile and reliable tool for analyzing thermal-hydraulic processes in nuclear power plants and research reactors. A distinctive feature of the code is its usage within numerous national and international projects and activities. Consequently, ATHLET stands for an active contribution to maintaining competence in the field of nuclear technology. ATHLET contains a comprehensive knowledge base on safety-relevant phenomena in nuclear reactors, including their modelling and assessment in the context of reactor safety analyses. The code serves as both a basis and starting point for numerous research activities as well as a software tool for training and educating young scientists. This is best demonstrated by model developments performed at German research institutions and universities, which were recently integrated in the main version of ATHLET to become available for all code users. These models improved the code's predictive ability particularly regarding advanced reactor designs and SMRs, which may potentially be constructed in the vicinity of Germany in future. This highlights how the continuous development and maintenance of ATHLET contributes to maintaining and enlarging the knowledge on reactor safety in Germany. Finally, this also supports GRS to reliably inform and advise the federal German government on current and future topics related to nuclear installations safety both domestically and abroad.

Literature

/ABD 25/ Abd El Malek, M.: Improvement of the friction factor model in the laminar and transition-to-turbulent range in ATHLET, Technical Report. IKE, University of Stuttgart, IKE, 2-FB25-1, 2025.

/AHN 15/ Ahn, S. H., Aksan, N., Austregesilo, H., Bestion, D., Chung, B. D., D'Auria, F., Emonot, P., Gandrille, J. L., Hanninen, M., Horvatović, I., Kim, K. D., Kovtonyuk, A., Petruzzi, A.: FONESYS: The FOrum & NEtwork of SYStem Thermal-Hydraulic Codes in Nuclear Reactor Thermal-Hydraulics. Nuclear Engineering and Design, Bd. 281, S. 103–113, DOI 10.1016/j.nucengdes.2014.12.001, 2015.

/ARA 22/ Arai, T., Furuya, M., Shirakawa, K.: Development of Subchannel Void Sensor for Wide Pressure and Temperature Ranges and Its Application to Boiling Flow Dynamics in a Heated Rod Bundle. Nuclear Technology, Bd. 208, Nr. 2, S. 203–221, DOI 10.1080/00295450.2021.1897733, 2022.

/BES 18/ Bestion, D., Valette, M., Fillion, P., Gaillard, P.: 3d core thermalhydraulic phenomena in pwr sblocas and iblocas. In: American Nuclear Society (ANS), Zhongguo-Hexuehui, Xi an jiao tong da xue: 17th International Topical Meeting on Nuclear Reactor Thermal Hydraulics (NURETH-17). NURETH-17, Xi'an, China, 3. - 8. September 2017, ISBN 9781510872622, Curran Associates Inc: Red Hook, NY, 2018.

/BES 23/ Bestion, D., D'Auria, F., Cai, Q.: BENCHMARK OF 3D CORE AND SUBCHANNEL MODELS IN A SIMPLE 1-PHASE FLOW. 2023.

/BES 25a/ Bestion, D., D'Auria, F., Umminger, K., Heo, J., Schöffel, P. J., Carnevali, S., Vacher, J. L., Gaillard, P., Sha, H., Yuan, H., Waddington, G., LeCorre, J. M.: Current and Planned Activities of the FONESYS Network of System Code Developers in collaboration with the SILENCE Network of Experimentalists. In: American Nuclear Society (ANS) (Hrsg.): 21st International Topical Meeting on Nuclear Reactor Thermal Hydraulics. Korean Nuclear Society (KNS), NURETH-21, Busan, Korea, 31. August - 5. September 2025, August 2025/September 2025.

/BES 25b/ Bestion, D., D'Auria, F., Cai, Q., Heo, J., Schöffel, P. J., Yuan, H., Capogna, A., Carnevali, S.: FONESYS Benchmark of Core Interfacial Friction Models in System Codes. In: American Nuclear Society (ANS) (Hrsg.): 21st International Topical Meeting on Nuclear Reactor Thermal Hydraulics. Korean Nuclear Society (KNS), NURETH-21, Busan, Korea, 31. August - 5. September 2025, August 2025/September 2025.

/BES 25c/ Bestion, D., Schöffel, P. J., Piette, N., Vacher, J. L., Jeong, J. J., Heo, J., D'Auria, F., Cai, Q., Zingales, V.: FONESYS Benchmark of singular Pressure Losses in System codes. In: American Nuclear Society (ANS) (Hrsg.): 21st International Topical Meeting on Nuclear Reactor Thermal Hydraulics. Korean Nuclear Society (KNS), NURETH-21, Busan, Korea, 31. August - 5. September 2025, August 2025/September 2025.

/BIE 20/ Bieberle, A., Moonesi Shabestary, A., Geissler, T., Boden, S., Beyer, M., Hampel, U.: Flow morphology and heat transfer analysis during high-pressure steam condensation in an inclined tube part I: Experimental investigations. Nuclear Engineering and Design, Bd. 361, S. 110553, DOI 10.1016/j.nucengdes.2020.110553, 2020.

/BOD 24/ Boden, S., Hampel, U., Pietruske, H., Bieberle, A.: Investigation on flow morphology and heat transfer for high-pressure steam condensation in an inclined tube at low inlet steam qualities. Nuclear Engineering and Design, Bd. 419, S. 112954, DOI 10.1016/j.nucengdes.2024.112954, 2024.

/CAC 96/ Cachard, F. de: Development, Implementation, and Assessment of Specific Closure Laws of Inverted-Annular Film-Boiling in a Two-Fluid Model. NUREG/IA-, Nr. 0133, 104 S., 1996.

/CRO 12/ Cron, D. von der: Entwicklung eines ATHLET-Sprühkondensationsmodells, TN-VDC-12/01. Technische Notiz, TN-VDC-12/01, 2012.

/CRO 23/ Cron, D. von der: Konzept für das Überblenden von Strömungsbildkarten in ATHLET, TN-VDC-23/01. Technische Notiz, TN-VDC-23/01, 16 S., Dezember 2023.

/DIN 23/ Di Nora, V. A., Wielenberg, A., Hollands, T.: Implementation & application of a GitLab CI pipeline for AC2 validation. In: Žagar, T., Lenošek Kavčič, M. (Hrsg.): 32nd International Conference Nuclear Energy for New Europe, Book of Abstracts. Društvo Jedrskih Strokovnjakov Slovenije, NENE 2023, Portorož, Slovenia, 11. - 14. September 2023, S. 206, ISBN 978-961-6207-55-3, 2023.

/DIT 30/ Dittus, F. W., Boelter, L. M. K.: Heat transfer in automobile radiators of the tubular type. University of California publications in engineering, Vol. 2, No. 13, University of California press: Berkeley, Oktober 1930.

/DÜN 22a/ Dünne, N., Skorek, T., Schöffel, P. J.: Simulation of the open tests of the RBHT benchmark with ATHLET. In: American Nuclear Society (ANS) (Hrsg.): 19th International Topical Meeting on Nuclear Reactor Thermal Hydraulics (NURETH-19). NURETH-19, Brussels, Belgium (virtual), 6. - 11. März 2022, ISBN 9789076971261, 2022.

/DÜN 22b/ Dünne, N., Skorek, T., Schöffel, P. J.: Simulation and uncertainty analysis of the RBHT blind tests with ATHLET 3.3. In: Chung-Hwa Nuclear Society (CHNS), National Tsing Hua University (Hrsg.): NUTHOS-13 2022 Proceeding Book, 13th International Topical Meeting on Nuclear Reactor Thermal-Hydraulics, Operation and Safety. NUTHOS-13, Hsinchu, Taiwan, 5. - 10. September 2022, 2022.

/DÜN 25a/ Dünne, N.: ATHLET 3.5 simulation results of the RBHT II open phase tests. OECD/NEA RBHT II Project: 4th Workshop and Meeting of the Management Board, Virtual, Dezember 2025.

/DÜN 25b/ Dünne, N.: ATHLET simulation results of the RBHT II open phase tests. OECD/NEA RBHT II Project: 3rd Workshop and Meeting of the Management Board, Paris Saclay, Juni 2025.

/DÜN 26/ Dünne, N.: ATHLET 3.5 simulations of the RBHT II blind phase tests. OECD/NEA RBHT II Project: 5th Project and Management Board Meeting, Aix-en-Provence, März 2026.

/FU 19/ Fu, Q., Bestion, D., Fillion, P., Davit, Y., Quintard, M.: Analysis of flow in rod bundles with velocity and temperature radial dissymmetry using CATHARE-3. In: ICAPP 2019. 2019.

/HAA 12/ Haas, C.: Critical Heat Flux for Flow Boiling of Water at Low Pressure on Smooth and Micro-Structured Zircaloy Tube Surfaces, Zugl.: Karlsruhe, Karlsruher Inst. für Technologie, Diss., 2012. Karlsruhe Institute of Technology (KIT), KIT Scientific Reports, Bd. 7627, 186 S., ISBN 978-3-86644-923-7, DOI 10.5445/KSP/1000030425, KIT Scientific Publishing; Technische Informationsbibliothek u. Universitätsbibliothek: Hannover, Karlsruhe, 2012.

/HOL 08/ Holloway, M. V., Beasley, D. E., Conner, M. E.: Single-phase convective heat transfer in rod bundles. Nuclear Engineering and Design, Bd. 238, Nr. 4, S. 848–858, DOI 10.1016/j.nucengdes.2007.08.003, 2008.

/INL 12/ Idaho National Laboratory (INL): RELAP5-3D Code Manual Volume IV: Models and Correlations. INEEL-EXT-98-00834, 2012.

/ITO 59/ Ito, H.: Friction Factors for Turbulent Flow in curved pipes. Journal of Basic Engineering, S. 123–132, 1959.

/JOB 24/ Jobst, M., Schäfer, F., Kliem, S.: Numerical investigation on steam condensation and heat transfer in an emergency condenser tube with the thermo-hydraulic system code ATHLET. Nuclear Engineering and Design, Bd. 421, S. 113059, DOI 10.1016/j.nucengdes.2024.113059, 2024.

/KIM 14/ Kim, M.-G., Lee, Y., Lee, J. I.: Flow regime comparison of MARS-KS to SPACE during LBLOCA. Transactions of the Korean Nuclear Society Autumn Meeting, 2014.

/KRI 24/ Krieger, J., Koch, M. K.: Analysis of a Selected Experiment of the OSU-MASLWR Test Facility Regarding Heat Transfer in Helically Coiled Steam Generators Using AC 2 -ATHLET. Nuclear Technology, S. 1–14, DOI 10.1080/00295450.2024.2377027, 2024.

/LIU 21/ Liu, Q., Kelly, J., Sun, X.: Study on interfacial friction in the inverted annular film boiling regime. Nuclear Engineering and Design, Bd. 375, S. 111082, DOI 10.1016/j.nucengdes.2021.111082, 2021.

/MOE 70/ Moeck, E. O.: Annular-dispersed two-phase flow and critical heat flux. Atomic Energy of Canada Limited (AECL), AECL-, Nr. 3656: Chalk River, ON, Canada, 1970.

/NAR 82/ Nariai, H., Kobayashi, M., Matsuoka, T.: Friction Pressure Drop and Heat Transfer Coefficient of Two-Phase Flow in Helically Coiled Tube Once-Through Steam Generator for Integrated Type Marine Water Reactor. Journal of Nuclear Science and Technology, Bd. 19, Nr. 11, S. 936–947, DOI 10.1080/18811248.1982.9734239, 1982.

/NRC 12/ U.S. Nuclear Regulatory Commission (NRC): TRACE V5.0 Theory Manual. 2012.

/OEC 25/ OECD Nuclear Energy Agency: Rod Bundle Heat Transfer (RBHT) Project Phase I Summary Report. Nuclear Safety NEA/CSNI, NEA/CSNI/R(2023)7, 45 S., 2025.

/REP 24/ Repetto, G., Grando, Q., Eymery, S., van Lochem, R.: COAL reflooding experiments during a loss of coolant Accident: Effect of the water flow rate, the pressure and the rod power with ballooned rods. Nuclear Engineering and Design, Bd. 429, S. 113641, DOI 10.1016/j.nucengdes.2024.113641, 2024.

/SAL 20/ Salko, R., Avramova, M., Wysocki, A., Hu, J., Toptan, A., Porter, N., Blyth, T. S., Dances, C. A., Gomez, A., Jernigan, C., Kelly, J.: CTF User's Manual, Version 4.2. 14. September 2020.

/SCH 15/ Schöffel, P. J., Ceuca, S. C., Deitenbeck, H., Kloos, M., Langenfeld, A., Lerchl, G., Peschke, J., Scheuer, J., Skorek, T., Cron, D. von der, Weyermann, F. C.: Weiterentwicklung des Systemrechenprogramms ATHLET für Anwendungen in der Reaktorsicherheit. Gesellschaft für Anlagen- und Reaktorsicherheit (GRS) gGmbH (GRS), GRS-Bericht, GRS-387, September 2015.

/SCH 18/ Schöffel, P. J., Herb, J., Langenfeld, A., Lerchl, G., Skorek, T., Cron, D. von der: Rechenmethodenentwicklung für Reaktorsicherheitsanalysen mit dem Systemcode ATHLET. GRS-Bericht, GRS-497, 252 S., ISBN 978-3-946607-82-3, Gesellschaft für Anlagen- und Reaktorsicherheit (GRS) gGmbH: Köln, November 2018.

/SCH 21/ Schöffel, P. J., Buchholz, S., Dünne, N., Guo, L., Jacht, V., Köllein, C., Krüssenberg, A., Lee, J., Lerchl, G., Skorek, T., Cron, D. von der, Weyermann, F. C., Wielenberg, A., Wong, K. W.: Weiterentwicklung des AC² Thermohydraulik-Moduls ATHLET zur Simulation komplexer, zweiphasiger Strömungsphänomene. Gesellschaft für Anlagen- und Reaktorsicherheit (GRS) gGmbH (GRS), GRS-Bericht, GRS-630, ISBN 978-3-949088-19-3, 2021.

/SCH 24a/ Schöffel, P. J., Di Nora, V. A., Dünne, N., Jacht, V., Junk, M., Skorek, T., von der Cron, D., Weyermann, F. C., Wielenberg, A.: Further Development of the AC² Code ATHLET for Evolutionary Reactors and Research Reactors (Phase A). Gesellschaft für Anlagen- und Reaktorsicherheit (GRS) gGmbH (GRS), GRS-Bericht, GRS-795: Köln, August 2024.

/SCH 24b/ Schöffel, P. J., Di Nora, V. A., Eckert, D., Junk, M., Cron, D. von der, Weyermann, F. C., Wielenberg, A.: ATHLET 3.4.1 Models and Methods. Gesellschaft für Anlagen- und Reaktorsicherheit (GRS) gGmbH (GRS), GRS-P-1/Vol. 4 Rev. 9, Mai 2024.

/SCH 24c/ Schöffel, P. J., Di Nora, V. A., Eckert, D., Junk, M., Cron, D. von der, Weyermann, F. C., Wielenberg, A.: ATHLET 3.4.2 Models and Methods. Gesellschaft für Anlagen- und Reaktorsicherheit (GRS) gGmbH (GRS), GRS-P-1/Vol. 4 Rev. 10, Oktober 2024.

/SCH 25a/ Schöffel, P.: New Models and Features in ATHLET 3.5. Präsentation, Gesellschaft für Anlagen- und Reaktorsicherheit (GRS) gGmbH (GRS), AC² User Meeting 2025: Cologne, Germany, 18. November 2025.

/SCH 25b/ Schöffel, P. J., Bestion, D., Rodriguez, A., Prea, R., Heo, J., Sha, H., Wang, L., Yuan, H., D'Auria, F., Zingales, V.: FONESYS benchmark of Core-3D-Mixing in system codes. In: American Nuclear Society (ANS) (Hrsg.): 21st International Topical Meeting on Nuclear Reactor Thermal Hydraulics. Korean Nuclear Society (KNS), NURETH-21, Busan, Korea, 31. August - 5. September 2025, August 2025/September 2025.

/SCH 25c/ Schöffel, P. J., Di Nora, V. A., Eckert, D., Junk, M., Cron, D. von der, Weyermann, F. C., Wielenberg, A.: ATHLET 3.5 User Manual. GRS-P-1/Vol 1 Rev. 14, 2025.

/STE 25/ Steinhoff, T., Jacht, V.: NuT 2.1 Numerical Toolkit User's Manual. GRS-P-10 / Vol. 1 Rev. 9, Dezember 2025.

/SUD 93/ Sudo, Y., Kaminaga, M.: A New CHF Correlation Scheme Proposed for Vertical Rectangular Channels Heated From Both Sides in Nuclear Research Reactors. Journal of Heat Transfer, Bd. 115, Nr. 2, S. 426–434, DOI 10.1115/1.2910695, 1993.

/SUG 84/ Sugimoto, J., Murao, Y.: Effect of Grid Spacers on Reflood Heat Transfer in PWR-LOCA. Journal of Nuclear Science and Technology, Bd. 21, Nr. 2, S. 103–114, DOI 10.1080/18811248.1984.9731021, 1984.

/VAL 26/ Valgrind Development Team: Valgrind Web page. Erreichbar unter https://www.valgrind.org/, abgerufen am 2. Februar 2026.

/VDI 13/ Verein Deutscher Ingenieure (VDI), VDI-Gesellschaft Verfahrenstechnik und Chemieingenieurwesen (GVC): VDI-Wärmeatlas, Mit 320 Tabellen. VDI-Buch, 11. Aufl., 1760 S., ISBN 978-3-642-19981-3, DOI 10.1007/978-3-642-19981-3, Springer Vieweg: Berlin, 2013.

/WAL 70/ Wallis, G. B.: Annular Two-Phase Flow, Part 1: A Simple Theory. Journal of Basic Engineering, Nr. 59, 1970.

/WEB 93/ Weber, J. P., Skorek, T., Teschendorff, V.: ATHLET-Verifikation an HDR-Kondensationsversuchen und Druckhalterversuchen der TH Zittau. GRS-A-Bericht, GRS-A-2062, Juni 1993.

/YAO 82/ Yao, S. C., Hochreiter, L. E., Leech, W. J.: Heat-Transfer Augmentation in Rod Bundles Near Grid Spacers. Journal of Heat Transfer, Bd. 104, Nr. 1, S. 76–81, DOI 10.1115/1.3245071, 1982.

/YAO 88/ Yao, S. C., Hochreiter, L., Cai, K. Y.: Dynamics of Droplets Impacting on Thin Heated Strips. Journal of Heat Transfer, Bd. 110, S. 214–220, 1988.

List of Figures

Fig. 2.1 Flow regime map for post-CHF conditions in vertical flow paths of TRACE /NRC 12/. $\mathbf{E}$ stands for the entrained droplet fraction. 5

Fig. 2.2 Flow regime map for vertical flow paths of RELAP5-3D /INL 12/. The post-CHF flow regimes are within the area framed by the green dashed line. 6

Fig. 2.3 Flow regime map for post-CHF conditions in vertical flow paths of SPACE (own work, based on /KIM 14/) 6

Fig. 2.4 Decision tree for the implemented post-CHF flow regime map for vertical channels 8

Fig. 2.5 Graphical representation of the post-CHF flow regime map for vertical channels as implemented in ATHLET 8

Fig. 2.6 A fluiddynamic CV (blue) which is in contact with four different HCOs 9

Fig. 2.7 COSMOS test LA-120-80-0250: Number of time steps needed with active and inactive flow regime map module 16

Fig. 2.8 COSMOS test LA-120-80-0250: Number of Jacobian matrix updates needed with active and inactive flow regime map module 16

Fig. 2.9 COSMOS test LA-120-80-0250: Residual mass with active and inactive flow regime map module 17

Fig. 2.10 COSMOS test LA-120-80-0250: Liquid mass inventory calculated with active and inactive flow regime map module 17

Fig. 2.11 RBHT facility nodalization 19

Fig. 2.12 Measured and simulated cladding temperature for test O3 20

Fig. 2.13 Measured and simulated cladding temperature for test O4 20

Fig. 2.14 Measured and simulated quench front progression for test O3 21

Fig. 2.15 Measured and simulated quench front progression for test O4 21

Fig. 2.16 Measured and simulated carry over fraction for test O7 22

Fig. 2.17 Measured and simulated cladding temperature for test O7 22

Fig. 2.18 Measured and simulated cladding temperature for test O6 23

Fig. 2.19 Measured and simulated carry over fraction for test O8 23

Fig. 2.20 Measured and simulated cladding temperature for test O8 24

Fig. 2.21 Measured and simulated quench front elevation for test O8 24

Fig. 2.22 Schematic drawing of COSMEA test facility (2020) (not proportional to real scale) 30

Fig. 2.23 Nodalization of COSMEA facility 32

Fig. 2.24 Measured and calculated condensation rate for COSMEA experiment 33

Fig. 2.25 Measured and calculated condensate outlet temperature for COSMEA experiment 33

Fig. 2.26 Void fraction along COSMEA condensation pipe 34

Fig. 3.1 Cladding temperature downstream spacer grid No. 6 for RBHT test O-3 39

Fig. 3.2 Steam temperature downstream spacer grid No. 6 for RBHT test O-3 40

Fig. 3.3 Quench front position for No. 6 for RBHT test O-3 40

Fig. 3.4 Cladding temperature downstream spacer grid No. 6 for RBHT test O-6 41

Fig. 3.5 Discharge rates for Super Moby Dick experiment with sudden expansion 44

Fig. 3.6 Discharge rates for Super Moby Dick experiment with diffusor 44

Fig. 3.7 ATHLET Error Message 45

Fig. 4.1 Horizontal HCOs representing the core bottom plate (shaded red) with adjacent vertical TFOs for the core and lower plenum region 47

Fig. 4.2 Supported options for the coupling of horizontal plates: Left: one-sided horizontal coupling. Center: two-sided horizontal coupling. Right: two-sided horizontal coupling, at one side inside a TFO CV. 48

Fig. 4.3 Comparison of convective heat transfer enhancement factors for different spacer grid types 51

Fig. 5.1 Excerpt from the log file containing information for the user on non-default input parameter settings 54

Fig. 5.2 Sample output of the function plotTemporalEvolution() 60

Fig. 5.3 Sample output of the function plotAxialDistribution(). The abscissa axis has been aligned vertically facing downward using the setting `orientation="verticalDown"` 62

Fig. 5.4 Sample output of the function plotRadialDistribution(). The auxiliary line between the data points is not interrupted by the gap between two zones when the value “plot” is used for the parameter “plotFun” 63

Fig. 5.5 Sample output of the function plotRadialTemperature(). On the right-hand side, the arrow indicates the value of the HCV-adjacent fluid temperature. 64

Fig. 5.6 Sample output of the function plotObjects(). The TFOs containing mixture levels are labelled, the level position is indicated using a white horizontal bar..... 65

Fig. 5.7 Representation of horizontal plate HCOs in AIG-2 67

Fig. 6.1 Schematical representation of the considered bundle configurations. Top: In-line arrangement of pipes. Bottom; staggered arrangement of pipes with the narrowest cross section either perpendicular to the main flow direction (left) or in the diagonal (right)..... 69

Fig. 6.2 Contribution of each line of pipes to the form loss coefficient for a pipe bundle in in-line arrangement..... 70

Fig. 6.3 Contribution of each line of pipes to the form loss coefficient for a pipe bundle in staggered arrangement..... 71

Fig. 6.4 Erroneous nodalization of HCO HSG1 with non-matching grids in lower pipe section 72

Fig. 6.5 Correct nodalization of HCO HSG1 resulting in completely matching grids on both sides of HCO 73

Fig. 7.1 Cladding temperature at 2.69 m for RBHT test O-22 83

Fig. 7.2 Cladding temperature at 2.89 m for RBHT test O-19 84

Fig. 7.3 Cladding temperature at 2.89 m for RBHT test B-9..... 84

Fig. 7.4 Cladding temperature at 2.69 m for RBHT test O-19 85

Fig. 7.5 Peak cladding temperatures across the 17 RBHT phase II tests..... 86

Fig. 7.6 Time to reach the peak cladding temperature in the 17 RBHT phase II tests..... 86

Fig. 7.7 Quench time of the point of maximum power in the 17 RBHT phase II tests..... 87

Fig. 7.8 Core crossflow benchmark definition /BES 23/ 90

Fig. 7.9 Nodalization scheme for core crossflow benchmark 91

Fig. 7.10 Axial mass flow rate in cold and hot assembly at 7 MPa 92

Fig. 7.11 Cross flow along fuel assemblies 92

Fig. 7.12 Impact of friction loss coefficient on cross flow for 3D (left) and 6-equation (right) models 93

Fig. 7.13 Axial mass flow rate in cold (left) and hot (right) assembly at 1 MPa 93

Fig. 7.14 CA and HA wall temperature for BC2 at 1 MPa 94

Fig. 7.15 Assembly-wise nodalization adopted to BC3 and BC4 cases 96

Fig. 7.16 Liquid and vapor cross flow velocity for BC3 (2m vs. 3D) 97

Fig. 7.17 Void fraction in CA and HA for BC3 (3D) 97

Fig. 7.18 Void fraction against vapor superficial velocity for different pressures /BES 25b/ 101

Fig. 7.19 Bundle nodalization for interfacial friction model analyses, mass flow boundary condition at the bottom and pressure boundary condition at the top 102

Fig. 7.20 Void fraction against vapor superficial velocity for different pressures 103

Fig. 7.21 Phase distribution parameter by superficial vapor velocity 104

Fig. 7.22 Phase distribution parameter by void fraction at 10 bar 104

Fig. 7.23 Phase distribution parameter by void fraction at 100 bar 105

Fig. 7.24 Instrumentation for CRIEPI rod bundle test /ARA 22/ 107

Fig. 7.25 Nodalization for CRIEPI rod bundle test calculations 108

Fig. 7.26 Measured vs. calculated void fraction at 10 bar 109

Fig. 7.27 Measured vs. calculated void fraction at 30 bar 109

Fig. 7.28 Measured vs. calculated void fraction at 72 bar 110

Fig. 7.29 Geometry and dimensions of the six geometrical singular pressure loss configurations /BES 25c/ 112

List of Tables

Tab. 2.1 Comparison of measured and calculated critical heat fluxes 15

Tab. 2.2 Initial and boundary conditions of RBHT phase I open tests 18

Tab. 2.3 Initial and boundary conditions of COSMEA 2020 experiment 31

Tab. 7.1 Parameters of the RBHT Phase 2 open and blind tests 81

Tab. 7.2 Boundary conditions for cross flow benchmark 90

Tab. 7.3 Boundary conditions for tests BC3 and BC4 95

Tab. 7.4 Geometrical characteristics of the rod or tube bundles in LWR 100

Tab. 7.5 BC for tests 1 to 30 for the SIRIUS-3D experiment 106

Tab. 7.6 Errors on void fraction with ATHLET 2M model and experiment 110

Tab. 7.7 Inlet boundary conditions applied to the six geometrical singular pressure loss configurations 112

Abbreviations

1M	one momentum equation (5-equation model)
2M	two momentum equation (6-equation model)
AIG	ATHLET Input Graphics
BMUKN	Bundesministerium für Umwelt, Klimaschutz, Naturschutz und Nukleare Sicherheit (Federal Ministry for the Environment, Climate Action, Nature Conservation and Nuclear Safety)
BWR	boiling water reactor
CHF	critical heat flux
COSMOS	Critical-heat-flux On Smooth and MOdified Surfaces
CV	control volume
CW	control word
DFFB	Dispersed flow film boiling
DHVA	Druckhalterversuchsanlage
FLRM	flow regime maps
GIG	GCSM Input Graphics
HCO	heat conduction object
HECU	Heat conduction module within ATHLET
HTC	heat transfer coefficient
IKET	Institute of Nuclear and Energy Technologies
KIT	Karlsruhe Institute of Technology
KW	keyword
LOCA	Loss-of-coolant accident
LOFT	loss-of-fluid test
LSTF	large-scale test facility
MARS	Multi-dimensional Analysis of Reactor Safety
MAE	Mean absolute error
ME	Mean error
MF	momentum flux
ML	mixture level
PC	priority chain
PCT	peak cladding temperature
PK	point kinetic
PW	pseudo keyword
PWR	pressurized water reactor

RBHT	Rod Bundle Heat Transfer
RELAP	Reactor Excursion and Leak Analysis Program
RMSE	Root mean squared error
SMR	Small Modular Reactor
SPACE	Safety and Performance Analysis Code for Nuclear Power Plants
SSC	stead state calculation
SW	sub-keyword
TDV	time-dependent volume (pressure-enthalpy boundary condition)
TFD	thermo-fluid dynamic
TFO	thermo-fluid object
TRAC	Transient Reactor Analysis Code
TRACE	TRAC/RELAP Advanced Computational Engine
TSO	Technical Safety Organisation

Nomenclature

Symbols

A	flow area, m²
C	interfacial shear coefficient, N/m³
C_0	phase distribution parameter
C_l	friction factor coefficient for liquid phase, -
c	specific heat capacity, J/kg/K
D, d	diameter, m
E	entrained droplet fraction, -
e_d	entrained liquid fraction, -
f	interfacial shear factor, N/m²
G	mass flow rate, kg/s
g	gravitational acceleration, m/s^2
htc	heat transfer coefficient, W/m²/K
H	specific energy, J/kg
h	height, m
l	length, m
m	mass, kg
N_f	viscosity number, -
p	perimeter, m
$\vec{p}$	vector holding the overall path rates of the various flow regimes, -
Pr	Prandtl number, -
R, r	radius, m
Re	Reynolds number, -
S	arc length, chord length, m
t	time, s
V	volume, m^3
v	velocity, m/s
w	percentage in the path constructing $\vec{p}$, -
w	velocity, m/s
We	Weber number, -
α	void fraction, -
γ	inclination angle, °

	condensation/evaporation rate, kg/s
λ	heat conductivity, W/m/K
	Darcy-Weisbach wall friction factor, -
μ	dynamic viscosity, Pa · s
ρ	density, kg/m^3
σ	surface tension, N/m
τ	interfacial shear per unit volume, N/m³
τ_i	interfacial shear stress, N/m²

Subscripts and superscripts

0	upstream spacer grid
32	Sauter
ann	annular
b	single bubble
crit	critical
CV	control volume-specific
d	single droplet
f	film
FB	film boiling
g	gaseous
h	hydraulic
H	HCO surface-specific
i	interface
φ, k	phase index
l	liquid
loc	local
NB	nucleate boiling
max	maximum
r	relative
s	superficial
SA	value at upper end of slug to annular-mist flow regime transition
tot	total
v	vapor
w	wall

Gesellschaft für Anlagen- und Reaktorsicherheit (GRS) gGmbH

Schwertnergasse 1
50667 Köln
Telefon +49 221 2068-0
Telefax +49 221 2068-888

Boltzmannstraße 14
85748 Garching b. München
Telefon +49 89 32004-0
Telefax +49 89 32004-300

Kurfürstendamm 200
10719 Berlin
Telefon +49 30 88589-0
Telefax +49 30 88589-111

Theodor-Heuss-Straße 4
38122 Braunschweig
Telefon +49 531 8012-0
Telefax +49 531 8012-200

www.grs.de

ISBN 978-3-911727-57-0